Modelling and Placement Strategy Analysis for Integration of Offshore Floating Solar with Wind Farms

Savion D'Mello

Delft University of Technology

Modelling and Placement Strategy Analysis for Integration of Offshore Floating Solar with Wind Farms

by

Savion D'Mello

Student Number

5748704

TU Delft Supervisor:	Dr. H. Ziar
TNO Supervisor:	Dr. Y. Liu
Project Duration:	September, 2023 - July, 2024
Faculty:	Electrical Engineering, Mathematics and Computer Science, Delft

TU Delft

TNO innovation for life

PVMD Delft University of Technology

Abstract

The transition to renewable energy sources is crucial for mitigating climate change and ensuring a sustainable energy future. Harnessing the potential of offshore wind and floating solar technologies offers a promising avenue to increase the share of renewables in the global energy mix, reducing reliance on fossil fuels and minimising environmental impact. Offshore floating PV technology in itself and its integration with existing offshore wind farms is a new application, requiring research and development to prove its viability. Within this research field, more comprehensive models are being developed to accurately estimate the power and energy output of floating PV installations, incorporating unique characteristics and conditions specific to these systems. Simulation models for land based PV systems cannot be used as they cause an error due the different environmental conditions. The objective of this thesis is to develop such a model and use it to determine the physical placement of these floating installations in the wind farm to maximise the energy generated.

EE-Farm II is a sophisticated simulation tool designed for evaluating the electrical systems of wind farms, encompassing both AC and DC components which has now been enhanced to integrate solar farm modelling. The model for floating PV was built on the existing EE-Farm II tool in MATLAB. A tilt model from literature is used to analytically determine the effect of sea waves on the tilt of the floating PV and a model to find the effect of static shading of the wind turbine on the floating installation was developed from scratch.

In the model, the effect of degradation has been neglected and it has been assumed that the MPPT of the inverters is ideal. The tilt model shows that on average the annual energy produced would be similar to the case with no tilt effects considered i.e. fixed tilt however, the power variability can be observed on a smaller temporal scale (for e.g. daily) and is dependent mainly on the wind speeds. The energy loss on a floater due to shading in the worst-case scenario for the simulation considered was found to be 10.5% and due to the wind farm being in the North Sea, shading losses are prevalent in the north of the wind turbine.

This work helped understand the behaviour and make better power variability and energy estimations for offshore floating PV installations and also helped understand how to better place floating PV when integrating it with an offshore wind farm to maximise energy production. This work can help installation companies with their analysis and to make predictions about the energy output and possible variability throughout the year in different temporal scales. Future work should focus on determining the optimal orientation of the panels or strings by improving the model by modelling bypass diodes in the modules, addressing the current limitations due to the simplifications made.

Acknowledgement

I did this master's graduation project with the support of the Photovoltaic Material and Devices (PVMD) research group at the Technical University of Delft and the Wind Energy Group at TNO, Delft. Recognising the contributions of my peers both at the university and at TNO, I thank them for their valuable insights and encouragement during the course of this project. Appreciation goes to my TNO supervisor, Dr. Yichao Liu, for his constant support, supervision, and motivation, especially during challenging times.

With immense gratitude, I acknowledge my TU Delft supervisor, Dr. Hesan Ziar, for his meticulous advice that has shaped me into a better researcher and enabled me to produce work that I am proud of. A special thanks to Dr. Edwin Wiggelinkhuizen from TNO for his technical assistance and interesting technical discussions from the very beginning. TNO's provision of access to the remote cluster, which allowed me to run my code faster and obtain my results efficiently, was invaluable and I would like to thank them for their support. I would also like to thank to Dr. Arthur Weeber and Dr. Antonio Jarquin Laguna for being part of the thesis committee and offering their guidance during the final stage of my thesis.

These last two years at TU Delft have been a dream, and it would not have been possible without the support of my family and my housemates. I will cherish my time spent here during my master's and am deeply thankful for their unwavering support and love.

Savion D'Mello
Delft, July 2024

Contents

Abbreviations

Abbreviations

Abbreviation	Definition
AC	Alternating Current
DC	Direct Current
DHI	Diffuse Horizontal Irradiance
DNI	Direct Normal Irradiance
GHI	Global Horizontal Irradiance
(H)RES	(Hybrid) Renewable Energy Systems
HV	High Voltage
LV	Low Voltage
MPPT	Maximum Power Point Tracker
MV	Medium Voltage
(O)FPV	(Offshore) Floating Photovoltaic
OFW	Offshore Wind Farm
POA	Plane of Array
PV	Photovoltaic
RES	Renewable Energy Sources

1 Introduction

1.1. Background

The world is witnessing a significant rise in energy demand driven by population growth, urbanisation, and economic development [1]. This surge in energy consumption is putting immense pressure on traditional energy resources, highlighting the necessity for a transition towards sustainable energy solutions. Renewable energy sources are becoming increasingly vital to address these challenges, ensuring a reliable and sustainable energy supply for the future [2]. Amidst growing global commitment to sustainable energy, renewable energy sources are increasingly crucial in meeting climate goal targets and enhancing energy security. In particular, the Dutch government's ambitious renewable energy goals underscore a pressing need to innovate and expand energy generation capabilities within constrained geographic and economic contexts [3].

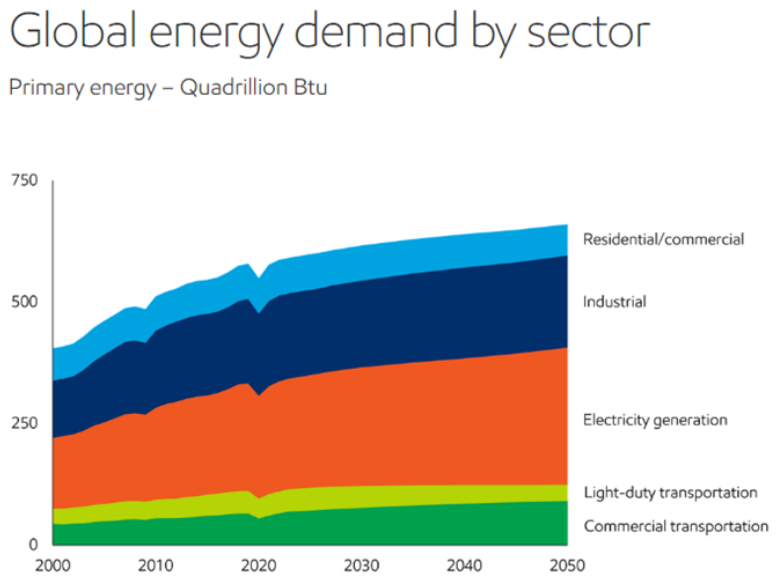

Figure 1.1: Increase of Global Energy Demand. Figure From [4]

Offshore renewable energy technologies, particularly wind and solar, represent a strategic response to the dual challenges of land scarcity and the need for sustainable energy production. The North Sea emerges as a pivotal region for renewable energy development [5] due to it's renewable potential. While offshore wind technology has already seen extensive development [6], offshore floating photovoltaic systems are still in their infancy and initial research and development stages.

Offshore wind technology harnesses the power of wind over open water, where wind speeds are typically higher and more consistent than on land. This technology involves the use of wind turbines installed in bodies of water, usually on the continental shelf. Offshore wind farms have the potential to generate large amounts of renewable energy, contributing significantly to the reduction of carbon emissions and the transition to sustainable energy sources. The turbines are often anchored to the seabed, and advancements in floating turbine technology are expanding the potential for offshore wind farms in deeper waters. Offshore wind technology plays a crucial role in meeting global energy needs while mitigating the impacts of climate change [7].

The concept of Hybrid Renewable Energy Systems (HRES), one such combination is the combination of offshore wind and floating PV installations which has the potential to offer enhanced energy reliability and efficiency [8]. This integration capitalises on the complementary nature of wind and solar energy—whereby periods of high solar irradiance typically coincide with lower wind speeds, and vice versa—ensuring a more stable and consistent energy output [9].

Furthermore, integrating these technologies can lead to significant infrastructural efficiencies. Utilising existing offshore wind farm cables for floating solar installations has the potential to reduce the costs associated with undersea cabling also maintenance costs can be shared for such integrated systems. Therefore this provides a cost-effective solution to energy generation in offshore settings [10, 11].

1.2. Floating Photovoltaics

FPVs represent a burgeoning frontier in renewable energy technologies, combining water-based installations with solar energy capture. First commercialised in 2007 on a reservoir in California, FPVs have expanded rapidly, now exceeding a global installed capacity of over 3 GW by 2020 [12].

FPVs are designed to float on water surfaces, utilising buoyant structures that support photovoltaic panels. These systems leverage the cooling effects of water to enhance panel efficiency and mitigate the thermal losses typically associated with terrestrial solar arrays [13]. The main components of an FPV installation are shown in figure 1.2.

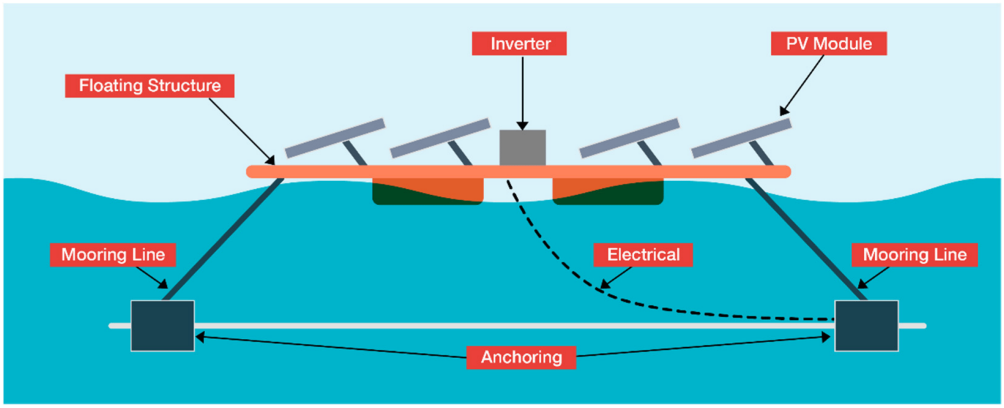

Figure 1.2: Main Components of an FPV Installation. Figure From [14]

The primary advantage of FPVs lies in their minimal land use, making them particularly valuable in land-scarce regions such as the Netherlands. Additionally, they help reduce water evaporation from bodies they cover, contributing to water conservation efforts while generating electricity [15]. The cooling effect provided by the water body underneath also increases the efficiency of the solar panels, offering a performance advantage over land-based systems [16].

Despite their benefits, FPVs face several challenges, especially in offshore installations. The harsh marine environment introduces complexities such as corrosion, and mechanical stresses from waves

and wind. Moreover, the lack of established standards for such installations poses significant hurdles for widespread adoption [17]. Globally, FPVs have been implemented in various settings, ranging from small ponds and reservoirs to large lakes and coastal areas. However, the offshore application remains limited, with pilot projects just beginning to explore the potential of open sea environments [18].

Ongoing research and development are focused on enhancing the durability and efficiency of FPVs to make them viable for broader offshore use. Innovations in materials and system designs that can withstand marine conditions are critical to the future expansion of FPVs in the renewable energy sector [19, 20].

In summary, FPVs offer a promising avenue for expanding renewable energy capacities, especially in regions with limited land availability. While the technology presents unique challenges, particularly in offshore settings, the potential benefits in terms of energy yield and environmental impact make it a compelling area for continued research and development.

1.3. Offshore Wind Technology

Offshore wind technology has its roots in the early 1990s when the first offshore wind farm was constructed in Denmark [21]. This marked the beginning of a new era in renewable energy, taking advantage of the stronger and more consistent wind resources available offshore compared to onshore sites. Over the past three decades, technological advancements and increasing investments have led to the development of larger, more efficient turbines and expansive wind farms, transforming offshore wind into a significant contributor to the global energy mix [22].

Offshore wind energy plays a crucial role in the transition to a sustainable energy future. It offers the potential to generate vast amounts of clean electricity, reduce greenhouse gas emissions, and decrease reliance on fossil fuels. This is particularly important for coastal cities and regions where space for onshore wind farms is limited, and energy demands are high [23]. Offshore wind farms consist of large wind turbines installed in bodies of water, typically on the continental shelf. These turbines are anchored to the seabed using various foundation types, such as monopiles, jackets, or floating platforms, depending on water depth and seabed conditions. The generated electricity is transmitted to the mainland via undersea cables [24]. A few types of offshore wind turbine installation are shown in 1.3.

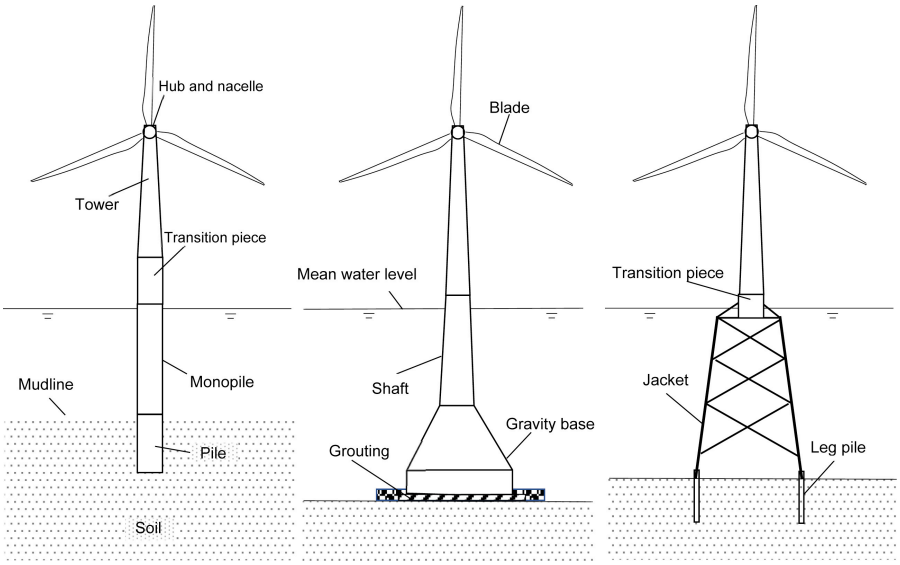

Figure 1.3: Schematic of Monopile, Gravity-Based and Jacket Offshore Wind Turbines. Figure From [24]

Economically, offshore wind creates jobs and stimulates investment in coastal regions. Environmentally, it contributes to the reduction of carbon emissions and air pollution [25]. However, the installation

and operation of offshore wind farms can pose challenges, such as impacts on marine ecosystems and navigation routes. Balancing these factors is critical for the sustainable development of offshore wind energy [26]. The future of offshore wind looks promising, with trends pointing towards the development of larger turbines, floating wind farms, and integration with other renewable energy sources [27]. However, challenges remain, including high initial costs, complex logistics, and regulatory hurdles. Continued research and innovation are essential to overcome these obstacles and fully realise the potential of offshore wind energy [28].

1.4. Benefits of Integrating Renewable Energy Sources in a Single Power Plant

The benefits of hybrid wind and solar farms are multifaceted and significant, particularly in the context of offshore and onshore installations. In [8] the integration of these renewable energy sources plays a crucial role in enhancing the stability and efficiency of energy supply. In Western Iberia, [8] revealed that while offshore wind energy resource is higher than solar PV on an annual scale, the combination of these two renewable resources leads to a significant reduction in the seasonal variation of energy throughout the year. Figure 1.4 illustrates what an offshore hybrid solar and wind farm would look like.

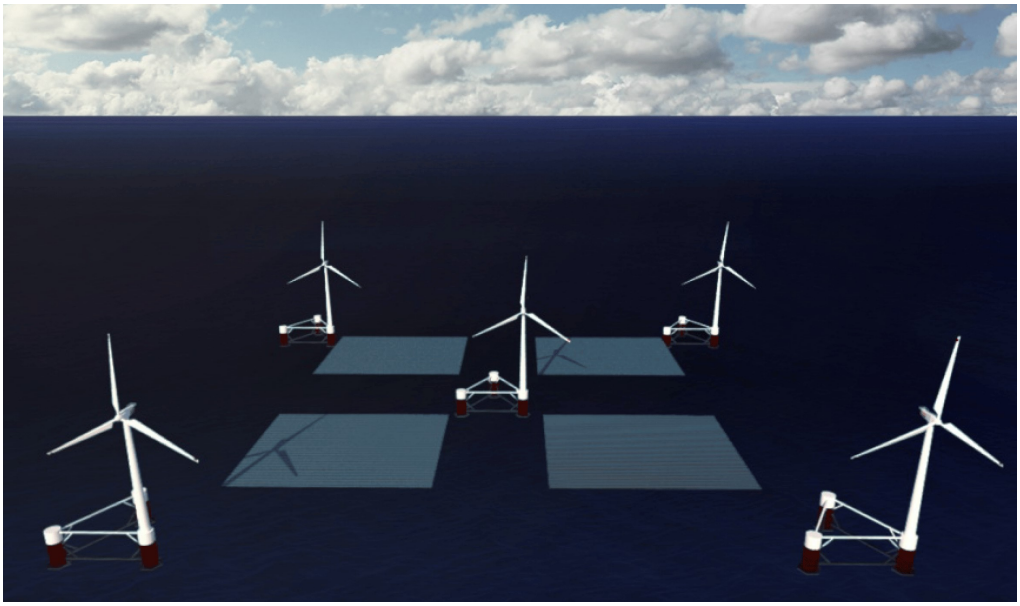

Figure 1.4: Illustration an Offshore Wind Solar Farm. Figure From [29]

The integration of RES like wind and solar is pivotal for achieving ambitious decarbonisation targets set by regions such as the European Union [30]. The diversification of energy sources through marine renewables, including offshore wind and solar PV, contributes significantly to the overall reduction of greenhouse gases emissions. In this context, the study highlights the potential of offshore renewables to support a substantial portion of the European Union's electricity consumption by 2050 [31].

The distribution of offshore wind farms is not homogeneous across Europe, with northern Europe, particularly the United Kingdom, Germany, and Denmark, leading in offshore wind installations. However, regions like the western Iberian Peninsula show high offshore wind energy resource potential, comparable to that in the North Sea [8]. The technological evolution of floating offshore wind turbines is anticipated to foster new offshore wind farms in these areas. The integration of offshore wind and solar PV is increasingly considered due to the high level of technological maturity of both renewable sources.

The integration of offshore wind and solar PV has been shown to present technical and economic benefits. For instance, such integration can result in a higher use rate of the infrastructure, such as the

cables transporting electricity to the coast [11]. Additionally, offshore solar PV panels installed at the sea waterline operate with higher efficiency due to lower temperatures, which can be about 13% more efficient on average than land-based systems [32].

While the current research provides valuable insights, it also lays the groundwork for future research. This includes analysing the legal constraints for offshore platform installations and studying the balance between energy supply and demand at a finer temporal resolution. Future research should also consider technological advancements in offshore marine energy and their implications for the planning and development of renewable energy production systems.

1.5. Challenges and Disadvantages OFPVs

Combining offshore wind and solar energy presents several challenges, which are necessary to understand for the successful implementation and operation of such hybrid systems. These challenges stem from various technical, environmental, and socio-economic factors associated with both OFPV and wind energy systems.

OFPV systems require floaters for buoyancy, commonly made from materials like high-density polyethylene (HDPE). The choice of material and design of these floaters is critical for the stability and durability of the OFPV systems, particularly in harsh marine environments [33]. For FPV, a robust mooring system is essential to secure the floating structure, especially in areas with strong winds and high waves. This adds complexity to the design and increases the need for a substantial number of mooring points to maintain system integrity. Saltwater environments can accelerate the degradation of PV systems, including micro-cracks in solar cells due to constant movement and corrosion from saltwater [34]. This necessitates frequent maintenance and increases long-term operational costs. Accurately modelling the performance of FPV systems is complex due to factors like tilt angle variations caused by waves, and the cooling effects of water. These factors make standard modelling approaches less effective.

Coverage of water surfaces by FPV systems is limited to reduce environmental impacts and accommodate other water-based activities. This limitation restricts the potential scale of FPV installations. Seasonal weather variations significantly impact FPV systems, especially in regions with monsoon seasons where reservoir water levels fluctuate, affecting the suitability for FPV installations [35].

The specialised equipment required for hybrid floating solar installations often results in higher initial costs compared to traditional land-based installations. However, these costs are expected to decrease as the technology develops. There is a current knowledge gap in the industry regarding hybrid FPV systems. Limited experience with these systems can hinder data-driven decision-making and optimisation of operations. The development of hydropower and associated hybrid systems must be carefully evaluated for their social and environmental impacts. This includes considerations for the local communities, aquatic ecosystems, and overall sustainability.

1.6. Need for Research

The research gaps in the field of offshore floating photovoltaic systems are multifaceted, involving technical, environmental, and economic aspects. A major challenge for integrating solar PV and wind energy sources for electricity generation is the intermittent nature of these resources [36]. Integrating solar and wind resources into an optimum combination can partially resolve this issue and make the system more reliable and economical, particularly for stand-alone generation [11]. Voltage and frequency fluctuation and harmonics are significant power quality issues for both grid-connected and stand-alone systems [37]. Addressing these requires proper design, advanced control facilities, and good optimisation of hybrid systems.

Deployment of OFPV is limited due to unique marine and sea environments, such as wind loads and wave loads, which differ from onshore conditions. Offshore FPV systems have shown to be more economically and technically efficient when using thin-film PV at different latitudes [38].

Studies have shown that offshore FPV systems are more efficient due to natural cooling effects and differences in radiation intensity depending on the altitude of the sun and that the total electricity energy annually for offshore is higher than for inland FPV systems [32]. Research has been conducted to evaluate the effects of OFPV systems on the ecosystem, including hydrodynamics and fishery exploitation in coastal areas. Primary production depends strongly on the coverage density by floating platforms due to light deficit at different locations [39].

The influence of wind turbine shading on floating photovoltaic (FPV) systems requires thorough investigation. Static shading has been simplified in [40] however, this model cannot be extended to understand the dynamic nature of shading due to the blades of the wind turbine. Land-based simulations applied to FPV systems have shown high error margins on the energy calculations when compared to actual onshore FPV measurements, indicating the need for more accurate offshore-specific models [41, 42].

Economic feasibility is another critical area for upscaling and industrialising renewable energy systems. Understanding the cost dynamics and economic viability is essential to justify investments and support policy-making for offshore FPV systems [43]. Furthermore, the degradation characteristics of PV panels in offshore conditions remain largely unknown. Offshore environments are harsher, with saltwater exposure and higher humidity levels, which can accelerate panel degradation and affect performance over time [34].

The impact of combined RES on the stability of the collection system and grid compliance also warrants comprehensive research. Integrating large-scale offshore wind and FPV systems can pose challenges due to the intermittent nature of both energy sources, potentially affecting grid stability and compliance with regulatory standards. Additionally, innovative maintenance solutions need to be explored to reduce costs and enhance safety for offshore installations, where accessibility and environmental conditions pose significant challenges [44].

The environmental impact of large offshore FPV installations is not well understood. Research is needed to assess the potential effects on marine ecosystems, biodiversity, and water quality [45]. Moreover, the resilience of offshore FPV systems to extreme weather events, such as hurricanes and typhoons, needs to be evaluated to ensure their reliability and durability under such conditions. Advancements in new materials and designs are crucial for improving the performance and longevity of FPV systems. Research into different mechanical configurations of floating PV systems can lead to innovations that optimise energy capture, reduce costs, and enhance system stability.

The focus of this thesis underscores the pressing need for more detailed research into the influence of wind turbine shading on FPV systems and the discrepancies observed when applying land-based simulations to offshore environments. This need is particularly urgent due to ongoing projects researching integration of offshore floating solar with existing wind farms, which would greatly benefit from a model capable of accurately estimating characteristics such as power variability and energy output of these systems. These areas are critical to understanding and improving the performance of FPV systems, and they form the primary focus of the investigations carried out in this thesis.

1.7. Research Objectives and Thesis Outline

In this section, the research objectives and the thesis outline is discussed. The primary research objective is to develop a strategy for placement of Offshore Floating Photovoltaic installations within an offshore wind farm to maximise DC energy output. To achieve this main objective, two sub-objectives have been outlined:

1. **Modelling OFPV:** The first sub-objective focuses on developing a model for OFPV energy production for such systems integrated in an OWF. This model incorporates factors such as the tilt dynamics of the OFPV system and the shading effects caused by the wind turbines on the OFPV. The tilt dynamics refer to how the floating platform's inclination, influenced by sea waves, affects

the solar panels' orientation and, consequently, their energy output. By modelling these dynamics, we can understand the power fluctuations. Additionally, the shading effects from wind turbine blades, towers, and nacelles can significantly reduce the energy yield of PV panels especially the ones closer to the wind turbine. Hence, this model must also simulate these shading impacts to provide a realistic estimate of the energy production and identify areas and parameters that mostly affect shading losses.

2. **OFPV Placement Strategy:** The second sub-objective is to strategies how to go about selecting where to place these OFPV systems in the wind farm. This involves analysing the energy grid maps which show how much energy would be outputted by an OFPV platform in a wind farm and this would be found from simulations. To understand how the analysis for the placement of the OFPV platform would happen, various constraints such as mooring lines, electric cables, and shipping lanes are considered for analysis. The strategy would place the OFPV systems in unconstrained areas that minimise shading, thereby enhancing the overall energy yield. By integrating these systems, the combined output of the wind and solar installations can be maximised, making the renewable energy farm more efficient and cost-effective.

Through these detailed research objectives and questions, the study aims to provide a robust framework for integrating OFPV systems within offshore wind farms, leveraging modelling techniques and understanding strategies for placement of OFPV to achieve maximum energy production.

This thesis is structured into five chapters. Chapter 2 outlines the layout and specifications of an offshore wind farm and integrated OFPV system, used as a case study, covering the wind farm location, module and floater specifications, and electrical infrastructure such as inverters, transformers, and cables. Next, chapter 3 which is the methodology chapter details the modelling workflow and simulation components, including initial setup, input data, wind and PV system integration, in-plane irradiance calculation, and the tilt and shading models. It also addresses DC power calculations and various optimisations, such as node spacing sensitivity analysis and the use of lookup tables. Chapter 4 presents the simulation results, analysing the tilt model, irradiance and frequency node maps which illustrates how the irradiance and frequency of the number of times a node is shaded varies for nodes - which have been used for spatial representation of OFPV - in the area surrounded by a wind turbine. Followed by floater energy and irradiance grid maps where the energy and the irradiance of reference floaters surrounding a wind turbine is illustrated. It examines daily power production profile, energy loss analysis, and cluster placement strategies to optimise OFPV systems within wind farms. The final chapter discusses the implications of the findings, challenges, and limitations, suggesting future research directions and practical applications. It emphasises the need for advanced MPPT modelling and improved shading models, highlighting the research's significance in predicting energy output and understanding power variability in hybrid offshore wind-solar farms.

2

Case Study Description

This section details the physical and electrical configuration of the hybrid renewable energy farm. Initially, the location and layout of the wind farm are discussed. Subsequently, the physical arrangement of what is termed as the reference cluster and floater, including the layout of the PV string, is described. Following this, the specifications of the modules used in the simulation are provided, along with information about the considered inverter skid. The section concludes with a brief overview of the cables and transformers considered in the modelling environment.

2.1. Wind Farm Location and Layout

The Hollandse Kust Noord (HKN) wind farm [46] is considered as the site for the hybrid wind farm simulations. This is because of the fact that an offshore floating solar system is planned to be integrated in this wind farm. The wind farm is located in the HKN wind farm zone in Dutch Exclusive Economic Zone (EEZ) of the North Sea. The actual wind farm consists of 69 wind turbines of capacity 11 MW each. figure 2.1 shows the wind farm zone where the wind farm is located in the North Sea. This zone is about 25 kms from the shore where the water depth is about 20-28 m.

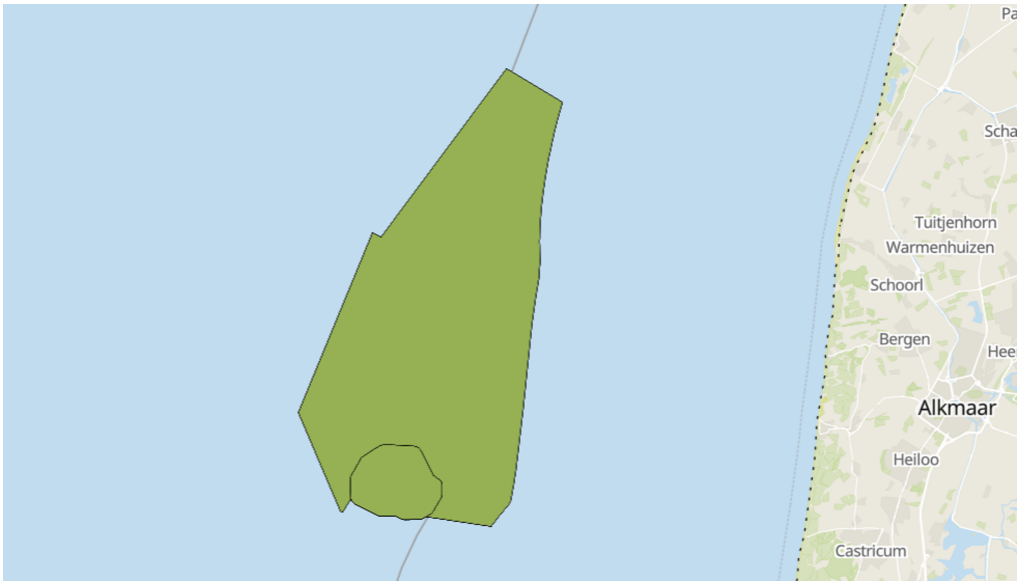

Figure 2.1: HKN Wind Farm Zone in Dutch EEZ of the North Sea. Figure Derived From [47]

The wind farm layout considered in the EE-Farm II tool is shown in figure 2.2. This reference wind farm is considered for the simulations done in this thesis project. This is a hypothetical layout which

consists of 8 strings of wind turbines with a total of 63 wind turbines of 12 MW capacity each and their coordinates were selected trying to minimise wake losses. This analysis was done previously and is out of scope for this thesis, for the purposes of this project, only the layout is of use. These 8 strings are connected to the offshore substation with 3 phase sub-sea inter-array cables at a standardised AC high voltage level of 66/69 kVac.

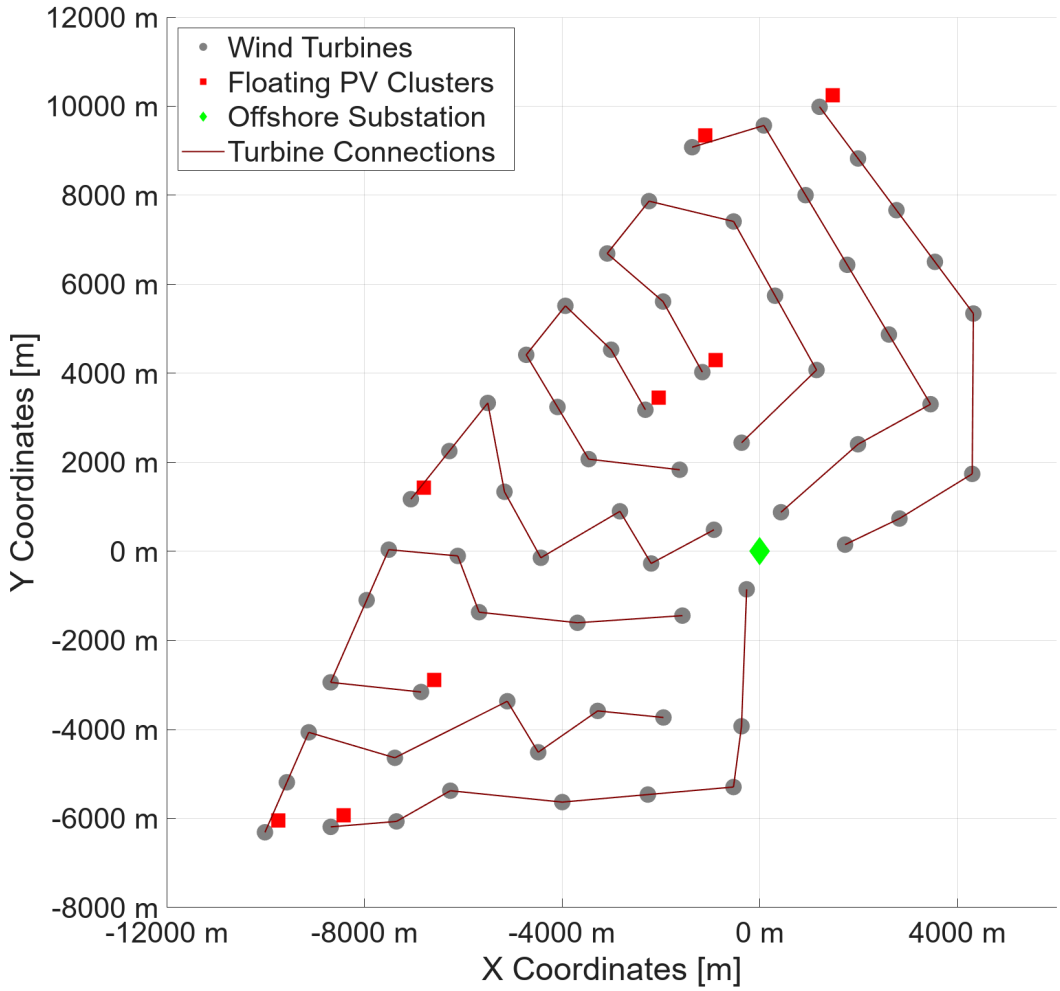

Figure 2.2: Wind Farm Layout Considered in the Simulation

2.2. Module, Reference Floater and Cluster Specification

The PV module was taken to be the same one used in previous simulations done to study challenges of integrating OFPV with an OFWF. This module is a mono-crystalline silicon panel manufactured by Canadian Solar [48]. The PV module has a rated power of 660 Wp and a module efficiency of 21.2%.

The reference floater considered in the simulations is made up of floating bodies considered in [43]. The pontoon structure is made up of high-density polyethylene (HDPE) cubes. Each cube measures 50 cm × 50 cm × 40 cm and weighs 6.5 kg, with a flotation capacity of 87.5 kg per cube. The pontoon is designed to be anchored to the sea floor, allowing for rotation but preventing displacement. This design ensures the structure remains stable while floating on the sea surface, minimising mechanical fluctuations caused by wave movement.

In [43] the dimensions of the pontoon are optimised to reduce angle variations due to wave effects. It was determined that a heavy, short, and wide pontoon aligned with the predominant wind direction minimises these fluctuations. For the simulation cite located in the North Sea, a square-shaped pontoon was chosen. The length and the width of the reference floater in the simulation is 40 m. The pontoon supports the PV modules, arranged in series with string. On a reference floater in the simulations, there are 12 strings arranged in the East-West direction in a straight line with 26 PV modules connected in series in each string as seen in figure 2.3. The capacity of this reference floater is 206 kW.

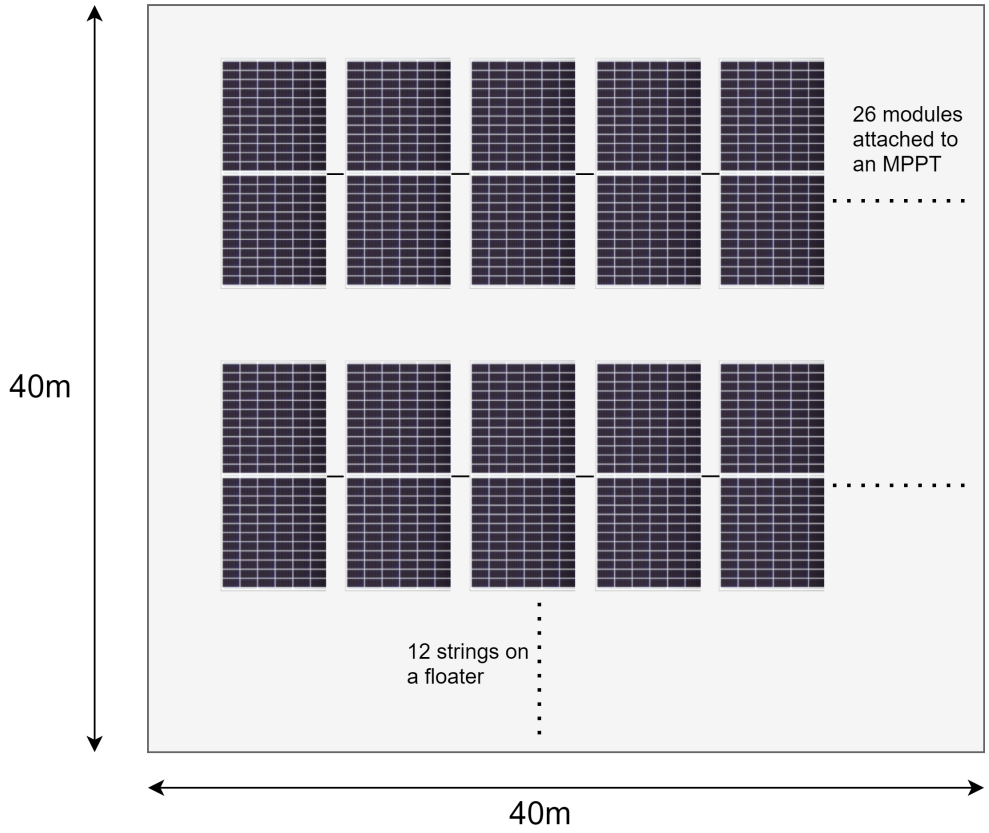

Figure 2.3: Illustration of Reference Floater

In the particular hybrid configuration seen in figure 2.2, 8 floating PV clusters can be observed with each cluster connected to a separate wind turbine string. The capacity of these clusters is nearly 15 MW. In the considered electrical topology, each cluster contains 2 inverter skids described in section 2.3 and 72 reference floaters. There is no set rule to arrange the floaters in a cluster; however, if the locations of the inverter skids are known, the floaters should be arranged to form a shape as close to a square as possible to minimise DC losses for the cables connected to the inverter skid. This is because, in a linear arrangement, the distance of each floater from the inverter skid increases, leading to higher losses. Optimal efficiency is achieved when the floaters are arranged in a square configuration, as this minimises the average distance to the inverter skid. It is to be noted that the inverter skids in a cluster are considered to be placed as close to the wind turbine as possible with the reasoning of minimising AC losses of the cables and the cable cost along with it's installation and procurement cost as well. The illustration of a cluster can be seen in figure 2.4.

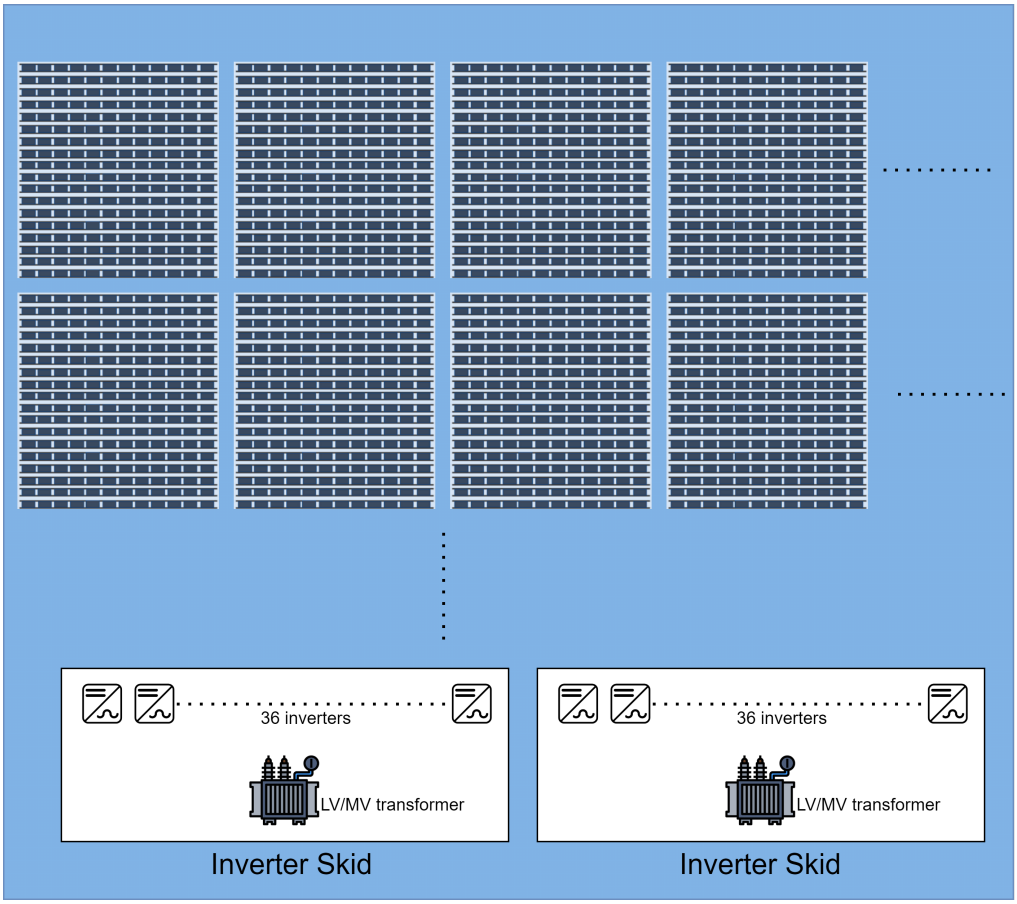

Figure 2.4: Illustration of Reference Cluster

2.3. Inverter Skid, Transformers and Cables

The inverter skid considered is also the same one as used in previous simulations in EE-Farm II and it is based on the medium voltage compact skid PVS-175-MVCS of Fimer [49] as seen in figure 2.5. It has 36 inverters of 175 kWac/185 kVA each however for the simulations done for this thesis the capacity of a reference floater is 205 kW. However since the modelling in this thesis has only been done up until the DC input of the inverter this does not affect the simulations run however in the case that the inverter model is also being run, there would be curtailment in the summer months when there is excess generation. For the purposes of the simulation, if this curtailment has to be omitted, the inverter specifications could be changed with the selection of a different inverter or the number of modules in a string can be reduced such that the capacity of the reference floater is less than that of an inverter.

Each inverter includes 12 MPPTs each of which is connected to a PV string of a reference floater which has a total of 12 strings. The selection of the number of strings in a reference floater and the number of floaters in a reference cluster has been done keeping this fact in mind. The inverter skid also includes a medium voltage transformer and a low voltage and medium voltage switchgear. The skids, are assumed to be located with the floaters in the reference cluster and thus would require a floating platform for itself too.

Stepping up voltage directly from around 1 kV to 66 kV typically requires multiple transformation steps due to practical and technical limitations associated with transformer design and efficiency. High-ratio transformers, which would directly convert such low voltages to very high voltages, face challenges related to insulation, core saturation, and efficiency losses. Insulation requirements become more stringent as the voltage difference increases, leading to increased complexity and cost. Additionally, the efficiency of a single high-ratio transformer may be lower due to higher core and copper losses

Figure 2.5: Inverter Skid Considered in the Simulation. Figure derived from [49]

[50]. By using two transformation steps, the intermediate voltage level reduces the stress on insulation and maintains higher efficiency, as each transformer operates within an optimal voltage range. This staged approach also allows for better management of thermal dissipation and improves overall system reliability and maintainability. Therefore the voltage from the output side of the inverter is stepped up in two stages to 66 kV which is the capacity of the inter-array cables. The MV-HV transformer could hypothetically be placed on a monopile near the reference cluster or it could be installed at the wind turbine. These considerations are out of scope for the research objectives of this study.

For the cabling, low voltage DC cables connect the PV strings on the floater to the inverters. Medium voltage AC cables connect the outputs from the LV-MV transformer in the inverter skid to the MV-HV transformer and finally, high voltage 66 kV AC cables are used to connect these OFPV clusters to the OFWF array. The capacity of the cables and their specifications are included in EE-Farm II however since DC cable losses are not calculated in the model these specifications are not relevant to the modelling purposes of this thesis.

3

Methodology

This chapter describes the methodology and modelling workflow used throughout this thesis. It starts by outlining the simulation model and the environment, explaining the complete modelling process from beginning to end for the objectives of this study. The chapter then details the tilt model, shading model, and the method for calculating DC power from the PV panel strings mounted on floaters. Finally, it addresses various additional tasks aimed at justifying the methodologies applied, optimising the model's performance, and maintaining accuracy, as well as discussing other relevant work done.

3.1. Modelling Workflow

In this section, the overview of the EE-Farm II tool is provided. Following that, the initialisation of the relevant paths and the importing of data is described. Next, the input data used for the simulations is described. Next, the integration of the wind and PV systems within EE-Farm II is described. Then the procedure followed to calculate the in-plane irradiance is described in detail. Finally, the tilt model, shading model and the power calculation are described in brief as they're described in detail in the following sections of this chapter. Figure 3.1 illustrates the simulation workflow for the purpose of this thesis.

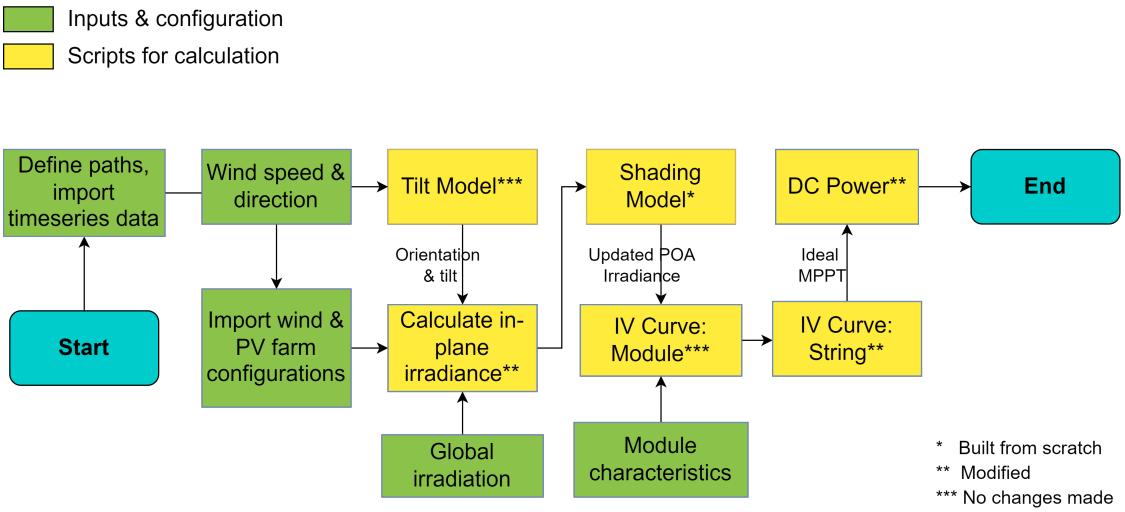

Figure 3.1: Illustration of the Modelling Workflow

3.1.1. EE-Farm II

EE-Farm II is a comprehensive simulation tool developed for the evaluation and optimisation of electrical systems in wind farms [51]. Built as a Simulink library within the MATLAB/Simulink environment, EE-Farm II facilitates the modelling of both AC and DC components of wind farm electrical systems. This tool is particularly adept at performing steady-state calculations necessary for determining electrical losses, power production, and the overall efficiency of various wind farm configurations.

The tool includes a diverse library of component models, such as wind turbines, generators, transformers, AC and DC cables, inductors, and converters. Each component is represented by a Simulink block, which can be easily connected to simulate the electrical network of a wind farm. One of the key features of EE-Farm II is its ability to handle both AC and DC electrical components.

The core simulation involves calculating the voltage, current, power, reactive power, and losses for each component under different wind speed conditions. The tool then aggregates these results to determine annual energy production and losses, providing insights into the levelled production costs of the wind farm.

In the past few years, the EE-Farm II model has been enhanced to include the capability of calculating and determining all the aforementioned quantities when integrating a solar farm with the wind farm. However, this integration was implemented using a model for the solar farm that did not account for the variation in tilt angle due to the sea waves of the floater for the solar panels and it also did not account for the shade on these solar panels due to a wind turbine in its proximity. Addressing this limitation and achieving a more accurate representation of floating offshore floating solar installations within EE-Farm II was a key objective of this project. This advancement aims to provide a better evaluation of combined wind and solar energy systems, ensuring that simulations reflect the realistic conditions and challenges of offshore environments.

3.1.2. Initialisation

The initial step in the setup of the simulation model in the main file of EE-Farm II involves defining and organising the directory paths that are crucial for the model's operation. This setup ensures that all necessary scripts, models, libraries, and result directories are correctly linked and easily accessible during the simulation runs. Paths are set relative to the project's root directory to maintain portability and adaptability of the code. The directory structure includes separate paths for the model's core components such as Simulink models, templates for auto-generation, parameter libraries, and post-processing tools.

Following the directory setup, the main specifications for the wind farm are extracted from an Excel file, which acts as a central repository for input data. This file contains multiple worksheets, each representing a different simulation scenario characterised by specific combinations of wind farm layout and OFPV configuration. The scenario-specific data are crucial as they define the operational parameters and layout that directly influence the simulation's performance and outcomes. For the simulation purposes for this thesis, the hybrid wind-solar configuration selected is as illustrated in the figure 2.2.

This organised approach in setting up paths and reading initial configurations from standardised files ensures a streamlined process, reducing the potential for errors and increasing the efficiency of the simulation runs. The separation of model components into distinct directories also aids in maintaining a clean and manageable codebase, facilitating future modifications and scalability of the simulation framework.

For the selected scenario, the necessary configuration data and results from the FarmFlow model - which simulates wind farm wake losses - are imported. Initially, the model assigns a generic project name and constructs database prefixes to access and manage component data efficiently. The model then checks for the existence of directories where results will be stored. If these directories do not exist, they are created dynamically. This ensures that all simulation outputs are organised and stored systematically. The model also searches for existing Simulink models corresponding to the scenario,

which might be split over several models due to the complexity of the configuration.

Importing data involves several key steps:

- Wind Farm and Solar Farm Configuration Data: The model retrieves configuration details from predefined Excel sheets. These details dictate the layout and operational parameters of the farms.
- FarmFlow Results: The model processes wake loss data from the FarmFlow simulations, which calculate the energy production losses due to interactions between wind turbines.
- Time Series Data: Depending on the user settings, wind and solar resource data are either applied as a wind rose frequency used by the FarmFlow model or as a time series for all time steps. This flexibility allows for detailed temporal analysis of resource availability and system performance.

The model performs calculations to adjust wind data to hub height if required, employing either Weibull scale parameters or a shear parameter approach [52]. This scaling is crucial for accurate representation of wind speeds at different elevations, directly affecting the simulation of wind turbine performance and for the solar module temperature model. Finally, the model generates time series for wind turbine power output by mapping wind time series data with the FarmFlow output tables. This step is critical as it translates wind speed and direction data into actual power generation figures, taking into account the specific characteristics of each turbine and the overall farm layout. This comprehensive setup allows for detailed scenario-based analysis, facilitating a deep understanding of the interactions between components within the wind and solar farms and their collective impact on energy production.

3.1.3. Input Data

For the accurate simulation of environmental conditions affecting the performance of the offshore PV system, meteorological data from KNMI station number 330, ”Hoek van Holland,” at 51.990998°N, 4.121798°E was utilised. This station is strategically located near the Dutch West coast, making it ideal for capturing maritime climate data relevant to the project site. The station provides comprehensive measurements of wind and global horizontal irradiance(GHI) at a high temporal resolution of 10 minutes, spanning the entire year of 2022 [53, 54]. This resolution is crucial for capturing the variability in weather patterns and their impact on solar irradiance and wind conditions. However, it is important to note that KNMI stations located directly at sea do not measure irradiance data; hence, the ”Hoek van Holland” station offers a proximal alternative that still accurately reflects the maritime climate influences expected at sea-based PV installations.

For the purposes of this study, wind speed measurements, originally recorded at 10m above ground level, are scaled to match the hub height of the wind turbines at 140 meters. This scaling is based on a wind shear exponent of 0.08 [55], which is used to adjust the wind speed data to reflect the conditions at greater heights more typical of wind turbine operations and also to adjust the wind speeds for lower height for the solar module temperature estimation at a height of 2m. Additionally, it is noted that the dataset includes some missing data points; these are systematically identified and excluded from the input dataset to ensure the accuracy and reliability of the simulation results.

3.1.4. Integration of Wind and PV System Configuration

In the simulation workflow, a critical step involves reading the layout and configuration details for both wind farms and PV systems from an Excel file, which includes data such as wind turbine and PV coordinates, cable routing, and cable types. This configuration information, extracted from specified ranges within the Excel file, forms the structural backbone of the simulation, dictating how individual components such as turbines and PV modules are interconnected and how energy flows within the system.

Once the configuration data are loaded, the simulation proceeds to implement the tilt model. This model dynamically calculates the tilt and azimuth angle for the floating PV arrays using the tilt model. Specifically, the tilt model adjusts the angle of the PV modules based on the effect of the sea waves which changes their solar irradiance. This model takes into account factors like wind speed and direction,

which can influence the floating platform's orientation. This step is crucial for estimating realistic operational scenarios as it directly affects the in-plane irradiance, which in turn impacts the power output of the PV modules. A more comprehensive discussion and technical details of the tilt model are provided in section 3.2, where the methodologies used are discussed in depth.

An essential aspect of the simulation's setup involves the creation and utilisation of structured data storage systems, specifically through the use of structures in MATLAB. These structures are pivotal for organising and managing a vast array of configuration data efficiently. For instance, data related to wind turbines, such as coordinates, relative distances, and specific components like transformers and cables, are stored within a structured format. This approach allows for easy access and manipulation of specific data fields throughout the simulation process.

Each structure encapsulates relevant data attributes, such as transformer ratings, cable types, and power ratings, linking them directly to their respective components in the physical layout of the wind farm or PV system. This methodical encapsulation not only streamlines the data flow within the simulation but also enhances the clarity and maintainability of the code. By centralising component data within structured entities, the model facilitates interactions between components and ensures that all operations on data, from input reading through processing to output generation, are both accurate and efficient. Furthermore, these structures are dynamically updated or referenced during the simulation to reflect real-time changes or conditions within the system, such as updates in the tilt and orientation of PV modules or changes in wind turbine operational parameters. The structured approach to data management significantly aids in maintaining a clear separation of concerns within the model, where each segment of the system is handled discretely yet remains interlinked through shared data structures.

3.1.5. Calculation of In-Plane Irradiance

The estimation of in-plane irradiance is a critical component in accurately simulating PV system performance. This process involves determining the solar position, decomposing global irradiance into its direct and diffuse components, and calculating the POA irradiance based on these components.

Solar Position Calculation

The solar position, which includes the solar azimuth and elevation angles, is crucial for determining the angle of incidence of solar radiation on the PV array. This is calculated using a function, which employs basic astronomical equations. This function returns the zenith and azimuth angles, which are essential for further irradiance calculations. The solar azimuth angle indicates the sun's relative position from north, and the elevation angle represents the height of the sun in the sky relative to the observer's horizon [56].

Decomposition of Global Irradiance

The decomposition of Global Horizontal Irradiance (GHI) into Direct Normal Irradiance (DNI) and Diffuse Horizontal Irradiance (DHI) is essential for accurate solar energy simulations, especially in regions with limited direct measurements of DNI and DHI. This decomposition is necessary when calculating the POA irradiance on a module and is crucial when updating the POA irradiance after running the shading model.

The model utilised for decomposing GHI into DNI and DHI employs empirical relationships derived from measured irradiance data [57]. It calculates the clearness index (K_T) and the diffuse fraction (K), which are critical for the decomposition process. The clearness index is defined as the ratio of the global irradiance (G) to the extraterrestrial irradiance (G_0):

$$K_T = \frac{G}{G_0} \tag{3.1}$$

The diffuse fraction (K) is defined as the ratio of diffused horizontal irradiance (D) to the global horizontal irradiance (G):

$$K = \frac{D}{G} \tag{3.2}$$

Using these indices, the model applies empirical equations to estimate DHI and DNI from GHI. For instance, the diffuse irradiance can be estimated from the clearness index using a sinusoidal relationship in equation 3.3:

$$D = G \times (a + b \times \sin(c \times K_T + d)) \tag{3.3}$$

Where a, b, c, and d are empirical constants determined from regression analysis of historical irradiance data. The direct normal irradiance is then calculated by subtracting the diffuse component from the global irradiance and adjusting for the solar zenith angle (θ) as done in equation 3.4:

$$DNI = \frac{G - D}{\cos(\theta)} \tag{3.4}$$

Plane-Of-Array Irradiance Calculation Before Considering Shading

With the direct and diffuse components defined, the irradiance on the plane of the array (POA) is calculated by adjusting for the angle of incidence and the array's orientation and tilt. The direct component is adjusted by the cosine of the angle of incidence, while the diffuse component is isotropic and also influenced by the sky view factor. The reflected component is calculated based on the ground albedo, which in this model is assumed to be 0.06 [58], contributing to the total irradiance on the array:

$$I_{POA} = I_{bB} + I_{dB} + I_{rB} \tag{3.5}$$

where I_{bB} is the direct irradiance on the plane, I_{dB} is the diffuse irradiance, and I_{rB} is the reflected irradiance from the ground. These components are calculated as follows:

$$I_{bB} = R_b \cdot I_{bh}, \quad I_{dB} = R_d \cdot DHI, \quad I_{rB} = R_r \cdot GHI \cdot \text{albedo} \tag{3.6}$$

Here, R_b, R_d, and R_r are the view factors for the beam, diffuse, and reflected components respectively, which depend on the geometric configuration of the array and the position of the sun. The Perez sky diffuse model is used to compute R_d. These calculations collectively enable the accurate estimation of the irradiance that a PV module in a specific layout would receive, which is critical for performance simulation and subsequent energy yield analysis.

3.1.6. Shading Model & DC Power Calculation

The simulation incorporates a shading model that is vital for assessing the impact of the closest wind turbine on the plane of array (POA) irradiance of each solar module on the floating platforms. This model dynamically updates the POA irradiance by calculating the extent of shading imposed by the turbines based on their relative positioning. The adjustments to the POA irradiance are critical for accurately simulating the photovoltaic output, as shading can significantly reduce the energy yield of affected modules. Detailed mechanics of this shading model, including its integration into the overall simulation framework and its effects on the system's efficiency, are further elaborated in Section 3.3.

The final section of the simulation involves the calculation of DC power output from the solar modules, which is done by using module characteristics, plane of array (POA) irradiance, and module temperature. This calculation uses the electrical characteristics of the solar modules, such as current-voltage (IV) curves, along with real-time environmental conditions to estimate the power output accurately. The varying POA irradiance, influenced by factors like shading and orientation, and the temperature-dependent efficiency of the modules, are key determinants in this process. This procedure ensures that the power output reflects realistic operational conditions and provides a robust basis for analysing overall system performance. Details on the methodologies employed and the algorithms used are further explored in Section 3.4.

3.2. Tilt Model

The tilt model in this thesis refers to the mathematical model developed in [43] used to estimate the tilt and azimuth angle of a particular type of floater. The code is open source and has been used with modifications only to the input parameters for the purposes of this thesis. The workflow of the tilt model described graphically can be seen in figure 3.2.

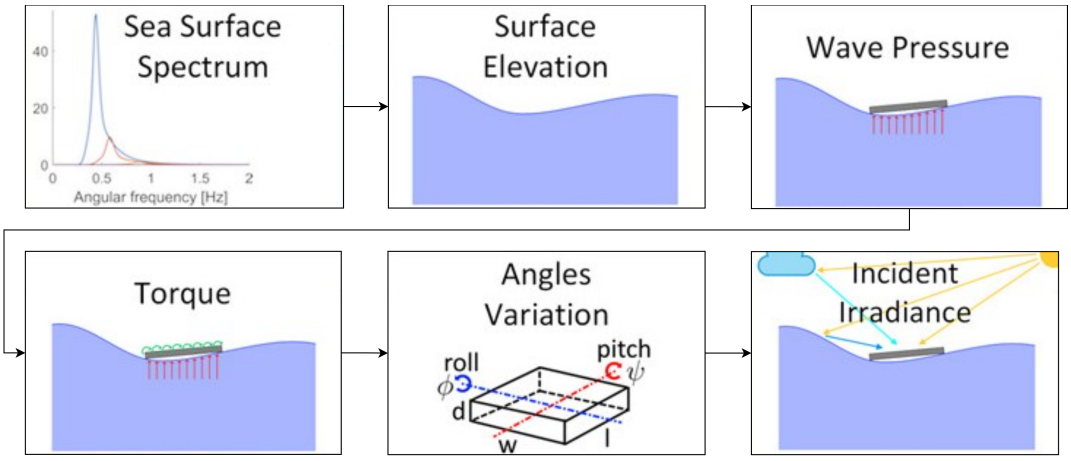

Figure 3.2: Graphical Workflow of the Tilt Model. Figure Derived From [43]

The initial stage of the tilt model involved selecting the appropriate type of wave to simulate based on its impact on floating bodies. In [43] the chosen criterion was that only waves with wavelengths comparable to the dimensions of the floating body would significantly affect it. Therefore, gravity waves, which are generated by consistent winds over large distances and have wavelengths between 1.5 and 900 meters, were selected. These wavelengths match the scale of the floaters used in the simulation model which has dimensions of 40 m x 40 m.

To describe the motion of the waves, linear water wave theory has been used in this work which simplifies the interaction between sea waves and floating bodies by making the following assumptions:

- The floating body is smaller than the wavelength: Assuming the floating body is smaller than the wavelength avoids complex wave reflection and scattering calculations. This simplifies the interaction model by treating the floating body as passively driven by the waves.
- Water is incompressible: Assuming water is incompressible eliminates the need to consider changes in water density and volume, simplifying the fluid dynamics equations.
- Viscosity is negligible: Ignoring viscosity assumes no energy loss due to water resistance, simplifying the energy balance and force calculations on the floating structure.
- Coriolis for is ignored: Neglecting the Coriolis force removes the need to account for rotational effects of the Earth, simplifying the force and motion equations.
- Deep water conditions apply: Applying deep water conditions assumes that wave characteristics (e.g., speed and pressure distribution) are simplified, focusing on wave heights and lengths without near-shore complexities.

These simplifications significantly reduce the computational complexity of the model while retaining essential dynamics, allowing for a more simplified analysis of the interactions between sea waves and floating structures.

3.2.1. Sea Surface Spectrum

The JONSWAP spectrum, was utilised within the tilt model to accurately characterise the sea states encountered in the North Sea, where the original data for this spectrum were gathered. The Joint North Sea Wave Project (JONSWAP) conducted extensive measurements that form the basis of this spectrum

model, which is tailored to describe the complex wave dynamics in this region [59]. The JONSWAP spectrum is particularly effective in depicting waves of varying heights, duration, and shapes, reflecting the stochastic nature of sea conditions with limited predictability. A system of equations described in [60] was implemented to derive the spectrum as a function of wind speed, capturing the essential characteristics of the sea's response to wind dynamics. Figure 3.3 illustrates the derived spectra, showing how different wind speeds influence wave patterns.

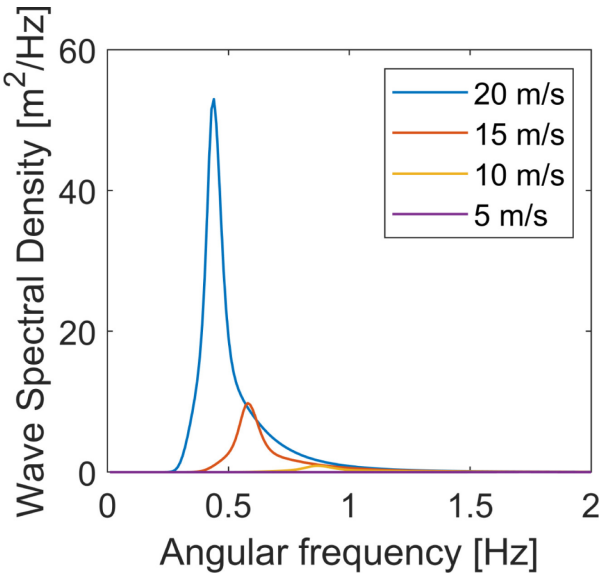

Figure 3.3: JONSWAP Spectra for Different Wind Speeds. Figure From [43]

3.2.2. Surface Elevation Calculation

The sea surface elevation is calculated by superposing waves of different wavelengths and amplitudes based on Fourier's theory. This requires discretisation for numerical implementation, employing the approach in [61] where amplitude components of the spectral equation are treated as random variables. The resulting surface elevation equation is represented in equation 3.7 [62].

$$\begin{aligned} \eta(x,t) &= \sum_{n=1}^{N/2} \left(a_n \cdot \cos\left(k_n \cdot x - \omega_n \cdot t\right) + b_n \cdot \sin\left(k_n \cdot x - \omega_n \cdot t\right)\right) \\ a_n &= rn_{a_n} \cdot \sigma_S \\ b_n &= rn_{b_n} \cdot \sigma_S \end{aligned} \tag{3.7}$$

where $\eta(x,t)$ is the surface elevation [m] at point x and time t, a_n and b_n are Fourier amplitudes [m]. ω_n is the angular frequency [Hz] of wave n which is related to the wave number k_n [m^{-1}] by the dispersion relation for deep water conditions given by equation 3.8.

$$\omega_n^2 = g \cdot k_n \tag{3.8}$$

where g is the gravitational constant.

3.2.3. Wave Pressure Calculation

The interaction between the floating solar plant and sea waves is described using the simplified Froude-Krylov theory. This theory estimates the force exerted by waves on a structure by determining the pressure variations around it [63]. Several assumptions are made:

- The wave field is unaffected by the floating structure.
- The floating body is considered rigid.
- Movements on the plane parallel to the sea surface and rotation around z-axis are neglected due to anchoring.
- The floating body is positioned at $z = 0$ relative to sea level.

The wave pressure p under a progressive wave is calculated as in equation 3.9:

$$p(x, z, t) = -\rho \frac{\partial \phi}{\partial t} - \rho \cdot g \cdot z \tag{3.9}$$

where ρ is the seawater density and ϕ is the velocity potential function, related to the surface elevation η as in equation 3.10:

$$\eta(x, t) = -\frac{1}{g} \frac{\partial \phi}{\partial t}\bigg|_{z=0} \tag{3.10}$$

For a floating body at $z = 0$, the pressure simplifies to equation 3.11:

$$p(x, z = 0, t) = \rho \cdot g \cdot \eta \tag{3.11}$$

3.2.4. Torque Calculation

The force F acting on the floater is the integral of this pressure over the area A is shown in equation 3.12:

$$F = \int p \, dA = \int_{-w/2}^{w/2} \int_{0}^{l} p \, dy \, dx \tag{3.12}$$

where w and l are the width and the length of the floater in the x and y-axis respectively. The torque τ resulting from this force is as expressed in 3.13:

$$\tau = F \cdot x = \int_{-w/2}^{w/2} \int_{0}^{l} p \cdot x \, dy \, dx \tag{3.13}$$

3.2.5. Roll and Pitch Calculation

The rotational angle θ of the floater is obtained from the relation between torque, moment of inertia I, and angular acceleration α is shown in equation 3.14:

$$\tau = I \cdot \alpha = I \cdot \frac{\partial \omega \theta}{\partial t} = I \cdot \frac{\partial^2 \theta}{\partial t^2} \tag{3.14}$$

Considering two axes of rotation, the moments of inertia around the x- and y-axes are calculated as in equation 3.15:

$$I_x = \frac{1}{12} \cdot m(l^2 + d^2) \quad \text{and} \quad I_y = \frac{1}{12} \cdot m(w^2 + d^2) \tag{3.15}$$

where m is the mass and w, l, and d are the dimensions of the floating body.

3.2.6. Coordinate Transformation to Obtain Tilt and Azimuth Angles

Using these equations the roll with the x-axis being the rotational axis and the pitch along the y-axis are found however to be able to use these values to find the POA irradiance, a coordinate change is done first. The simulation framework needs tilt α and azimuth A_M at each time step, derived from roll ϕ and pitch ψ using equations 3.16 and 3.17:

$$\tan A_M = \frac{\sin \psi}{\tan \phi} \tag{3.16}$$

$$\cos \alpha = \cos \psi \cdot \cos \phi \tag{3.17}$$

3.3. Shading Model

This section provides a detailed analysis of the shading model and its components. It begins with the assumptions made in the shading model, followed by the geometry of the wind turbine. Next, the assignment of indices to nodes is discussed, along with the azimuth angles considered for shading. The subsequent parts cover the methodology for finding the vertices of shadow boundaries and shapes, and identifying the nodes within these approximate boundaries. Finally, the section concludes with the irradiance calculation for each module.

3.3.1. Assumptions Made in the shading model

In the shading model, the solar panels are assumed to be flat, i.e., without any tilt, to simplify the computational demands. This assumption is warranted considering that the tilt angle of the floating solar installations typically remains below 5 degrees throughout most of the year. Consequently, the variation in the shaded area induced by tilting is minimal and can reasonably be approximated as constant. Furthermore, the direction of the tilt may vary, either towards or away from the sun, which implies that, on average, the alterations in the shaded area due to tilt are not substantial.

In the analysis of the diffused irradiance component, the assumption of negligible shading by the wind turbine is justified by the substantial distance separating the turbine from the floating solar installation. Specifically, with the turbine situated at least 110 meters away, the sky view factor—considering no other obstacles, which is a reasonable assumption in the marine setting of the floating panels—remains substantially unaffected. The circumference of the base of this theoretical hemisphere at this distance is calculated as $2\pi \times 110$ meters. Given that the turbine's span obstructs not more than 6 meters of this circumference, this represents less than one percent of the total sky view factor. Even assuming an infinitely tall tower, the minimal percentage of the horizon that is obscured substantiates the decision to neglect the shaded part of the diffused irradiance, thereby avoiding unnecessary computational costs.

The mathematical substantiation can be illustrated by the following simple equation 3.18:

$$\text{Sky View Factor Reduction} \approx \frac{\text{Obstructed Length}}{\text{Total Circumference}} = \frac{6}{2\pi \times 110} \approx 0.0087, \tag{3.18}$$

which confirms that the impact on the sky view factor is indeed negligible.

3.3.2. Geometry of the Wind Turbine

The geometry of the wind turbine in the model is simplified for computational efficiency. The tower of the turbine is approximated as cylindrical, while the three blades, positioned symmetrically at intervals of 120 degrees, are modelled with conical shapes to approximate their actual aerodynamic profiles. Additionally, the nacelle of the wind turbine is represented as a cuboid. Figure 3.5 depicts the geometric approximations used for the wind turbine. Furthermore, Table 3.4 provides a detailed list of the dimensions for the components of the wind turbine as considered in the simulation model.

The geometries selected for the wind turbine in this study are designed such that the boundary of the shadow they cast forms simple polygons. This design choice is strategic, as it significantly reduces the computational complexity of the shading model. By simplifying the shadow boundaries to polygons, the calculations required to determine shading effects on the floating PV clusters are streamlined. This approach enhances the efficiency and speed of the simulation, allowing for more accurate and timely analysis without compromising the precision needed for effective energy yield assessments.

3.3.3. Assignment of Indices to Nodes

For the purposes of the simulation, both the floaters and the solar modules mounted on them are discretised into nodes. The spacing between these nodes is a variable parameter, influencing the model's resolution and the accuracy of power output calculations. Adjusting node spacing affects the computational demand: finer resolutions, while more accurate, significantly increase computational time due to the shading model. This modelling approach allows for the extraction of detailed irradiance data at a modular level, facilitating an analysis of how string arrangements might contribute to power losses.

Parameter	Dimension [meters]
Hub height	140
Rotor diameter	220
Tower width	6
Nacelle (L x B x H)	10 x 8 x 4
Blade base diameter	4

Figure 3.4: Wind Turbine Dimensions

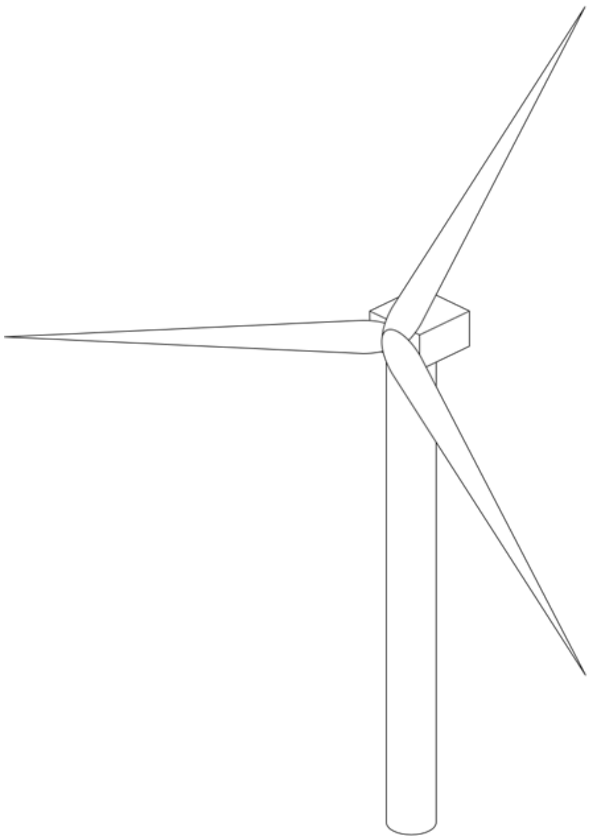

Figure 3.5: Wind Turbine Geometry

Such losses occur due to variations in the IV curve formation and discrepancies in the maximum power points across different strings.

Each node within the model is assigned specific module and string index numbers, enabling precise differentiation and analysis of shading effects on each module's irradiance. Figure 3.6 displays a visualisation of the floater, with modules color-coded according to their index numbers in the strings.

3.3.4. Azimuth Angles Considered for Shading

Due to the computational intensity of the shading model, initial computations are made to determine the angles at which shading is possible, thereby restricting the model's operation to conditions where shading effects are likely. This pre-computation step involves identifying the minimum azimuth angle for which shading on a particular floater is feasible. Figure 3.7 illustrates the scenario for a specific floater, highlighting the conditions under which the shading model is activated.

In the simulation, the wind turbine is modelled as a cylindrical structure with a diameter equal to that of the rotor. The shadow cast by the turbine is analysed by tracing its boundary lines to ascertain whether they intersect with the floater. This method ensures that the shading model is only engaged when the floater lies within the projected shadow path, optimising computational resources and model efficiency.

This approach employs a simplified representation of the wind turbine's cylindrical boundary using points spaced at regular intervals. This discretisation can lead to minor inaccuracies in determining the exact intersections of the turbine's shadow with the floater. As a result, there are instances where the actual azimuth angle at which shading occurs may be underestimated. This occurs when the tangential shade boundary line representing the cylinder crosses the floater, but the spaced points fail to capture this intersection fully. Consequently, the shading model might omit certain shading events, leading to

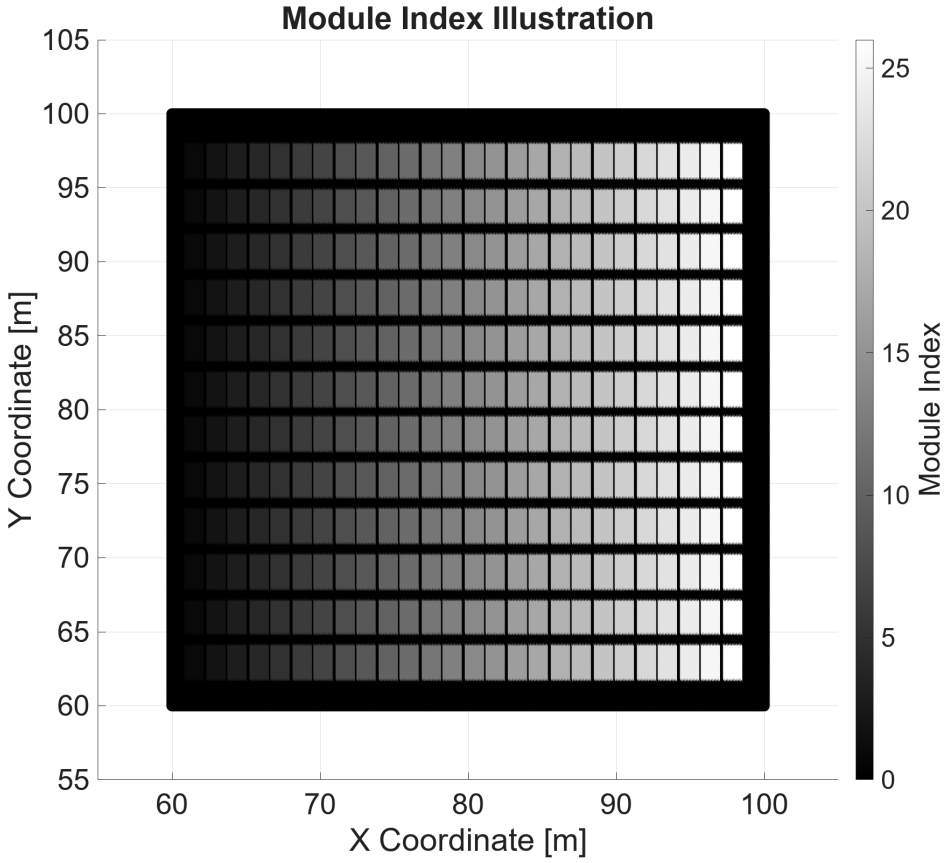

Figure 3.6: Module Index Number Assignment Illustrated With a Colormap on a Floater

a slight overestimation of power output. In a simulated scenario where a floater was positioned 200 meters north of a wind turbine, this methodological error resulted in a power calculation error of approximately +0.023%. Despite these small inaccuracies, the method remains valid and effective for most practical purposes.

3.3.5. Finding the Vertices of Shadow Boundaries

To delineate the shadow boundaries, it is essential first to establish the precise coordinates, dimensions, and orientations of the wind turbine. These include the hub height, tower centre position, blade azimuth angle, yaw angle, blade endpoints and nacelle corners. Based on the position of the sun—specifically the solar elevation and azimuth angles—the length of the shadows cast by the turbine tower and blades are calculated and from this length and solar azimuth angle, the endpoints of the shadow boundary are calculated. This calculation employs a specific equation designed to accurately model the shadows based on the geometric and positional data. Figure 3.8 from [64] illustrates the methodology employed for this calculation, demonstrating the application of the equations 3.19 and 3.20 in determining shadow endpoints:

$$\text{Shadow Length} = h \times \tan(\theta_{\text{zenith sun}}) \tag{3.19}$$

$$\text{Shadow Azimuth} = \phi_{\text{azimuth sun}} + 180^\circ \tag{3.20}$$

Upon determining the endpoints of the shadows cast by the wind turbine's structural components, the subsequent step involves tracing these points to the endpoints of a line orthogonal to these points, situated proximally to the wind turbine. The length of this orthogonal line is contingent upon the specific component of the turbine being considered—either the tower or the blade. Specifically, the line's length

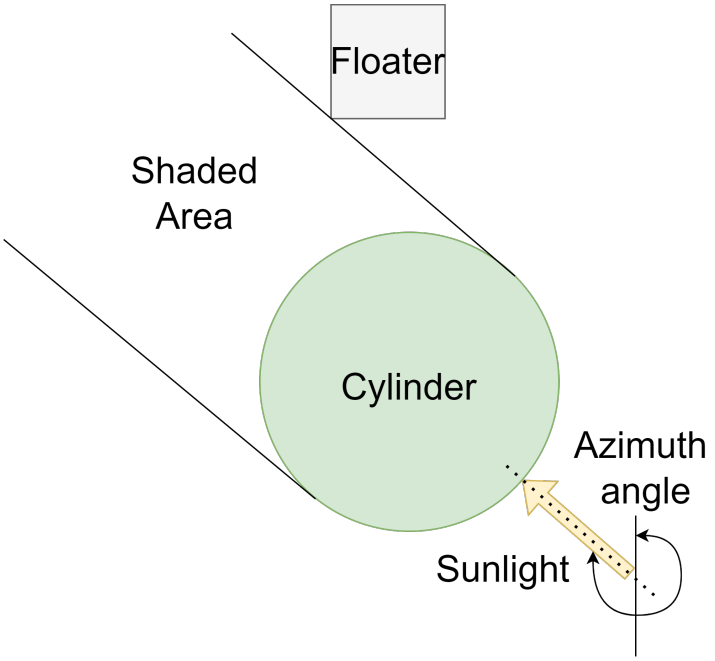

Figure 3.7: Minimum Azimuth Angle Considered to Run the Shading Model

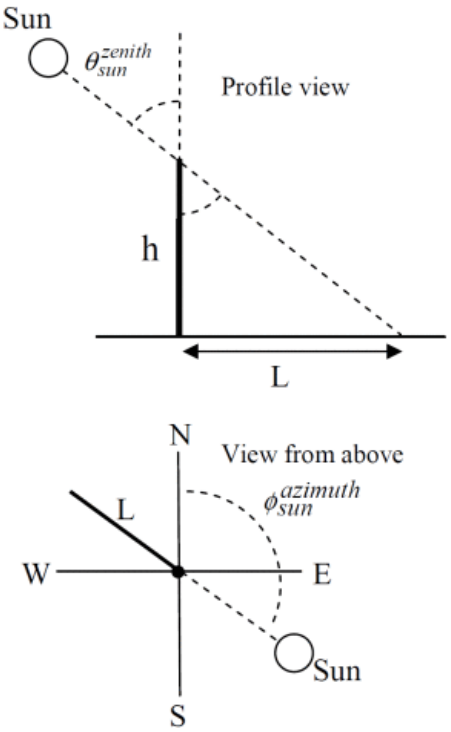

Figure 3.8: Illustration of How the Length of the Shadow Is Calculated. Derived from [64]

varies according to the base diameter of the component responsible for the shadow. For the turbine tower, the width of the tower significantly influences the length of this orthogonal line. Similarly, for the blades, their rotational base diameter dictates the length of this orthogonal line. This methodical approach allows for a precise mapping of the shadow's reach and configuration, ensuring that all potential shading effects on the floaters are accurately assessed and incorporated into the shading model.

3.3.6. Finding the Nodes Within This Approximate Boundary

Upon establishing the vertices that delineate the shadow boundaries-a rectangle for the turbine tower and a triangle for the blades—the next critical step involves identifying the nodes within these boundaries. This identification is efficiently executed using MATLAB's `inpolygon` function. This function is selected for its computational speed and accuracy, surpassing the performance of any custom-coded alternatives that could be developed for this purpose.

The `inpolygon` function cross-references the coordinates of each node against the defined polygonal boundary (either rectangular or triangular, depending on the turbine component). The nodes within these boundaries are then processed to update the solar irradiance impact matrix. In this matrix, each node is assigned additional binary shading indices where a value of '1' indicates the node is shaded, and '0' indicates it is not shaded. This binary shading index crucially informs subsequent calculations regarding the PV output efficiency under various shading scenarios.

The effectiveness of the `inpolygon` function in identifying shaded nodes is depicted in a scatter plot, which illustrates the shadow of the wind turbine on the floater during a specific instance. Figure 3.9 shows this distribution, highlighting the precise areas impacted by shading, and providing a clear visual representation of the shadow of the wind turbine.

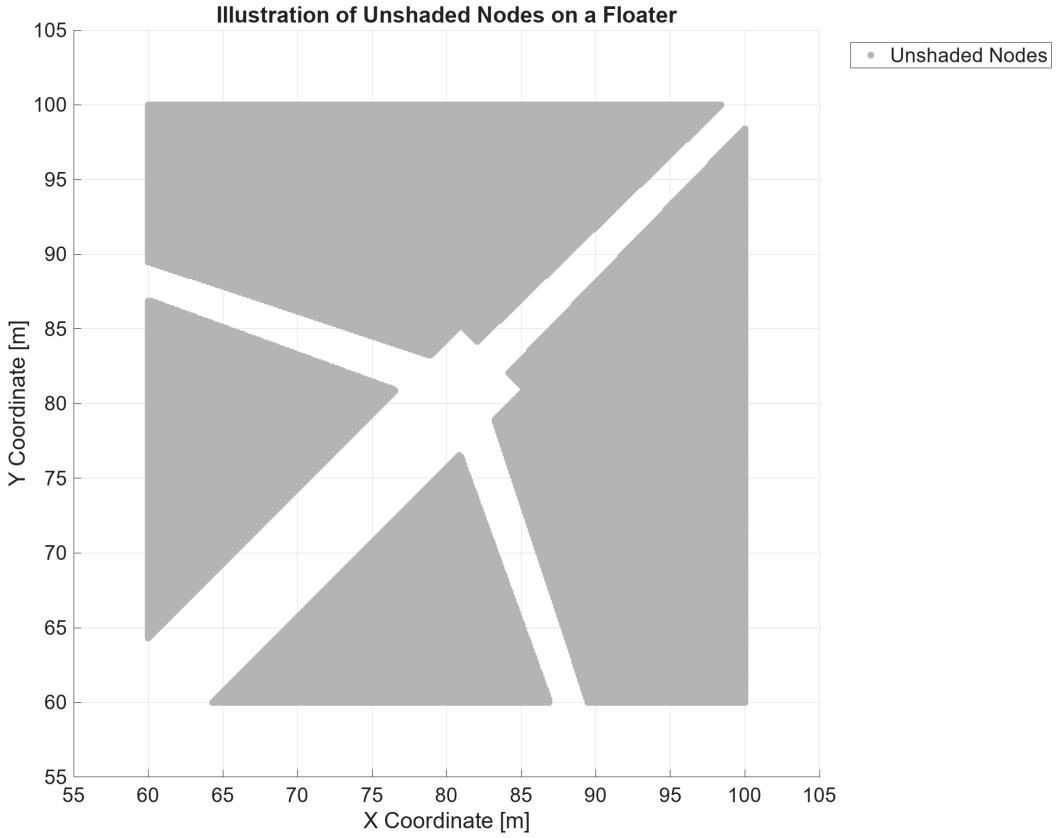

Figure 3.9: Illustration of the Shade Caused by a Wind Turbine at [0,0] on a Floater When the Blade Azimuth Angle = 0°, Wind Direction = 225°and, Solar Azimuth Angle = 225°, Solar Elevation Angle = 50°

3.3.7. Irradiance Calculation of Each Module

The new effective plane of irradiance for the solar modules is calculated by adjusting for shading impacts. This involves compiling a matrix with node coordinates, string assignments, module assignments, and shading data, which is then filtered to remove any entries without module or string assignments. Unique combinations of string and module indices are identified to calculate the total shading

occurrence count for each combination. The proportion of shading for each module is computed by dividing the total shading occurrences by the number of nodes for that module.

This proportion is used to adjust the direct irradiance received by each module. Specifically, the effective POA irradiance for each module is calculated by subtracting the product of the direct irradiance and the proportion shaded from the total irradiance. This method ensures that the irradiance values are adjusted to reflect the actual light exposure after shading.

Figure 3.10 displays a plot of the modules, categorized by the effective POA irradiance they receive after shading. This plot provides a clear visualization of how shading influences the irradiance received by different modules.

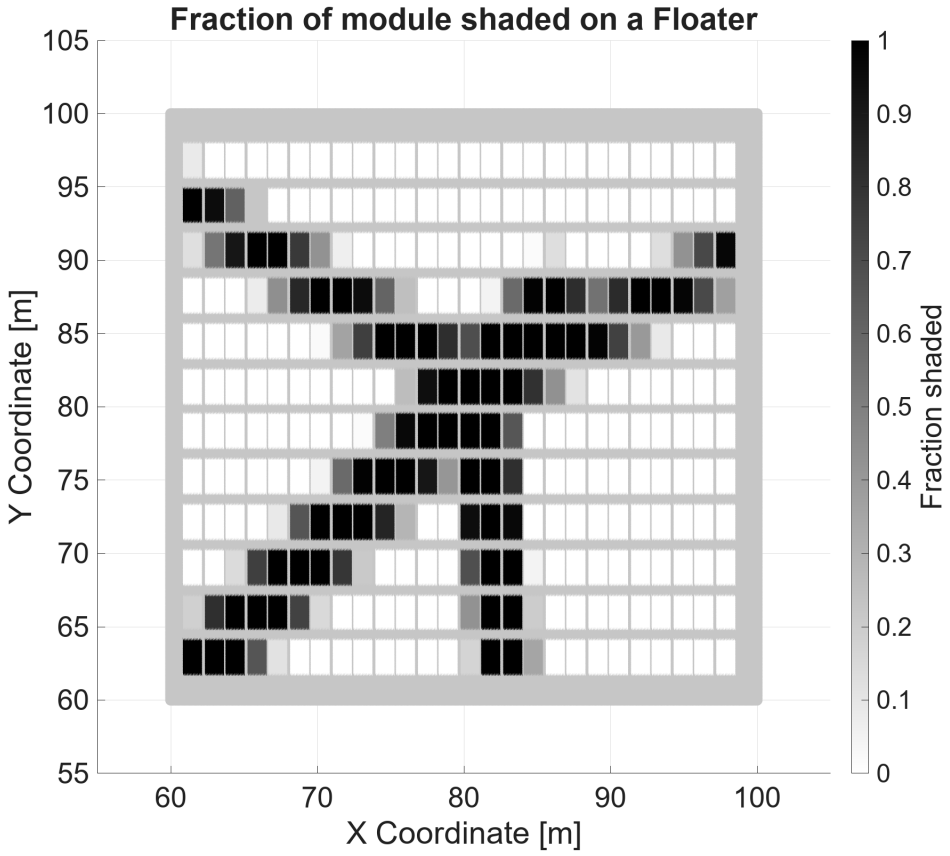

Figure 3.10: Scatter Plot for the Proportion of Shade of a Module

3.4. DC Power Calculation

In this section, the calculation of the DC power generated at the DC side of the inverter neglecting DC cable losses. This part of the model runs after the shading model which calculated the POA irradiance for each module.

3.4.1. Estimation of Module Temperature

An accurate estimation of the temperature of photovoltaic (PV) modules is crucial for understanding their performance and efficiency. In an offshore floating PV installation this effect is more important to capture as the modules operate at a lower temperature due to cooling effect and higher wind speeds than in in-land installations which increases the energy yield [65, 66].

The module temperature is determined by a function that incorporates air temperature, irradiance, and wind speed, following the modelling approach proposed in [67] in their study on photovoltaic cells. This method, selected for its detailed consideration of environmental variables, utilises a set of coefficients which are calculated empirically that relate these environmental factors directly to the module temperature. Specifically, the model calculates the module temperature as a linear combination of the air temperature, irradiance, and wind speed, adjusted by coefficients that reflect the thermal properties and exposure characteristics of the solar panels as seen in equation 3.21.

$$T_{\text{mod}} = c_1 \cdot T_{\text{air}} + c_2 \cdot I_{\text{rad}} + c_3 \cdot V_{\text{wind}} + c_4 \tag{3.21}$$

Where c_1, c_2, c_3, and c_4 are coefficients derived from empirical data and manufacturer specifications that account for the thermal rise due to irradiance and the cooling effect of wind. T_{air} is the air temperature, I_{rad} is the POA irradiance of the module and, V_{wind} is the estimated speed of the wind at 2m height from sea level. This formula ensures that the temperature calculation is sensitive to real-time changes in environmental conditions, thereby providing a dynamic input into the subsequent calculation of DC power output.

The selection of this model is based on its ability to provide a realistic simulation of the module's thermal behaviour under various environmental conditions. This temperature modelling is essential for the next step in the simulation process, where these temperatures, along with irradiance data, are used to estimate the voltage, current and subsequently power produced by the PV modules under varying environmental influences.

3.4.2. Calculation of I-V Curve for Solar Modules

The I-V curve for a solar module is calculated using a single-diode model alongside series and shunt resistances to reflect real-world inefficiencies. This model is essential for understanding how solar panels will perform under various environmental conditions, including changes in irradiance and temperature.

Assumptions in the I-V Curve Modelling

In the development of the I-V curve model for the floating PV modules, certain simplifications were adopted to streamline the computations and focus on the core objectives of the thesis. Notably, the model does not incorporate the effects of bypass diodes typically used in PV modules to mitigate the impact of partial shading. This assumption is primarily due to the spatial resolution of the nodes used in simulating the floating platform, which are larger than individual solar cells and the width of the strings in the considered PV panel. Accurately modelling the influence of individual bypass diodes would require a finer resolution to capture variations within a module, as each diode protects a subset of cells within the module. Additionally, including bypass diodes in the model would significantly increase computational complexity without substantially influencing the goal of this thesis, which is to determine a placement strategy for OFPV clusters relative to wind turbines.

Moreover, the model assumes uniform irradiance across each module when shaded. This assumption reduces the complexity of the simulation and is justified because the primary objective is to assess macro-level interactions between the solar array and environmental factors, rather than detailed micro-level interactions within each module. This approach allows for a more streamlined analysis and is sufficient for understanding the overall system behaviour under typical operational conditions. It ensures the focus remains on evaluating the significant effects of relative positioning and environmental influences on energy production, thereby providing robust insights needed for strategic planning and development of integrated solar and wind energy systems.

Photocurrent Calculation

The photocurrent (I_{ph}) for the solar module is derived from Equation 3.22:

$$I_{ph} = (I_{sc} + k_i \cdot (T_{module} - T_{ref})) \cdot \frac{I_{rad}}{G_{ref}} \tag{3.22}$$

where I_{sc} is the short-circuit current under standard test conditions, k_i is the temperature coefficient of the short-circuit current, T_{module} is the module temperature, T_{ref} is the reference temperature which is 298.15 Kelvin, I_{rad} is the irradiance, and G_{ref} is the reference irradiance which is 1000 W/m^2. This equation adjusts the photocurrent based on the actual irradiance and temperature relative to standard test conditions.

Reverse Saturation and Saturation Current Calculation

The reverse saturation current (I_{rs}) is calculated using Equation 3.23:

$$I_{rs} = \frac{I_{sc}}{\exp\left(\frac{q \cdot V_{oc}}{N_s \cdot k \cdot A \cdot T_{module}}\right) - 1} \tag{3.23}$$

where q is the electron charge, V_{oc} is the open-circuit voltage, N_s is the number of cells in series, k is the Boltzmann constant, A is the ideality factor of the diode.
The saturation current (I_s) is calculated using the diode Equation 3.24 adjusted for temperature:

$$I_s = I_{rs}\left(\frac{T_{module}}{T_{ref}}\right)^3 \exp\left(\frac{q \cdot E_g}{k \cdot A}\left(\frac{1}{T_{ref}} - \frac{1}{T_{module}}\right)\right) \tag{3.24}$$

where E_g is the band gap energy of the semiconductor. This formula accounts for variations in the reverse saturation current due to temperature changes, which significantly affect the diode characteristics.

I-V Curve Computation

The parameter z for the Lambert W function is computed using Equation 3.25:

$$z = \frac{R_s I_s}{A V_{th}} \cdot \frac{R_{sh}}{R_{sh} + R_s} \exp\left(\frac{R_{sh}}{R_{sh} + R_s} \cdot \frac{R_s(I_{ph} + I_s) + V}{A V_{th}}\right) \tag{3.25}$$

where R_s is the series resistance, R_{sh} is the shunt resistance, I_{ph} is the photocurrent, A is the ideality factor, and V is the voltage across the solar cell.

Using the Lambert W function, the current I is then calculated using Equation 3.26:

$$I = \left(\frac{R_{sh}}{R_{sh} + R_s}\right)(I_{ph} + I_s) - \frac{V}{R_{sh} + R_s} - \frac{A V_{th}}{R_s} W(z) \tag{3.26}$$

This equation is solved iteratively over a range of voltages to generate the I-V curve. This approach, utilising the single-diode model with empirical corrections for temperature and irradiance, provides a framework for predicting solar cell performance. By accurately modelling these characteristics, we can better understand and optimise the energy output of photovoltaic systems under varying environmental conditions.

3.4.3. Generation of I-V Curves for Series-Connected Solar Module Strings

To accurately assess the performance of photovoltaic (PV) systems under real-world conditions, it is essential to model the I-V characteristics of series-connected solar module strings. This modelling is particularly critical in scenarios where module strings are subjected to non-uniform irradiance due to shading or other environmental factors.

Handling Non-Uniform Irradiance

When modules within a string experience varying levels of irradiance, the output I-V curve of the string is influenced by the module receiving the least amount of sunlight. This is because, in series connections, the string current is limited by the least illuminated module, akin to the behaviour in electrical circuits where current through a series path is dictated by the component with the minimum current carrying capacity.

To model this, the I-V curve for each module is first calculated based on its specific irradiance and temperature conditions. The total current (I) for each voltage (V) in the string's I-V curve is determined by the lowest current available from all modules at that voltage. This approach simulates the behaviour of ideal string diodes, which prevent any amount of reverse biasing and protect less illuminated modules by allowing the current to bypass them.

Uniform Irradiance Handling

Under uniform irradiance conditions, all modules within a string are exposed to the same level of solar radiation. This uniformity simplifies the computation of the string's I-V curve, as the I-V curves for all modules will be identical. Therefore, the string's total current at each voltage point is simply the sum of the currents from each module at that voltage. This method significantly reduces computational complexity and ensures quick computations without sacrificing accuracy for scenarios where shading does not affect the solar array.

3.4.4. Power and Energy Calculations for the Floating PV System

This subsection elaborates on the methodologies employed to compute the power output at every time step and annual energy yield of the PV system, underlining the use of an ideal maximum power point tracker (MPPT).

Power Curve Generation

The power curve of a PV module is derived from the product of the voltage (V) and current (I) across the module as shown in equation 3.27:

$$P_{\text{curve}} = V \cdot I \tag{3.27}$$

This equation calculates the instantaneous power for combinations of voltage and current generated with a certain resolution for voltage from 0 to V_{oc} under varying irradiance conditions. The power curve is crucial for identifying the operating points where the modules can deliver maximum power output.

Maximum Power Point Tracking

To maximise the energy output from each PV module, the system is assumed to employ an ideal MPPT. This simply means that the maximum power from the Power-Voltage curve of a string is found and taken as the DC power output of that particular PV string.

Aggregate Power and Energy Calculations

The total power output for the PV floater is calculated by summing the power of all strings within the floater and then averaging these over the number of blade angles (in this simplified model, considered as one) considered in the static shading model in the 10 minute time frame. The annual energy yield for the cluster is then calculated by integrating the power output over time and dividing by the appropriate scaling factor to convert the result into megawatt-hours (MWh). This computation assumes that the power output is summed over ten-minute intervals throughout the year, providing an estimate of the total energy produced under typical operational conditions. Equation 3.28 is used to compute the annual energy for each floater from the power timeseries values which have a time resolution of 10 minutes and is computed in W:

$$\text{Annual Energy [MWh]} = \frac{\sum_{\text{time\_idx}=1}^{52418} P_{mpp} \cdot 10}{60 \times 10^6} \tag{3.28}$$

3.5. Supporting Tasks

This section delves into various auxiliary analyses and methodologies employed throughout the course of this project. It begins with an examination of the node spacing sensitivity analysis, highlighting how different node resolutions influence the simulation results. Following this, the section discusses the impact of the number of blade positions considered in the static shading simulation. Attention is then given to the code optimisation methods that were implemented to enhance the efficiency and performance of the simulations. An overview of the lookup table created for the I-V curve is also provided.

Additionally, this section describes the utilisation of a remote computer cluster and finally, the use of ChatGPT for this work is discussed.

3.5.1. Node Spacing Sensitivity Analysis

In the node spacing sensitivity analysis, the impact of varying the distance between nodes in a rectangular grid mesh on the speed and accuracy of the model was examined. This analysis aimed to identify an optimal balance between computational efficiency and model precision for the selection of the node spacing value in the main simulation.

Given that the dimensions of a PV module are 1.3 m by 2.3 m, the node spacing must be less than the smallest dimension, i.e., less than 1.3 m. However, with a node spacing of 1.3m, each PV module would be represented by just two nodes, leading to shading representations of 0%, 50%, or 100% when the shading model is applied. Reducing the node spacing increases the resolution, allowing for more granular shading fractions and, consequently, a more accurate model. Nonetheless, finer node spacing also results in increased computational load and longer execution times, necessitating a trade-off.

The sensitivity analysis involved calculating the annual energy output and recording the execution time for different node spacing values for a specific floater affected by shading. As shown in the table below, a node spacing value of 0.35m was identified as the most appropriate for the main simulation, offering a suitable compromise between accuracy and computational efficiency.

Node Spacing (m)	Annual Energy (MWh)	Execution Time (s)
1.0	258.15	71
0.5	257.98	86
0.35	257.95	93
0.25	257.94	111
0.1	257.94	240

Table 3.1: Node Spacing Sensitivity Analysis

This analysis underscores the importance of selecting an optimal node spacing value that balances the need for accurate shading representation with the practical considerations of computational time.

3.5.2. Sensitivity Analysis of the Number of Blade Azimuth Angles in Static Shading Model Simulations

The static shading model initially considered only a single blade azimuth angle, fixed at 0 degrees, within each 10-minute time frame. This simplification does not account for the dynamic nature of wind turbine blades, which in reality, sweep out a disc or elliptical area influenced by the yaw angle (determined by wind direction) and the solar azimuth and elevation angles. The fixed blade position assumption could lead to inaccuracies as it ignores the varying shadow cast by the rotating blades.

To address this, a sensitivity analysis was performed to evaluate the impact of considering multiple blade azimuth angles on the accuracy and execution time of the model. The analysis aimed to balance between computational efficiency and the precision of shading representation. The speed of blade rotation was deemed irrelevant for this study due to the assumption of ideal MPPT, which negates inverter losses caused by the MPPT's inability to continuously track the maximum power point. Hence an average of all the blade positions is an appropriate way of going about this analysis. In reality if the rotation of the blades is faster, that could lead to more variations in the IV curve of the PV module and thus make it harder for the MPPT of the inverter to track the maximum power point and subsequently lead to higher inverter losses.

In the analysis, different configurations were tested to understand the impact of considering multiple blade azimuth angles on the accuracy and execution time of the model. Initially, one blade azimuth

angle at 0 degrees was considered. To improve accuracy, the analysis then included two blade azimuth angles at 0 and 60 degrees, followed by three angles at 0, 40, and 80 degrees and so on. These angles were chosen based on the symmetry of the wind turbine's three blades, where angles between 0 and 120 degrees provide distinct shadow patterns, with 120 degrees being equivalent to 0 degrees due to rotational symmetry. For cases with multiple blade angles, the average power loss was calculated to account for the varying shade on the floater depending on the blade position.

The selection of angles was based on the symmetry of the wind turbine's three blades, where angles between 0 and 120 degrees provide distinct shadow patterns, with 120 degrees being equivalent to 0 degrees due to rotational symmetry. For cases with multiple blade angles, the average power loss was calculated, reflecting the variation of the shade on the floater depending on the blade position.

A scenario with 360 blade azimuth angle positions considered in the static shading model represents the most accurate model, was used as a reference to calculate the error. The analysis revealed that the error in annual energy calculation was minimal even when considering only a single blade position at 0 degrees. Therefore, for computational efficiency, the main simulation adopted this single blade azimuth angle approach.

In figure 3.11a, the annual energy is plotted against the number of blade angles considered in that position. In figure 3.11b, the time taken for the shading model to run is plotted against the number of blade positions considered. This analysis is performed for one floater that is affected by shading and is located north of the wind turbine. The array of considered number of blade azimuth angle positions is: [1, 2, 3, 4, 5, 6, 8, 10, 20, 30, 40, 60, 80, 100, 120, 240, 360].

The reasoning behind selecting 1 blade angle can be justified by the fact that the percentage error is not significant, as shown in Figure 3.11a, and it is logical to reduce the runtime of the model. Additionally, the time taken to run the shading model increases linearly with the increase in the number of blade angle positions considered, as can be seen in Figure 3.11b.

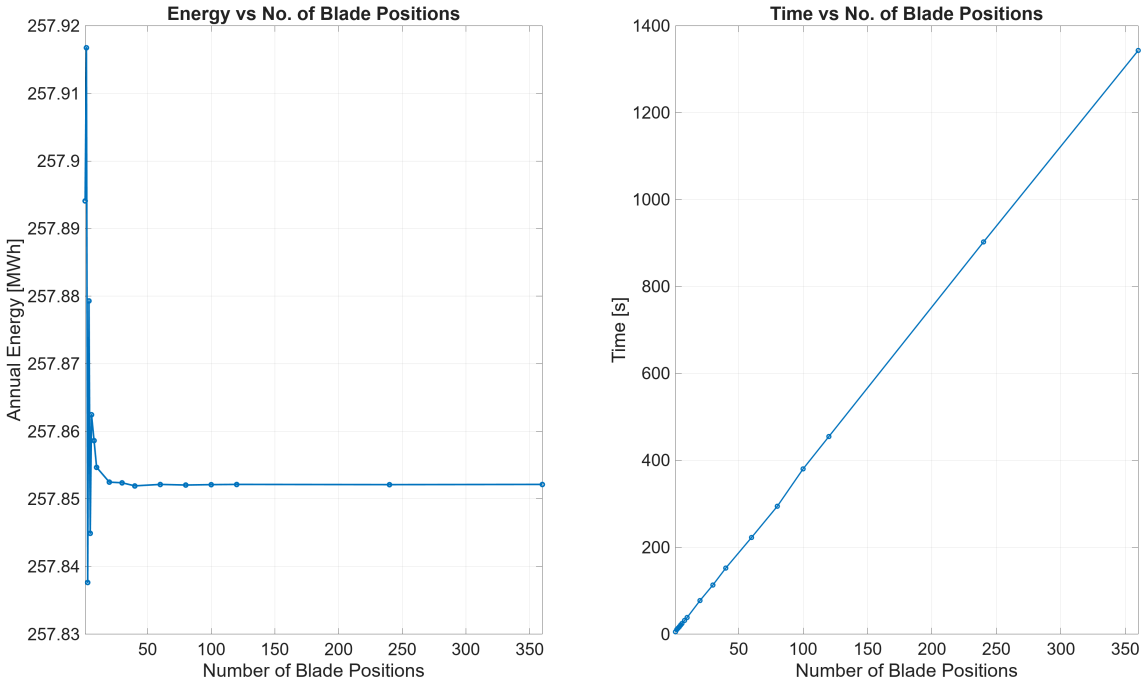

(a) Annual Energy vs. Number of Blade Azimuth Angles

(b) Runtime vs. Number of Blade Azimuth Angles

Figure 3.11: Sensitivity Analysis of Number of Blade Azimuth Angles w.r.t Accuracy and Time Taken by the Static Shading Model

3.5.3. Code Optimisation

The optimisation of the code for this project was a critical step to ensure efficient and timely simulations. The MATLAB Profiler was employed to identify functions that acted as bottlenecks and particular lines of code that significantly slowed down the execution. The primary focus was on the main simulation, which involved running the energy simulation for an entire year with the shading model for a floater grid map surrounding a wind turbine. This simulation was originally implemented using nested `for` loops: the outer loop iterated through each floater in the grid map, the middle loop iterated through each time instance, and the inner loop, which was conditionally executed, iterated through the strings on the floaters if shading was detected. The outer loop is run using `parfor` loops to leverage parallel processing and speed up the execution of the code. This comprehensive yet computationally intensive approach necessitated various optimisation techniques.

To enhance the execution speed, several logical tricks were employed. Firstly, the entire time step was skipped if no irradiance data was available, eliminating unnecessary computations. When no shading occurred on a string, the IV curve for the string was obtained by simply scaling the IV curve of a single module, leveraging a mathematical simplification to avoid redundant calculations. Furthermore, the shading model, a significant bottleneck, was executed only when shading was physically possible, reducing the frequency of its computation.

A function was also developed to dynamically create the layout of the floaters based on input parameters such as floater dimensions, size of the grid map, and the centre of the floater. This function returned the spatial data of the floaters in a cell, facilitating the execution of shading models. This dynamic layout generation not only streamlined the initial setup but also ensured that the spatial configuration could be easily adjusted for different simulation scenarios.

Overall, these optimisation strategies played a crucial role in achieving the performance required for the simulations, enabling more extensive and detailed analyses within a reasonable time-frame of 3 hours for a grid map containing 676 reference floaters surrounding a wind turbine. This grid map or collection of floaters is centred at [0, 0] and the wind turbine is placed at [0, -360] as shade due to it would be more prominent in the north then south so it was placed such that there are more floaters north of it than south. The time taken for the code to run for a particular floater is also dependent on it's relative position to the wind turbine as that dictates the number of times the shading model runs which is one of the major bottlenecks of the code.

3.5.4. Lookup Table for IV Curve

One of the strategies employed to accelerate the run time of the code was the creation of a three-dimensional lookup table storing the IV curve of the photovoltaic module for different irradiance and module temperature values. Solving for the IV curve typically relies on numerical methods, which can become a bottleneck and redundant for similar input parameter values. To address this, a lookup table of dimensions $600 \times 2301 \times 119$ was generated. Each IV curve consists of 600 points, with irradiation values ranging from $0 W/m^2$ to $1150 W/m^2$ at intervals of 0.5 W/m^2, and temperature values ranging from -18°C to 41°C, also at 0.5°C intervals. This lookup table provides a 600-point IV curve array with current values for a predetermined voltage range for the irradiation and temperature values closest to the input, serving as an approximation to expedite the process.

Although this approach significantly reduced the run time on local hardware, it proved less effective on the remote cluster. The retrieval of data points took longer than the actual execution of the numerical methods on the cluster, leading to its exclusion from the main simulations. However, with modifications, this method holds potential for optimising the process for specific solar modules on different hardware configurations. The error in the annual energy calculation using this lookup table was found to be only -0.06%, primarily due to rounding down the input parameters. There remains scope to further reduce this error, though it was not explored in this study.

3.5.5. Utilisation of Remote Computer Cluster for MATLAB Simulations

To ensure efficient and expedited execution of the MATLAB code for the simulations, a remote computer cluster with high-performance specifications was utilized. The cluster is equipped with an Intel(R) Xeon(R) Gold 6326 CPU running at 2.90GHz. This CPU configuration includes 2 sockets, each hosting 32 cores, which collectively provide a total of 64 logical processors. Additionally, the system is endowed with 128GB of RAM.

The deployment of this high-performance computing environment was pivotal in managing and expediting the complex calculations inherent in the simulations. The extensive computational requirements are addressed through the implementation of parallel processing techniques, specifically using the `parfor` loops available in MATLAB. The `parfor` loops enable parallel iteration over the simulations of each floater throughout the year, effectively distributing the computational load across multiple cores. This approach minimises overhead and optimises processing time, with each iteration of the loop taking between 1 to 3 minutes to execute. By leveraging the multiple cores of the CPU, the parallel processing capability significantly reduces the overall execution time of the code.

Moreover, the ample RAM capacity of 128GB provides a substantial advantage when handling large matrices, which are common in these simulations. The increased RAM allows for the accommodation of larger datasets and more extensive calculations without running into memory limitations. This is particularly beneficial for the tilt model simulations, where multiple data points are considered within ten-minute intervals to achieve a more precise and detailed analysis. The large memory space ensures that these sizeable matrices can be efficiently managed and processed, enhancing the accuracy and reliability of the simulation results.

However, it is important to note that utilising all available cores does not necessarily translate to the fastest execution times. Due to the phenomenon of diminishing returns, there is an optimal number of cores that maximises efficiency without incurring unnecessary overhead. Through empirical testing, it was determined that employing approximately 50 logical processors strikes the best balance between performance and resource utilisation. This configuration provides the fastest execution times for the MATLAB code while avoiding the diminishing returns that can occur when attempting to utilise all available cores.

In summary, the combination of high CPU core count, substantial RAM, and strategic use of `parfor` loops has enabled significant improvements in the execution speed and efficiency of the MATLAB simulations. The remote computer cluster's capabilities have been instrumental in facilitating the complex and resource-intensive computations required for the simulations, ultimately contributing to the robustness and accuracy of the simulation outcomes.

3.5.6. Utilisation of ChatGPT for Modelling and Documentation

In the course of developing the algorithm and pseudo code for the shading model in this thesis, the entire process was initiated and conceptualised independently. The algorithm was meticulously broken down into smaller, manageable functions. To aid in the development of these functions, ChatGPT was employed as a valuable tool to assist in writing the initial code structure.

Given the mathematical nature and complexity of the functions required for the shading model, significant edits and modifications were necessary to ensure their correctness and functionality. While ChatGPT provided a robust foundation and overall structure for these coding blocks, careful refinement was essential to address the intricate mathematical computations involved. Despite these challenges, the assistance from ChatGPT greatly facilitated the construction of the shading model from scratch, streamlining the development process.

Furthermore, ChatGPT has been instrumental in enhancing the clarity and coherence of the language used in this report. By leveraging its capabilities, certain sections of the report were polished and refined to improve readability and ensure that the technical content is communicated effectively.

The use of ChatGPT has been a complementary tool in both the development of the shading model and the documentation of this thesis. Its contributions have ranged from providing structural support in coding to refining the language in the written report, thereby supporting the overall objectives of this research.

4

Results and Analysis

In this chapter, the results obtained from various simulations conducted throughout this study are presented and analysed. The chapter is structured into five sections, each focusing on different aspects of the results and their implications. First, the outcomes of the tilt model are examined, providing a detailed analysis of the implications and significance of the results. Next, different irradiance and frequency maps surrounding the wind turbine are presented. These maps illustrate how shading influences the irradiance distribution and how wind direction impacts the frequency of shading on the nodes. In the third section, the main simulation results are showcased, highlighting the energy and irradiation grid maps for a floater grid around a wind turbine. This section provides insights into the energy yield of the floating PV system in the presence of wind turbines. The fourth section focuses on the daily and annual power curves, exploring how the percentage loss of energy varies over the course of a year. This analysis highlights the temporal aspects of energy production and identifies periods of significant energy loss for a particular set of floaters. Finally, the last section discusses the constraint map used for analysis of the placement of a PV cluster within a specific wind farm configuration. This section emphasises the importance of strategic placement to maximise energy yield and minimise shading losses in a potential real-life scenario.

4.1. Tilt Model Analysis

In this section, the analysis of the tilt model is explored, which is a crucial component in understanding the performance of floating PV systems under varying sea conditions. The inputs used for the tilt model are first discussed. Next, the pitch and roll values obtained for the floater over the course of a year are analysed. Following this, the power intermittency experienced during three different days with varying wind speed conditions is explored. Finally, an annual analysis of how tilt affects energy yield is conducted.

4.1.1. Input parameters

The wind speed and wind directions, obtained from KNMI with a resolution of 10 minutes, have been modified using linear interpolation to achieve a time resolution of 1 minute. This adjustment allows for a more granular analysis of the wind conditions affecting the floating PV system. The PV modules placed on the floater are flat, meaning their tilt angle will mirror that of the floater itself.

The tilt of the floater has been computed for every second. While the actual wave period is much longer, typically around 5-6 seconds, this high-resolution computation is necessary because the model employed is statistical. Therefore, it requires more data points within the time intervals to accurately represent the overall characteristics of the tilt. The objective of this model is not to simulate real-time tilt accurately but to provide an overview of how the floater responds to waves and to better understand the power intermittency caused by wave action.

4.1.2. Pitch and Roll Values from the Tilt Model

The tilt model provided a comprehensive set of pitch and roll values for the floater. The histograms in figures 4.1 and 4.2 illustrate the distribution of these values, with the y-axis presented on a logarithmic scale. It is observed that some values appear to be extreme. These can be justified by acknowledging that the assumptions underpinning the model do not hold in all cases. To achieve a simplified model that could be effectively implemented in MATLAB, numerous assumptions were necessary. One of the most significant assumptions was regarding the interaction between the waves and the floater. The model presumes that the waves remain unaltered by the presence of the floater, which is an unrealistic scenario and likely contributes to the occurrence of such large values.

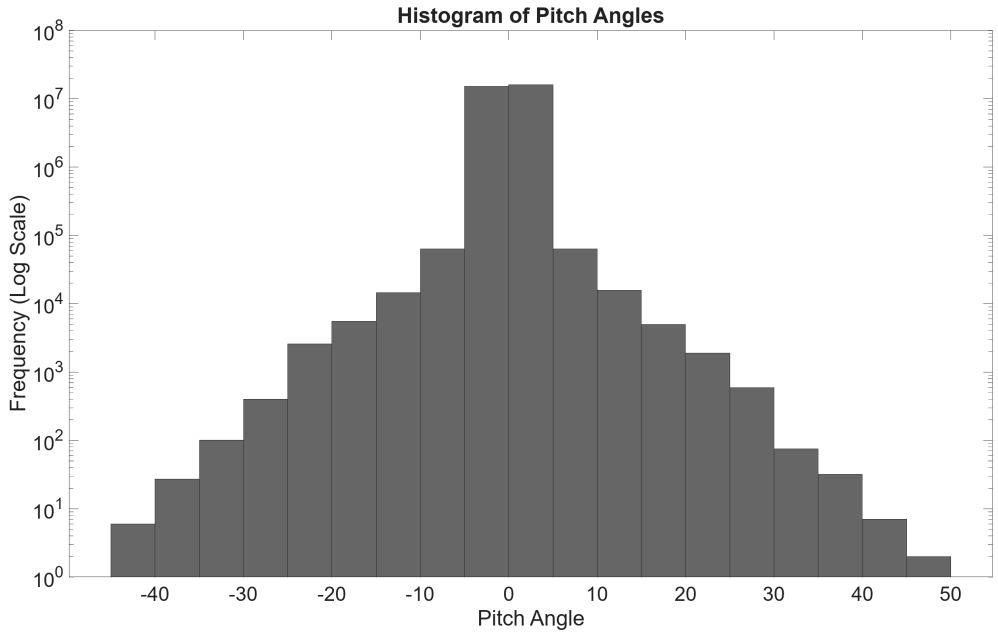

Figure 4.1: Histogram of Pitch Values

The distribution of roll and pitch values is influenced by the frequency of wind speeds predominantly coming from the west, as evidenced by the wind rose plot in figure 4.3. Consequently, there are more extreme pitch values than roll values. It is crucial to highlight that the dataset comprises 31 million data points, with an angle computed for each second of the year. However, it is important to note that the frequency of these extreme values is negligible when compared to the total number of data points, with the majority of values falling between 0 and 5 degrees.

4.1.3. Power Intermittency Analysis

This section explores the power intermittency analysis, focusing on three distinct days categorised as rough, moderate, and calm, based on their average wind speeds. The windrose plots for these three days are presented in figure 4.4, illustrating the distribution of wind directions and speeds.

The purpose of this analysis is to understand how variations in wind speeds affect the tilt of the floater and, consequently, the plane of array irradiance.

On the calm day, the irradiance profile appears typical without any significant variations, as shown in figure 4.5 . This day serves as a baseline for comparison with the other two days.

Moving on to the moderate day whose irradiation curve is shown in figure 4.6, the analysis reveals noticeable increases in power intermittency. This is evident in the irradiance plot for that day, where

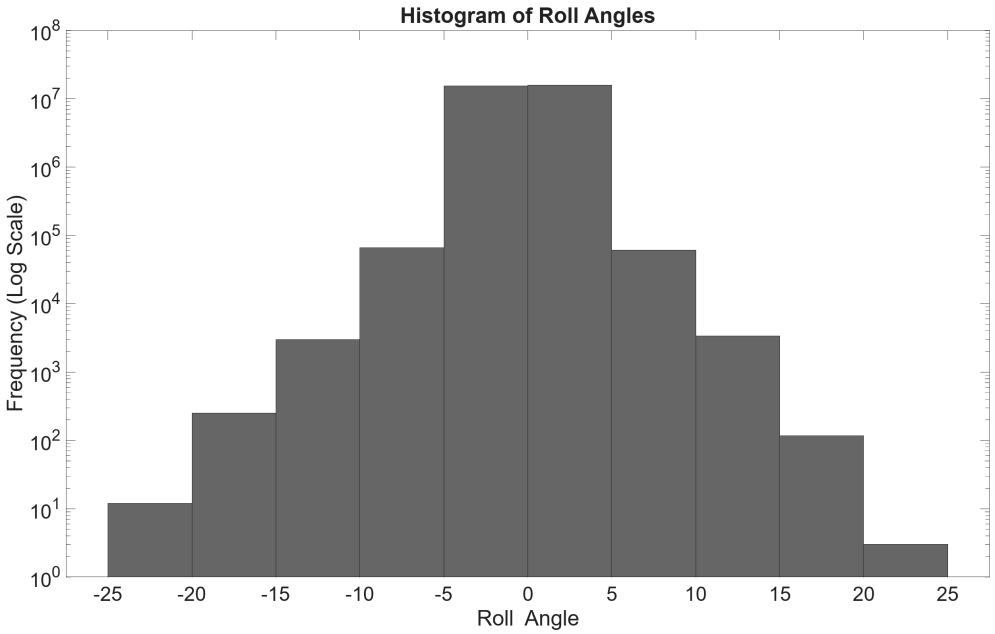

Figure 4.2: Histogram of Roll Values

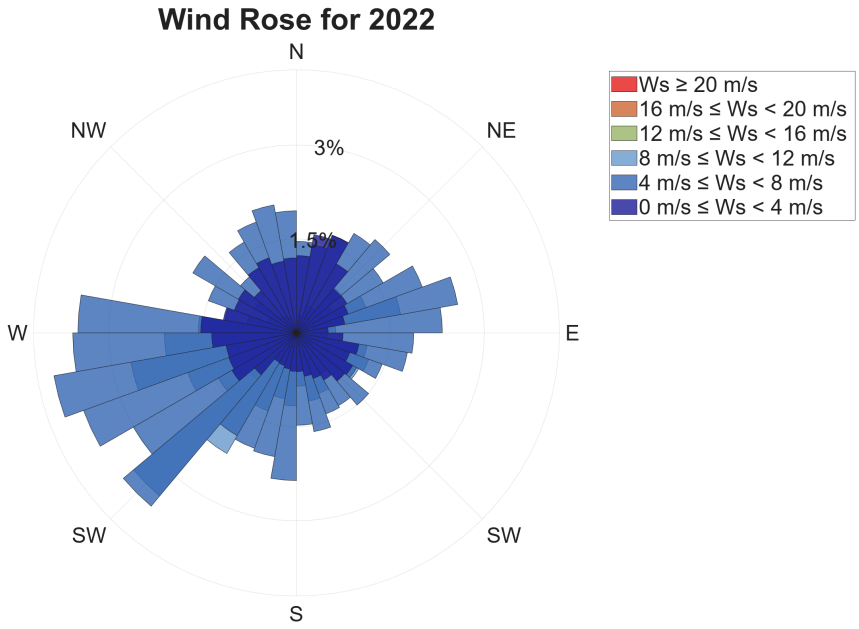

Figure 4.3: Wind Rose for the Year 2022

fluctuations are clearly visible, indicating greater variability in the power output.

Lastly, the rough day shown in figure 4.7 is characterised by extremely high intermittency, as depicted in its irradiance plot. It is crucial to note that some values observed on this day are extreme and may be highly exaggerated due to the assumptions and the model's stochastic nature.

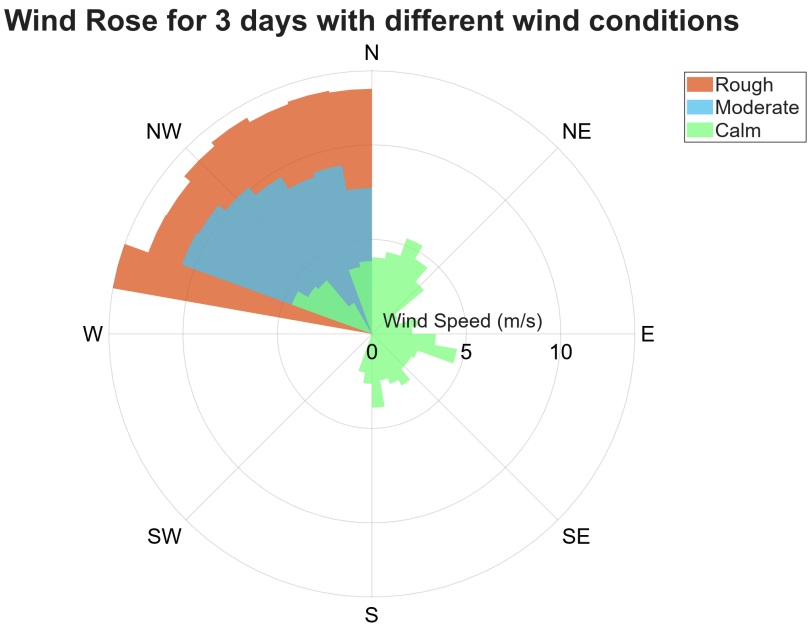

Figure 4.4: Windrose Plots for Rough, Moderate, and Calm Days

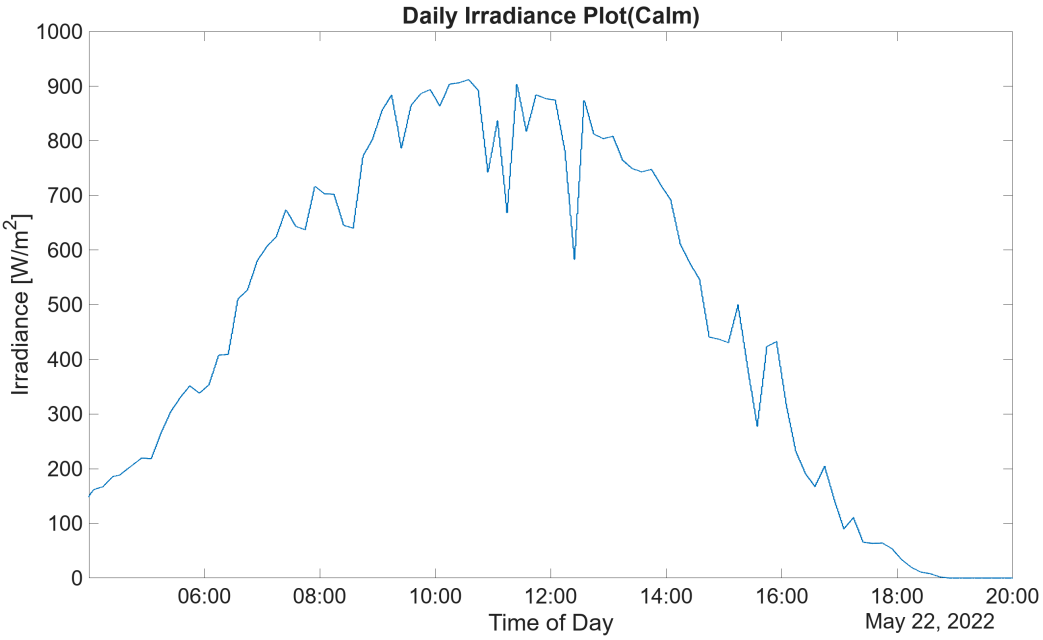

Figure 4.5: Irradiance Plot for the Calm Day

4.1.4. Annual Energy Analysis

Now, the annual energy analysis is discussed, focusing on the impact of tilt on the energy production of a floater. The tilt can result in the panels facing towards or away from the sun, causing an increase or decrease in the generated power at a particular time instance. To understand the overall effect of tilt on the annual energy yield, a comprehensive analysis was conducted. Given that the tilt model relies on statistical methods, a single simulation does not provide a complete picture. Therefore, 100 simulations were carried out, and the annual energy for each instance was calculated, as illustrated in the figure 4.8.

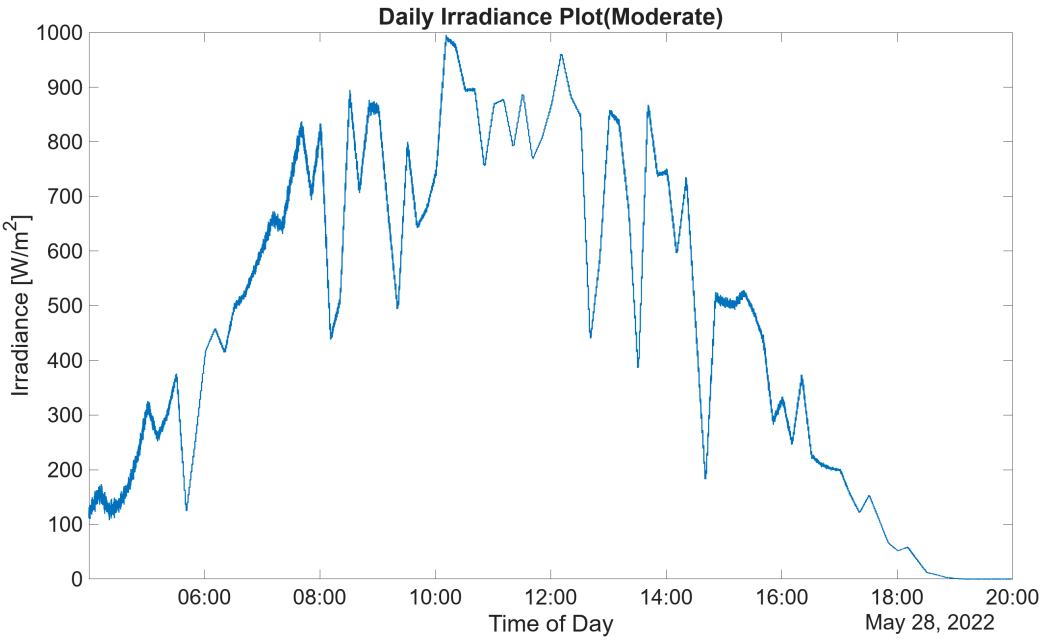

Figure 4.6: Irradiance Plot for the Moderate Day

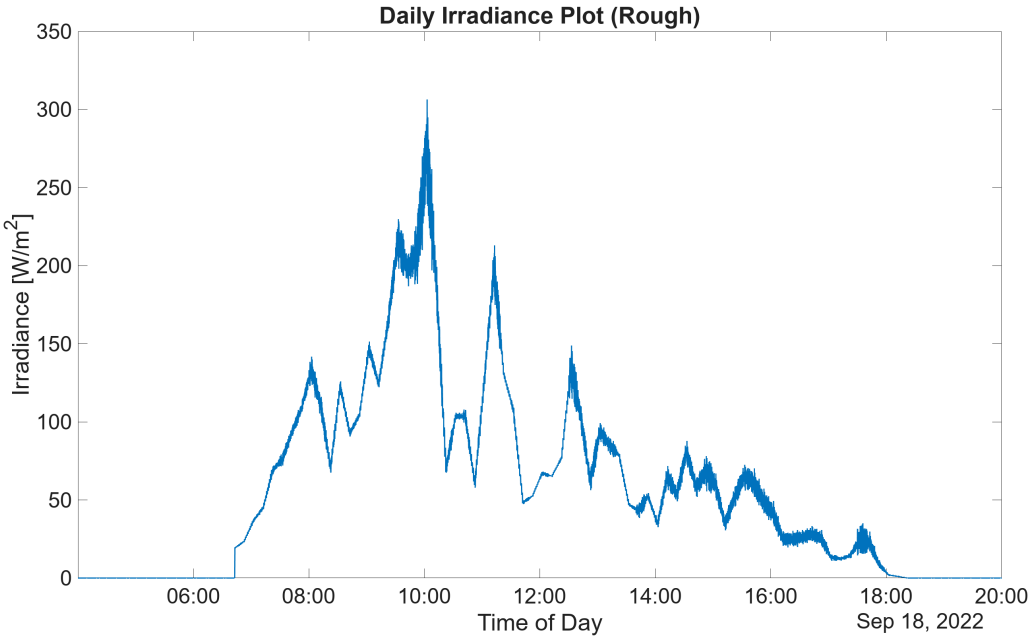

Figure 4.7: Irradiance Plot for the Rough Day

The average annual energy was determined from these simulations. It was observed that in some instances, the annual energy slightly decreases, while in others, it slightly increases. For a scenario without tilt, the annual energy of a floater was found to be 259.40 MWh. In comparison, the average energy for the 100 tilt simulations was 259.37 MWh. This indicates that, for this specific case where the panels are placed flat on the floater, the effect of tilt does not significantly impact the annual energy production.

However, it is important to note that this conclusion may not hold if the panels are placed at an angle

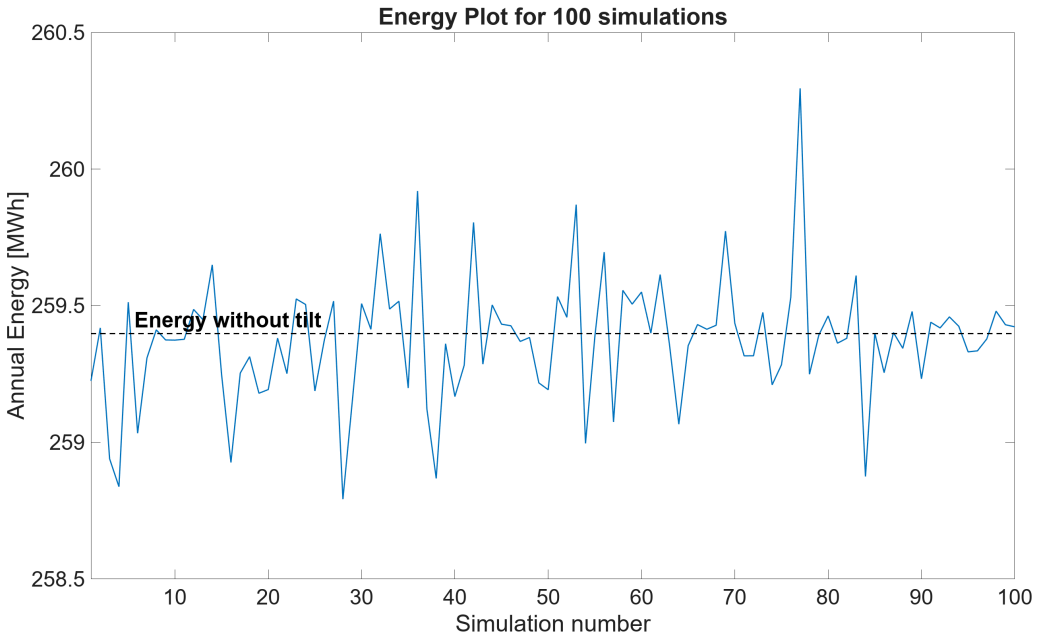

Figure 4.8: Annual Energy Yield for 100 Simulations of the Tilt Model

on the floater. Such a scenario would require separate simulations to accurately understand how tilt affects energy production in that configuration.

4.2. Irradiance and Frequency Node Maps

In this section, the irradiance and frequency node maps derived from various simulations are discussed to illustrate the impact of wind turbine shading on the irradiance distribution in the surrounding area. The analysis includes both annual and daily timescales to provide a comprehensive understanding of the shading effects. The irradiance node maps demonstrate how the presence of a wind turbine influences the irradiance levels in it's surrounding, highlighting areas that experience reduced sunlight due to the turbine's shadow. These maps are crucial for identifying regions with significant shading and understanding the overall impact on energy production.

Additionally, the frequency node maps show the number of times a node is shaded over different durations. This includes both annual and daily analyses, providing insights into the consistency and variability of shading over time. By examining these maps, the shading patterns can be better understood with the wind direction being a parameter. The combination of irradiance and frequency node maps offers a detailed view of the spatial and temporal variations in shading, which is essential to understand how wind direction affects the characteristics of the shade that occurs surrounding a wind turbine.

4.2.1. Annual Irradiance Map

The integration of floating photovoltaic (FPV) systems within offshore wind farms presents unique challenges, particularly regarding the shading effects caused by wind turbines on surrounding FPV modules. The variability in shading can lead to non-uniform irradiance across the photovoltaic modules, affecting their efficiency and overall energy output. The necessity of this analysis arises from the need to maximise energy yield in hybrid wind-solar farms. Accurate mapping of irradiance helps in identifying high irradiance regions for placing FPV modules, minimising shading losses, and enhancing the overall efficiency of the energy farm. It also assists in predicting and mitigating the adverse effects of shading, thereby improving the design and layout strategies for future implementations.

The methodology employed involves simulating the annual irradiance received by each node in the vicinity of a wind turbine. The simulation incorporates various factors, including the geometric configuration of the wind turbine, the position of the sun throughout the year, the wind directions and wind speeds. The simulation is configured with a grid map representing the area around a wind turbine. Each node in this grid represents a point on the surface where the irradiance is measured. The irradiance is computed every 10 minutes.

The shading model is used to determine the shading effect of the wind turbine on each node. The irradiance values are aggregated over the entire year to obtain the annual irradiance map. This aggregation helps in understanding the long-term effects of shading and provides a comprehensive view of the energy potential of each node. The resulting annual irradiance map, as shown in figure 4.9, illustrates the distribution of irradiance around the wind turbine. The colour scale represents the total energy received by each node over the year, with higher values indicating greater irradiance.

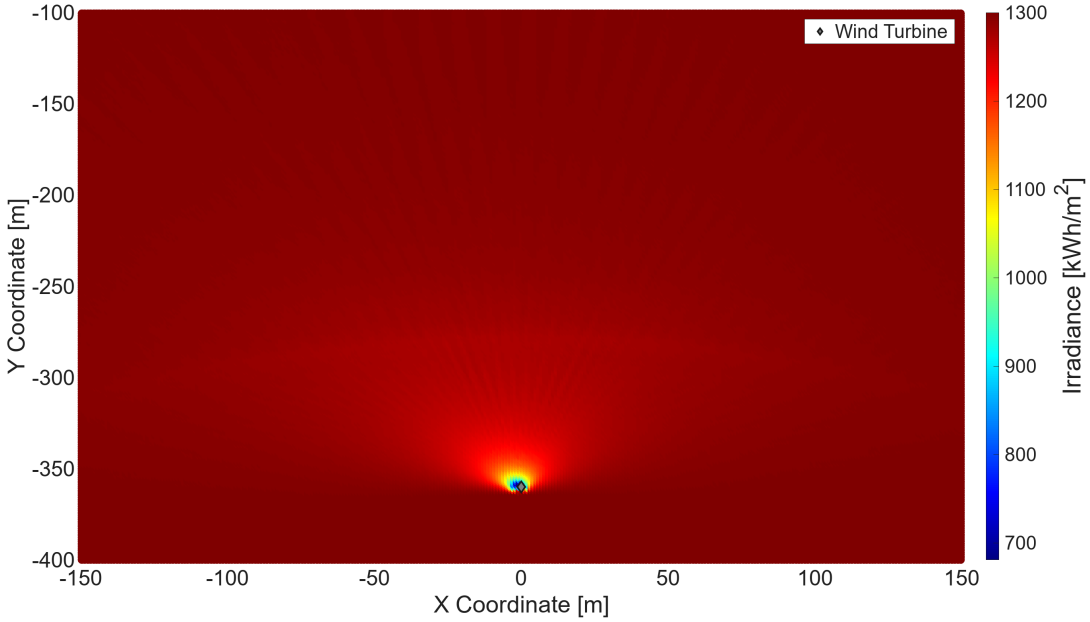

Figure 4.9: Annual Irradiance Per Node

The map clearly shows a region of reduced irradiance north of the wind turbine, where the shadow of the turbine blades frequently falls. This area exhibits lower energy values compared to the regions further away from the turbine. The irradiance distribution follows a pattern that reflects the the position of the sun throughout the year. Nodes located to the south of the turbine generally receive higher irradiance, suggesting these areas are less affected by shading due to the wind farm being in the northern hemisphere. The insights gained from this map can be used to better place the FPV modules. By avoiding areas with significant shading and placing modules in high irradiance zones, the overall energy yield of the FPV system can be maximised. The results highlight the importance of considering shading effects in the design and layout of hybrid energy farms. By integrating the shading model into the design process, it is possible to enhance the efficiency of these systems.

4.2.2. Annual Frequency Shading Node Maps

The annual shading frequency node maps illustrate the frequency at which each node is shaded surrounding a wind turbine, represented using a colormap with a log scale. This log scale provides a better distribution of colours, enhancing the visual clarity of the plots. These maps are generated on an annual scale with a time resolution of one minute to capture the temporal dynamics of shading accurately. To achieve these results, nodes within the elliptical disc formed by the wind turbine blades at each

time step are considered. This is different from the static shading model where only one blade azimuth angle was considered for the annual energy calculations. This approach helps in understanding how the movement of the blades affects the shading frequency map. The yaw angle, which aligns the axis of rotation of the wind turbine blades with the wind direction, is also accounted for in these simulations.

In figure 4.10, the wind direction is taken to be constant at 0°, while in figure 4.11, it is based on the interpolated input data with a time resolution of one minute. The comparison between these two cases reveals differences in the boundary of the most frequently shaded nodes. This is due to the fact that the most dominant wind direction for this year is west ward and so the disk formed by the shadow due to the blades have a higher probability of being bigger during sunrise and sunset which is why the boundary of the most frequently shaded nodes in red are elongated more towards the east and west of the wind turbine as compared to the case with a constant wind direction. In the case with constant wind direction, as the plane of the blades is aligned with the x-axis, during sunrise and sunset the disc formed by the blades would be very narrow, almost following the shape of the blade thus leading to the pattern that is observed. This same explanation can be used to describe why this red area is further up north in the case with constant wind direction. This information helps in understanding how the wind direction influences the shading of areas surrounding a wind turbine.

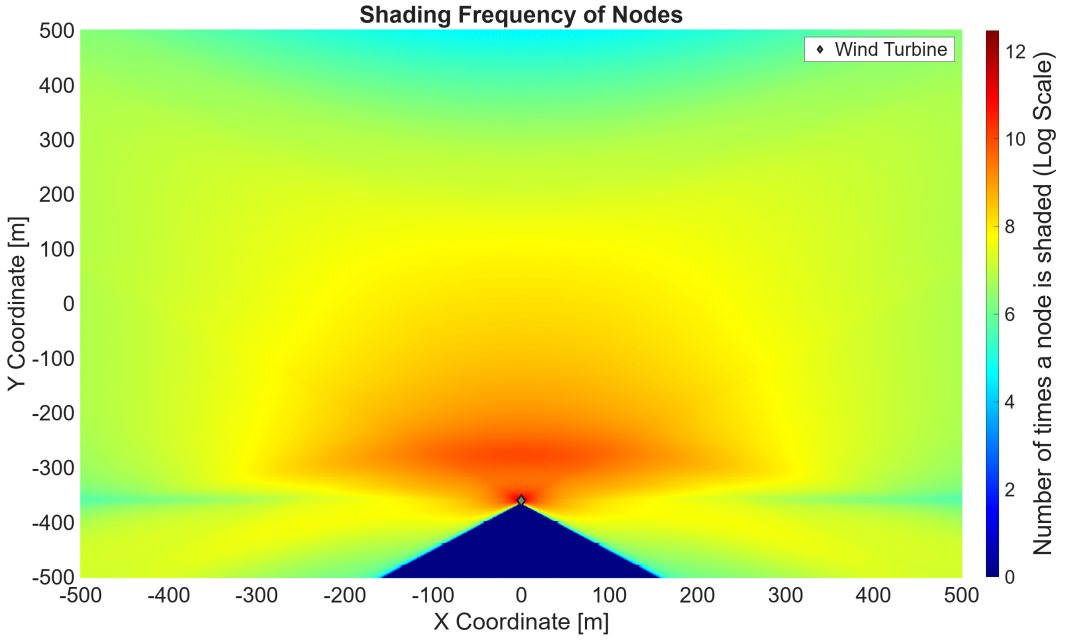

Figure 4.10: Annual Shading Frequency with Constant Wind Direction at 0 degrees (Towards South)

The assumption of uniform wind direction based on input data in these simulations provides a general understanding of shading patterns. However, in reality, wind directions can be heterogeneous in a wind farm due to the influence of multiple wind turbines. This heterogeneity can lead to variations in shading patterns among different turbines. The model presented here offers a framework that can be adapted if detailed wind direction data is available, allowing for more accurate predictions of shading effects. These maps can inform better placement strategies for floating photovoltaic modules to minimise shading losses and maximise energy yield and can help identify areas most susceptible to dynamic shading effects due to the blades of the wind turbine.

4.2.3. Daily Node Shading Frequency Map

The methodology used to derive the daily node shading map is identical to that described in the previous section. However, in this case, the duration of the simulation is limited to a single day. This approach allows for a detailed examination of shading patterns over shorter time frames. Figures 4.12 and 4.13

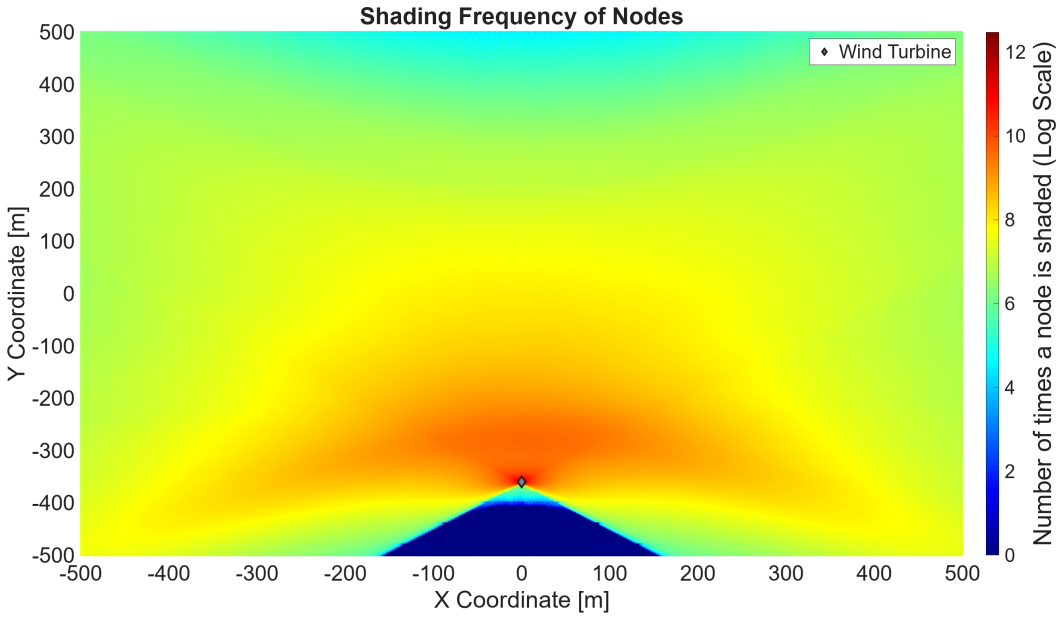

Figure 4.11: Annual Shading Frequency with Variable Wind Direction Based on Input Timeseries Data

illustrate the node frequency maps for January 1, considering two different wind direction scenarios. In the first scenario, the wind direction is held constant at 0 degrees i.e. from North to South. As shown in figure 4.12, the nodes that are most frequently shaded are located to the north of the wind turbine. This observation aligns with the expectation that the shadow cast by the turbine blades forms the largest disc when the sun is positioned to the south of the wind turbine.

In the second scenario, the wind direction is held constant at 90 degrees i.e. from East to West. As depicted in figure 4.13, the nodes to the north of the wind turbine are among the least frequently shaded. This outcome is due to the fact that the axis of the plane of the turbine blades is orthogonal to the south. Consequently, when the sun is to the south, the shadow disc formed by the blades is smallest, leading to less frequent shading in the northern region.

By examining these daily shading maps, it is possible to gain a deeper understanding of the impact of wind direction on the shading patterns around a wind turbine over shorter periods. In reality, the wind direction is not constant and varies throughout the day. To illustrate this, the shading frequency map for May 26th, a day when the wind directions are relatively consistent, has been analysed. On this particular day, the predominant wind direction is north-east. The frequency shading map for May 26th, shown in figure 4.14, reveals an asymmetry where the nodes to the east of the wind turbine are shaded more frequently than those on the west side. This asymmetry is attributed to the dominant yaw angle, which is influenced by the prevailing wind direction.

Another notable observation is the difference in the area surrounding the wind turbine that is shaded, compared to the January 1st plot. This discrepancy is due to the significant difference in solar angles, specifically the solar elevation and solar azimuth angles, between these two days. The solar angles greatly affect the extent and shape of the shaded region for any particular day.

Understanding that the wind direction, which determines the yaw angle of a wind turbine, can be predicted or known beforehand is crucial. By identifying regions that are susceptible to more dynamic shading or higher frequencies of shading, better power variability predictions and energy estimations can be made. This information is valuable for placement strategies of PV modules to minimise shading losses and enhance energy yield.

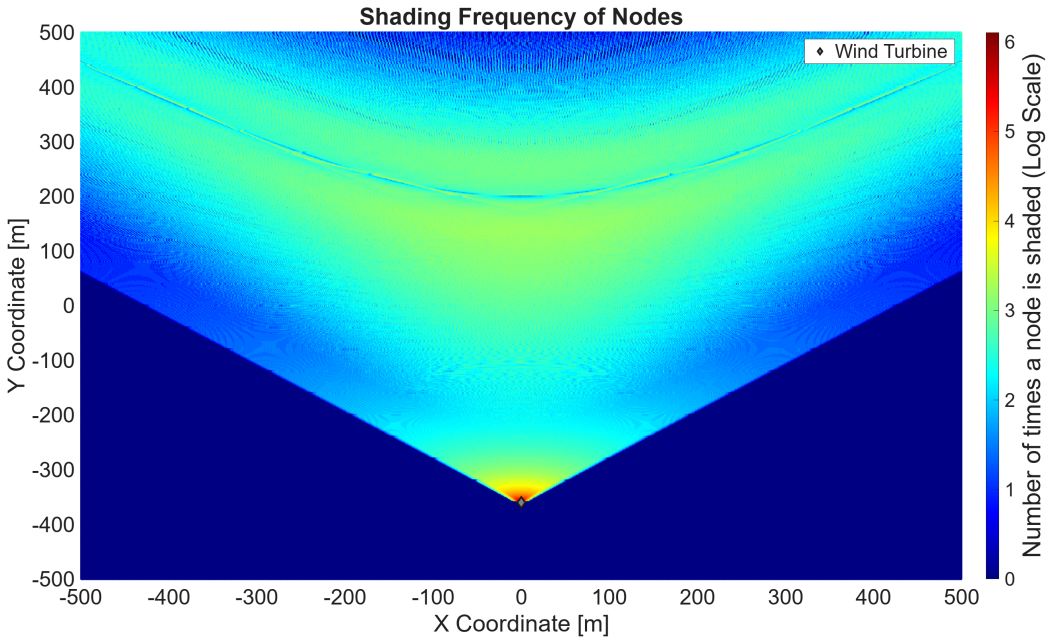

Figure 4.12: Daily Node Shading Map for January 1 with Wind Direction Constant at 0 Degrees (Towards South)

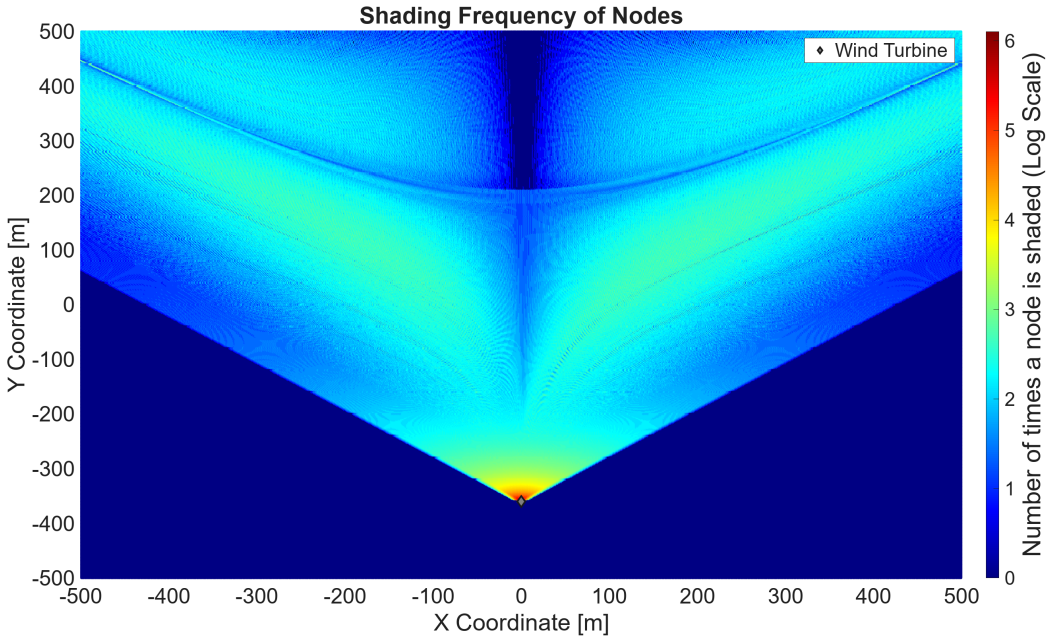

Figure 4.13: Daily Node Shading Map for January 1 with Wind Direction Constant at 90 Degrees (Towards West)

4.3. Floater Energy and Irradiance Grid Maps

In this section, the annual irradiance and energy grid maps derived from the simulation are presented. The setup for this simulation is described as follows: The time resolution is set to 10 minutes, and the simulation runs for an entire year. The wind turbine is strategically placed at coordinates [0, -360], surrounded by a grid of floaters. The centre of the grid map is fixed at [0, 0], but the size of the grid can be adjusted as needed.

The decision to place the wind turbine 360 meters south of the centre of the cluster is based on the

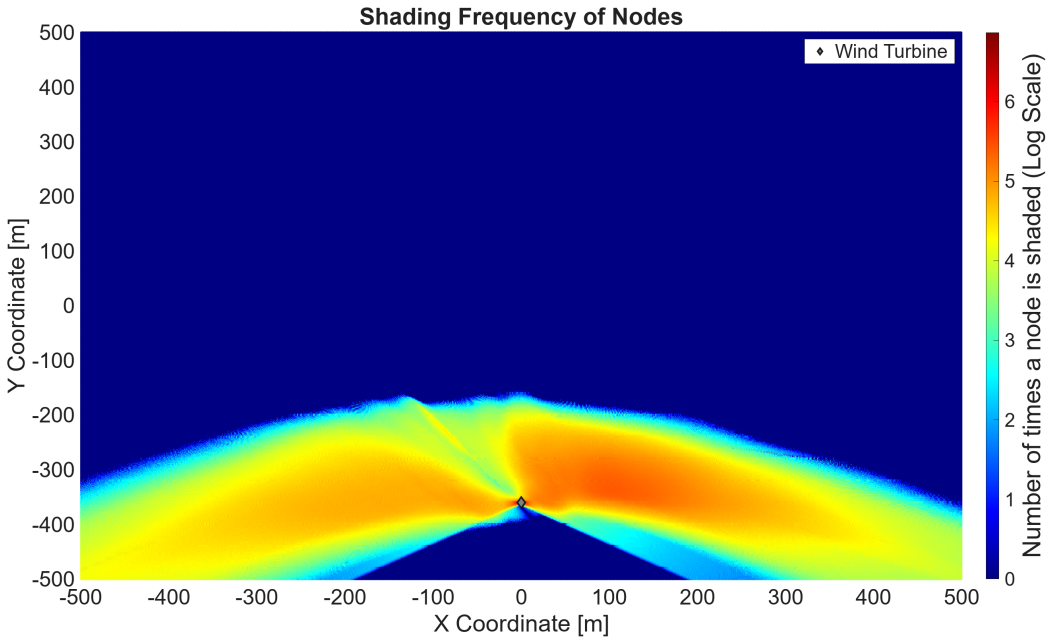

Figure 4.14: Daily Node Shading Map for May 26 with Predominant Wind Direction (towards North-East)

geographical consideration that the wind farm is located in the northern hemisphere. In this setup, significant shading effects south of the wind turbine are minimised. The shading to the south will primarily occur due to two factors. First, during the summer months, the sun rises and sets with a solar azimuth angle of less than 90 degrees and more than 270 degrees, respectively, which results in long shadows during these times. Second, shading can also occur directly south of the wind turbine due to the blades, which is possible due to the yawing motion of the turbine but it is not possible for this shade due to the blades to go out of the clearance area of the offshore wind turbine south of the wind turbine. The clearance area has been considered to be the area around the wind turbine that has a radius equal to the radius of the blade of the wind turbine.

To enhance the efficiency of the simulation, it is executed iteratively using parallel for loops for all the floaters. This approach significantly speeds up the execution time. The output values from this simulation are used to generate the figures presented in the following sections, representing the irradiance and energy data for each floater in the grid.

4.3.1. Irradiance Map Analysis

The annual irradiance map shown in figure 4.15 illustrates the distribution of irradiance across the floater grid surrounding the wind turbine. It is observed that there is a very negligible loss in the irradiance values for all floaters located south of the wind turbine on an annual scale. This negligible loss is expected due to the position of the wind turbine in relation to the sun's path. As anticipated, the irradiance losses are most significant for the floaters situated near the wind turbine. The floaters directly north of the wind turbine are the most affected by shading-induced irradiance losses. A distinct mushroom-shaped gradient can be seen, similar to the pattern observed in the most frequently shaded nodes in the annual node shading frequency map.

Furthermore, it is noticeable that the floaters located to the north-north-west (NNW) of the wind turbine experience more shading losses compared to those in the north-north-east (NNE). This discrepancy is due to the higher irradiation during the times when the floaters in the NNW are affected by static shading from the turbine tower, compared to the floaters in the NNE. This observation is corroborated by the cumulative irradiance data binned by solar azimuth angles, as shown in the figure 4.16.

The magnitude of the shading losses is predominantly dictated by the cumulative irradiance for the

those ranges of solar azimuth angle which cause shading on that respective floater, more so than the wind direction, which primarily affects the shape of the shadow. This conclusion holds true for the annual time scale and the larger spatial resolution of a floater. Also to be noted that changes in the spatial resolution do not significantly alter the observed characteristics, as corroborated by the irradiation map presented in the previous subsection. The maximum irradiance loss experienced by a reference floater in the simulation is 4.5%. In contrast, the maximum loss for a floater located outside the clearance area designated for wind turbines in this particular wind farm is significantly lower, at just 1.4%. This comparison highlights the impact of proximity to the wind turbine on irradiance losses and underscores the importance of strategic placement of floaters to minimise shading effects.

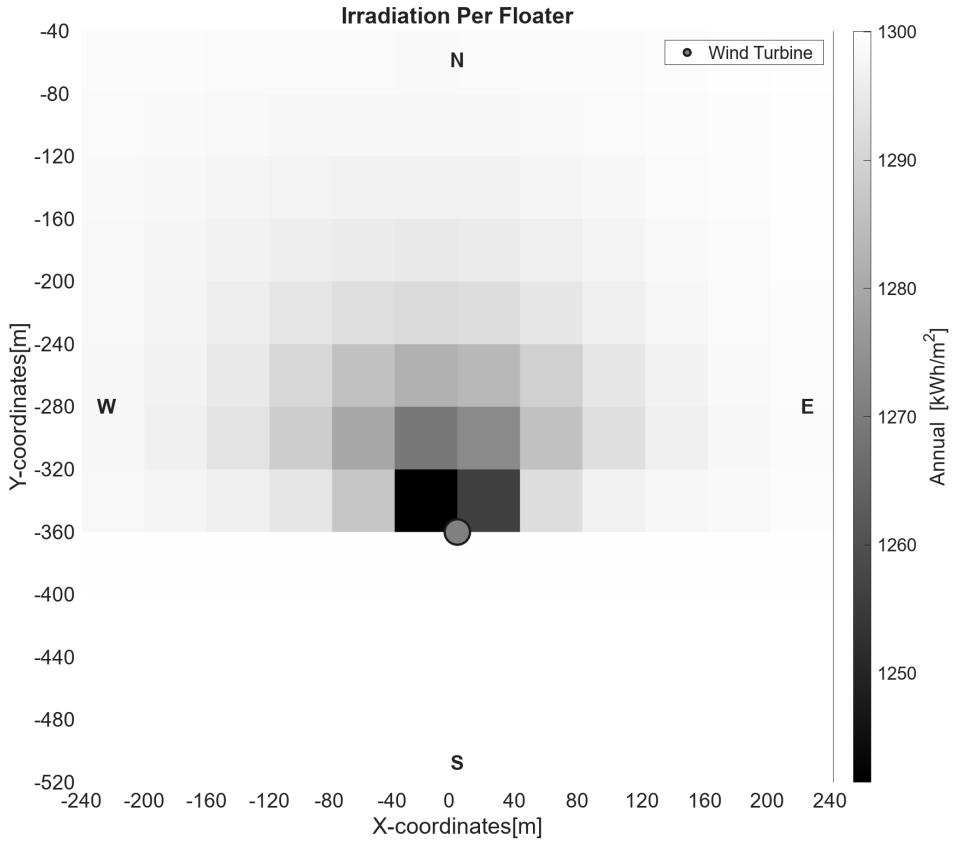

Figure 4.15: Annual Irradiance Floater Grid Map

4.3.2. Annual Energy Map Analysis

The energy grid map for the entire year exhibits a similar pattern to the annual irradiance grid map as shown in figure 4.17. However, it is observed that the energy loss for the floater experiencing the highest loss is 10.5% compared to a floater that does not experience shading losses. This higher percentage of energy loss compared to the maximum loss percentage for irradiance can be attributed to the nature of PV string operation.

If there is a 20% loss of irradiance distributed over some modules in a string connected in series, a mismatch is created in the power output of the modules within that string. The proportion of power lost is greater than the proportion of irradiance lost. This phenomenon occurs because the current in a PV string, where modules are connected in series, must remain the same. When finding the maximum power point for a string with uneven shading over the modules, this effect becomes pronounced. Although a similar phenomenon occurs for individual strings of solar cells within a solar module depending on how the shade spans across a module. This level of detail has not been modelled in the simulation models.

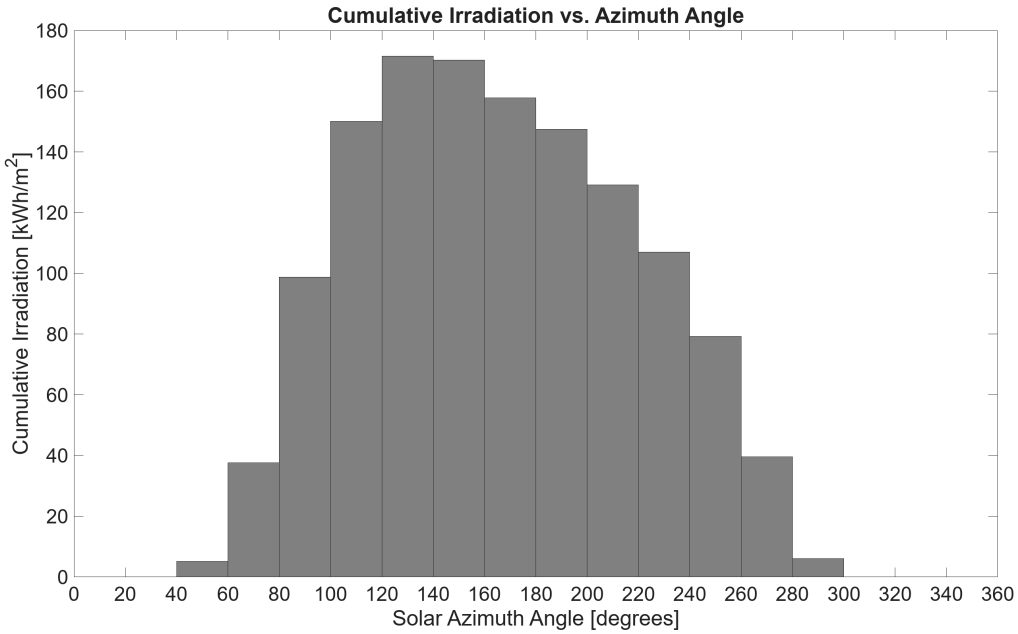

Figure 4.16: Cumulative Irradiance Data Binned by Solar Azimuth Angles

The maximum energy loss for a floater outside the clearance area, which is relevant for an offshore installation, is 2.9%. These losses are a reasonable approximation of the energy loss. However, it is important to note that the shading model used is a static shading model. In reality, these DC losses could be much higher due to the inverter's inability to track the maximum power point accurately under dynamic shading caused by the wind turbine blades. Consequently, these loss estimations provide a lower bound for predicting the loss percentage for these floaters.

4.3.3. Blade-Induced Energy Loss Map

The energy grid map in figure 4.18 which represents the difference between the energy map considering all shading elements and another energy map where the blades have not been simulated, specifically isolates the energy losses attributable to the blades alone. This map effectively highlights the floaters most susceptible to dynamic shading, excluding overlaps with the turbine tower or nacelle.

This analysis demonstrates which floaters are particularly affected by dynamic shading due to the blades. In reality, the blades will be moving based on the wind speed, which determines their rotation speed, thus dynamically altering the shading pattern. The energy loss values derived from this static model would be higher in a real scenario, influenced by the choice of inverter and its ability to track the maximum power point under dynamic conditions.

For large PV installations, this static model can be instrumental in decision-making processes. For instance, if two floater positions have similar parameters influencing potential losses but differ in their susceptibility to dynamic shading, the floater with less dynamic shading would be preferable. This decision, based on minimising dynamic shading losses, is crucial for increasing energy yield. However, this approach remains an idealised method of analysis. In real-world scenarios, many additional factors and complexities need to be considered to accurately predict and mitigate energy losses due to dynamic shading.

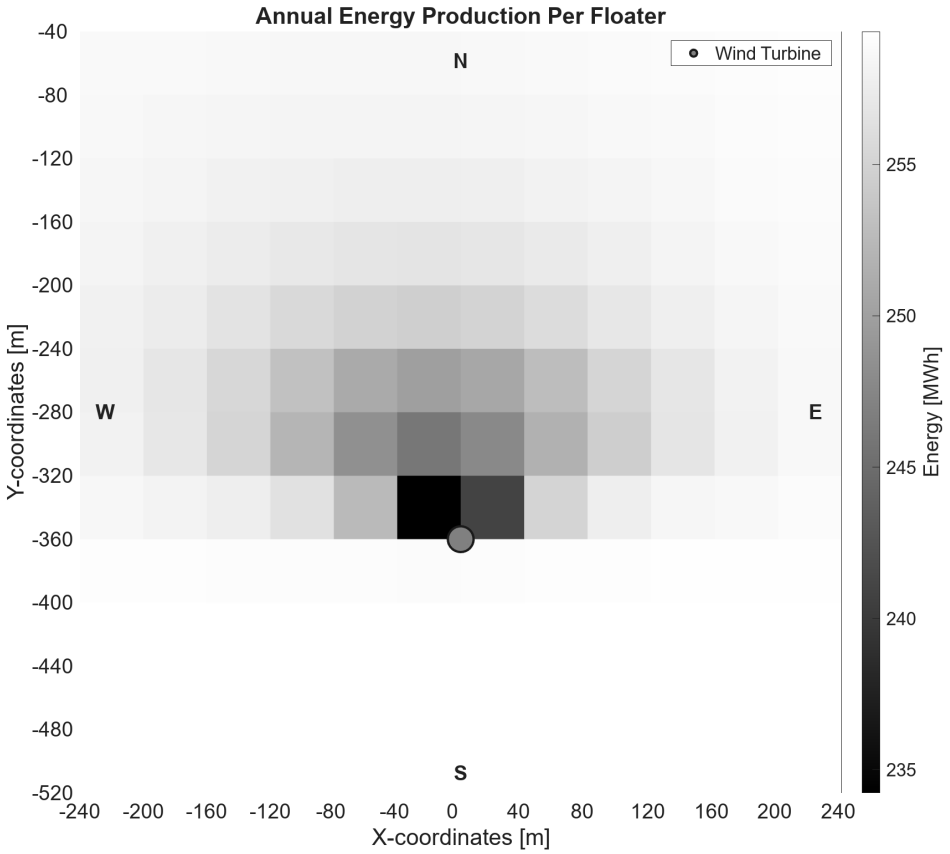

Figure 4.17: Annual Energy Floater Grid Map

4.4. Daily Power Curves and Energy Loss Analysis

In this section, for a floater that experiences shade and one that does not, first, an analysis of the daily power curves for three different days categorised based on wind speeds will be presented. Following this, the annual energy variation will be examined. Finally, the variation in the percentage of energy loss for a floater throughout the year will be discussed.

4.4.1. Daily Power Curves for 3 Cases

In this section, the daily power curves for three different days—calm, moderate, and rough—are analysed. These days were previously discussed in the results for the tilt model section. The reference floater considered for shading is located north of the wind turbine, just outside the clearance area.

Figure 4.19 compares the power curves for a calm day between two floaters: one that experiences shading losses and another that does not. During the shading period for the shaded floater, it is observed that the initial power loss is minimal but increases later. This increase is due to the blades initially causing shading on the floater, followed by additional shading from the turbine tower and nacelle, resulting in more significant power losses. This pattern repeats towards the end of the shading period. On a calm day, there are minimal power fluctuations on a smaller time scale.

In the next figure, the power curve for the moderate day is presented in figure 4.20. There are more variations in power due to changes in tilt, but the same power loss pattern is observed during shading as on a calm day. This highlights how moderate wind conditions affect the power output intermittently.

Figure 4.21 shows the power curve for the rough day, where the variations in power are more pronounced than on the moderate day. These variations in power follow the fluctuations in irradiance.

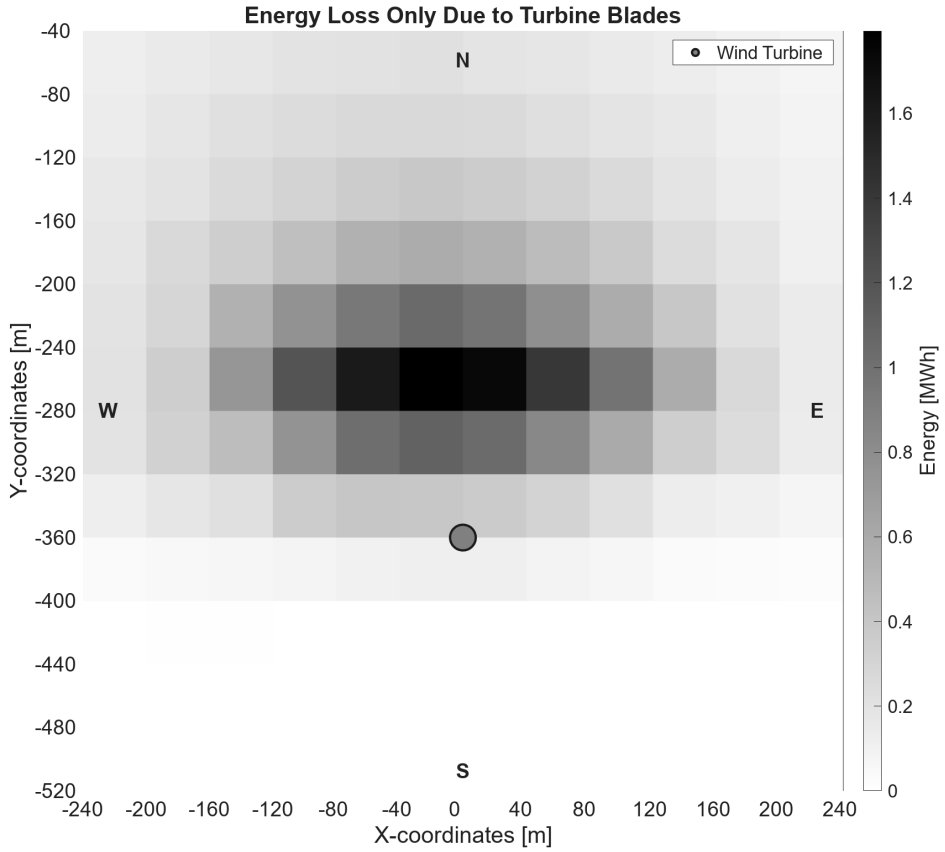

Figure 4.18: Blade-Induced Energy Loss Grid Map

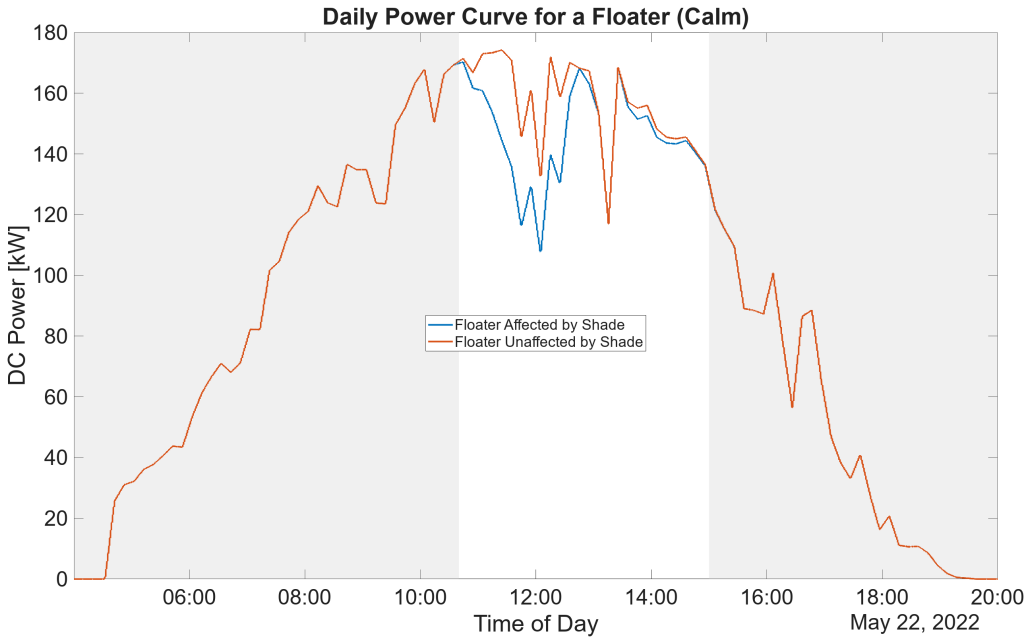

Figure 4.19: Power Curve Comparison for a Calm Day Between a Floater Affected by Shade and One Unaffected by Shade

The power loss observed is lesser because the irradiance values are generally lower, indicating a mostly cloudy day. Shading losses of diffuse horizontal irradiance (DHI) are negligible and hence not

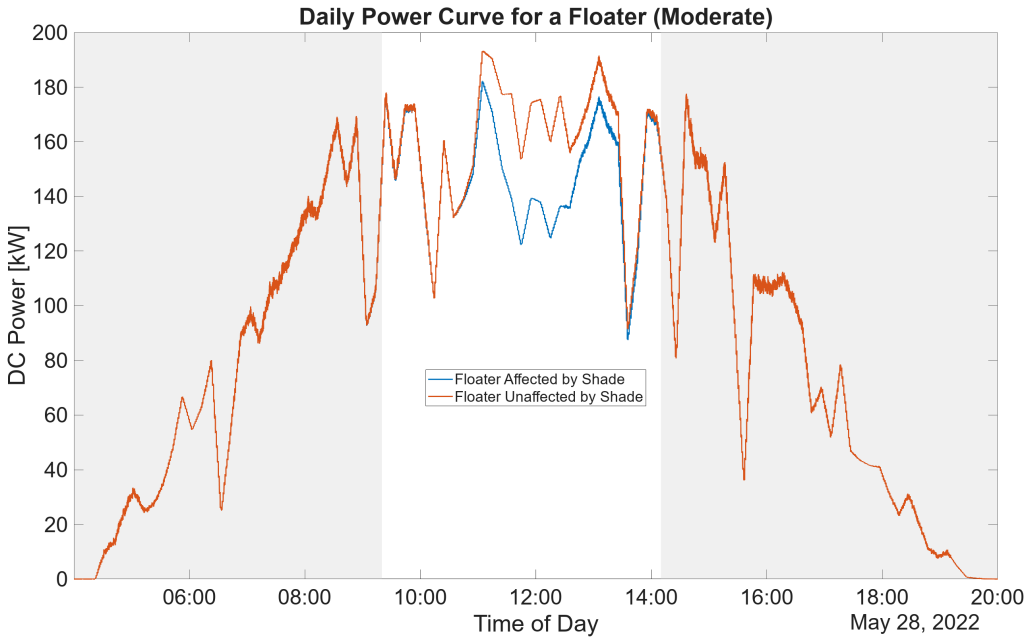

Figure 4.20: Power Curve Comparison for a Moderate Day Between a Floater Affected by Shade and One Unaffected by Shade

considered. The period in a day when shading is expected for a particular floater varies based on its position relative to the wind turbine and is predictable, corresponding to the solar azimuth angles for that time.

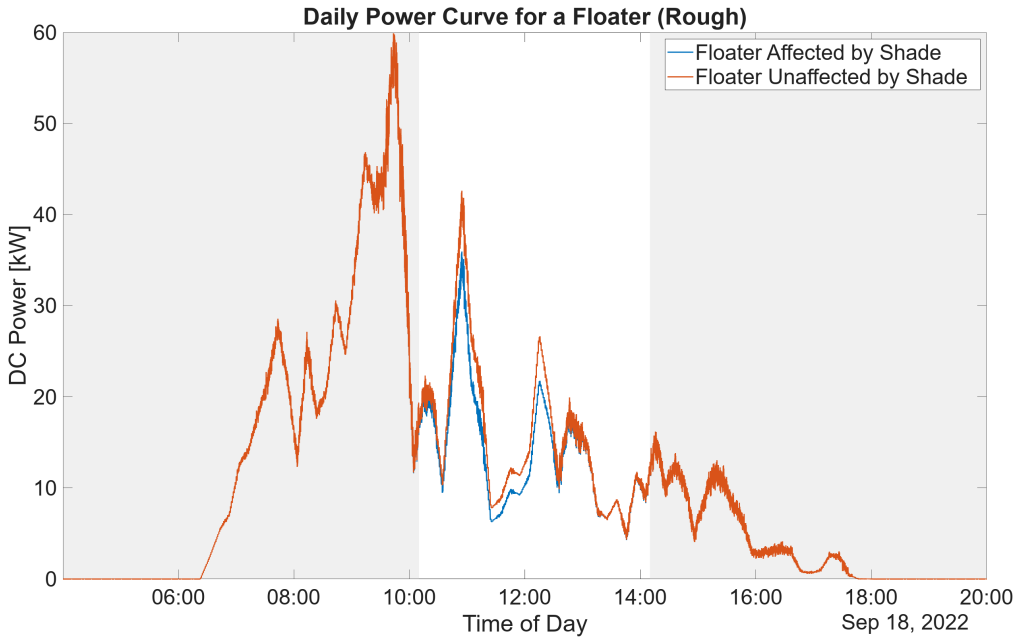

Figure 4.21: Power Curve Comparison for a Rough Day Between a Floater Affected by Shade and One Unaffected by Shade

4.4.2. Annual Energy Curves

In the next subsection, the annual energy curves are discussed. The first figure 4.22 shows the energy produced with a time resolution of one day. The same two floaters are considered for these plots as before: one that does not experience shading and another located north of the wind turbine outside the clearance zone that does experience shading.

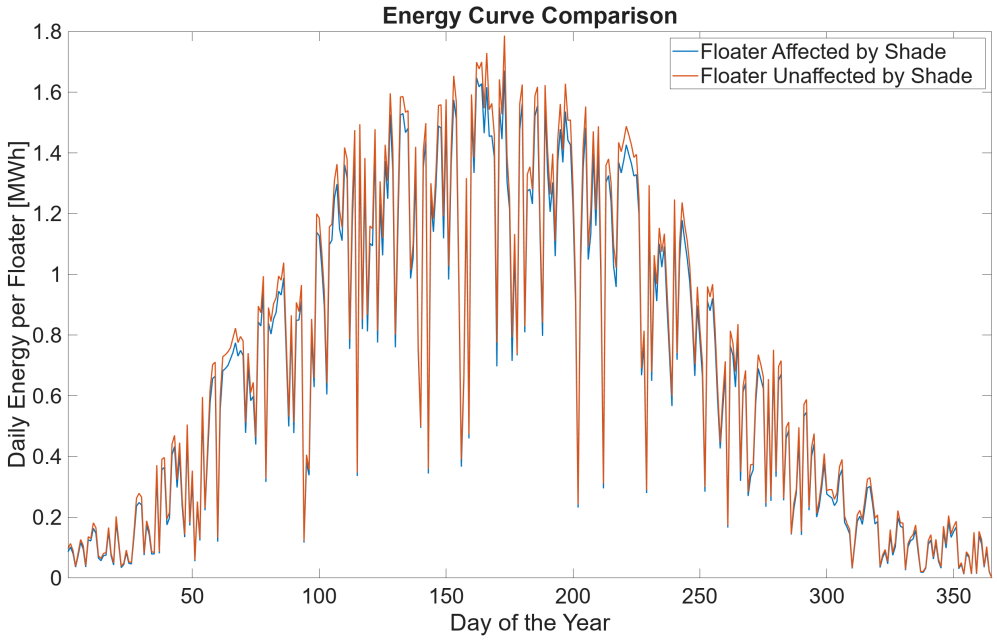

Figure 4.22: Daily Energy Production Comparison for a Floater North of the Wind Turbine Affected by Shade and a Floater Unaffected by Shade

From the graph, it can be observed that the magnitude of energy loss is lesser during the winter months and higher during the summer months. There are noticeable dips in 4.22 the energy produced on certain days, which can be attributed to cloudy weather leading to reduced overall irradiance. On these cloudy days, the power loss is minimal due to the lower levels of direct sunlight. The annual energy for the floater with no shading is 259.4 MWh, whereas for the floater experiencing shading, it is 247.46 MWh.

In figure 4.23, the weekly energy production is plotted on the X-axis. This plot makes it more evident that there is a greater loss of energy during the summer months compared to the winter months.

4.4.3. Energy Loss Variation

In this subsection, the variation in the percentage of energy lost due to shading on a floater is illustrated. Figure 4.24 shows the percentage loss of energy in a day for four floaters, compared to a floater that is not affected by shading. These floaters are located north of the wind turbine at increasing distances.

The first observed trend is that floaters closer to the wind turbine experience higher percentage losses in energy, which is expected from previous months. The second trend is that the percentage of energy lost due to shading is higher during the winter months and lower during the summer months. Although the percentage loss is lesser in the summer, the magnitude of power loss can be greater due to higher energy production during these months, as seen in the previous subsection.

This trend can be explained by two factors. First, the solar elevation angle is higher during the summer months, resulting in shorter shadows that do not reach the floaters. Second, the range of daylight hours is longer in the summer, increasing the range of azimuth angles. The loss experienced by a floater will

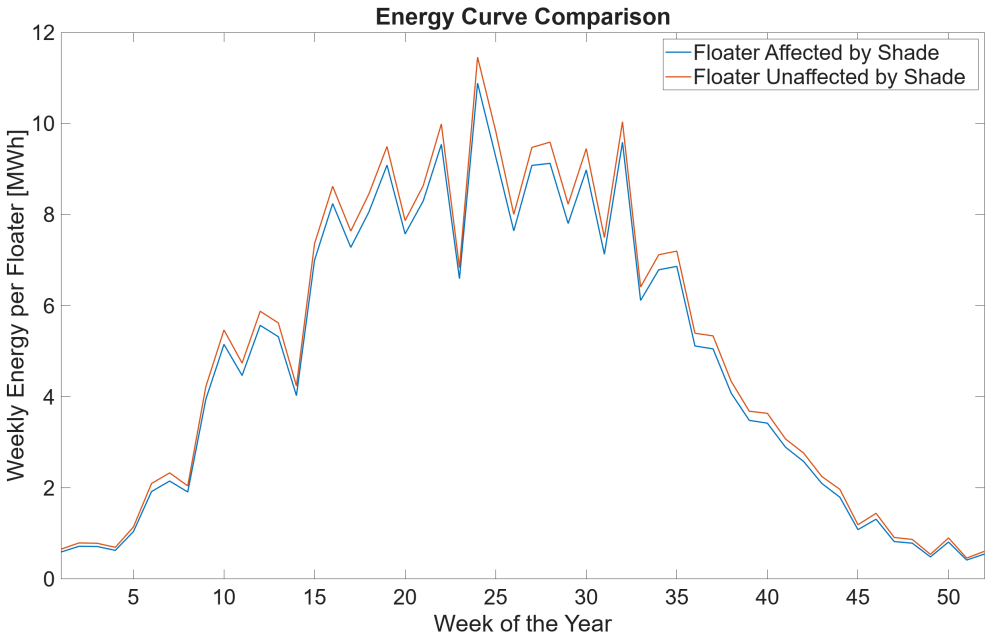

Figure 4.23: Weekly Energy Production Comparison for a Floater North of the Wind Turbine Affected by Shade and a Floater Unaffected by Shade

be related to this range, as the period during which it experiences shading remains constant. This trend, although not always proportional due to daily variations in irradiance, is generally observed.

Spikes indicating higher percentage losses than surrounding data points can be attributed to increased shading during periods of peak direct sunlight received on that day. Conversely, lower spikes can be explained by shading during cloudy times or low irradiance time for that day. This plot is useful for understanding expected energy losses throughout the year for floaters at various distances from the wind turbine.

4.5. Strategies for Cluster Placement Analysis

In this section, the focus will be on the strategies for cluster placement within the wind farm. The analysis will begin with an examination of the constraint map, highlighting various limitations and considerations for placement. Following this, different strategies for the best possible placement of the floating PV clusters will be discussed to maximise energy yield and minimise shading losses.

4.5.1. Constraint Map

In this subsection, the constraint map overlaid on top of the wind farm map and the energy grid map as seen in figure 4.25 is discussed. This map was obtained from actual data provided by [47]. The North Sea Energy Atlas is an online platform which provides comprehensive spatial information about various energy-related activities and constraints in the North Sea.

The spatial information was acquired in a GeoJSON format and subsequently imported and utilized in MATLAB. The dimensions for the smallest spatial pixel were 170m x 170m. Given that the mooring and anchoring lines of the floating installation will be placed on the seabed, it is not feasible to place any installations within the restricted areas. The constraint map considers three primary restrictions: shipping lanes, military areas, and electric cables.

It is noteworthy that the electric cables might appear to overlap with the strings of the wind farms. This overlap is a result of the hypothetical layout and coordinates of the wind farm, while the data derived

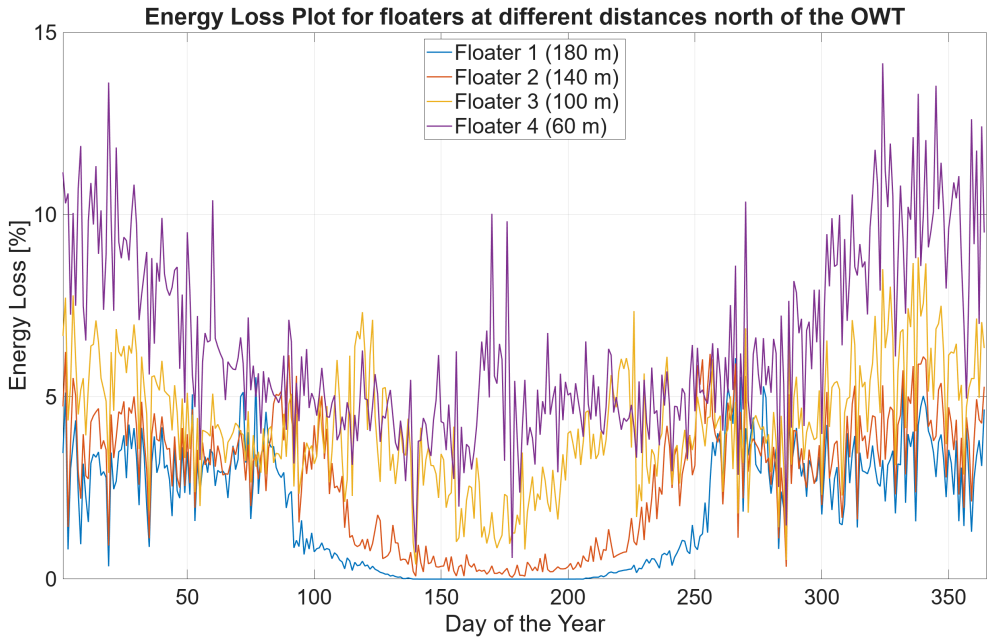

Figure 4.24: Daily Percentage Energy Loss for Floaters With Increasing Distances North of the Wind Turbine

from the North Sea Atlas is based on real-world data. This constraint map serves to illustrate how the energy grid maps can be used in a practical example, highlighting the importance of considering spatial restrictions in the placement of floating PV clusters.

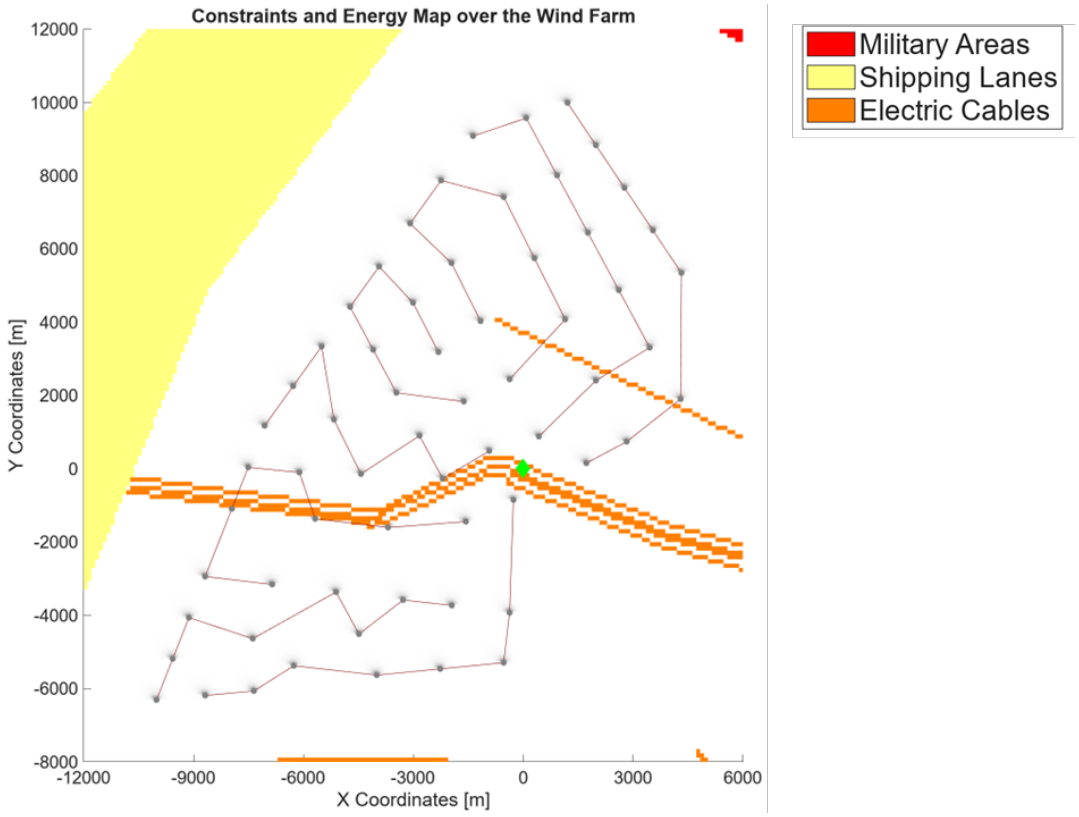

Figure 4.25: Constraint Map Overlaid on Wind Farm Map and Energy Grid Map

4.5.2. Cluster Placement Analysis

In this subsection, the analysis for placing the floating cluster around a wind turbine is discussed. A trivial solution would be to place the cluster south of the wind turbine, beyond the clearance area. However, this is not always feasible due to constraints such as wind turbine string cables or other restrictions. As illustrated in the figure, one such wind turbine scenario is analysed to understand how the energy map can be utilized for maximising energy extraction from the cluster while considering constraints.

Due to the size of the clusters considered in the wind farm, the clusters are positioned near the wind turbine and do not span so far as to be situated between two wind turbines. This scenario could only occur if the cluster dimensions were in the range of a kilometre, but they are less than 400 meters on any side. Consequently, the shading analysis for the energy grid map of the wind farm considers the impact of only one wind turbine. Even if a cluster is affected by shading from another wind turbine, it would occur during sunrise or sunset when the solar elevation angle is very low. Given the distance between wind turbines, which is several kilometres, the irradiance values at these times are already very low. Thus, it is justified to assume in the model that shading is caused by only one wind turbine for the offshore wind farm.

In the observed case, it is not possible to place the cluster south of the wind turbine due to the presence of electric cables running through that area. Consequently, the cluster must be positioned outside the clearance area of the wind turbine. Based on the grid map, a good place for the placement of the floating cluster is identified as shown in the figure 4.26. In the worst-case scenario, placing the cluster northwest of the wind turbine would result in producing approximately 100 MWh less energy.

This grid map proves useful in determining the placement for maximising energy yield. However, energy production is not the sole parameter for consideration when attempting to quantify and find an optimal placement for the floater. The positioning of the MV/HV transformer has not been considered in this study. For this placement analysis, the cluster has been positioned as close to the clearance area as possible to minimise cable costs and AC power loss for the cables connected to the wind turbine. However, this aspect has not been quantified. The optimal point could potentially be slightly further from the clearance area if research quantifies the LCOE and finds that overall shading losses exceed the combined losses and cable costs. In such a case, it would be advantageous to place the cluster further from the clearance area. This optimal placement is dependent on the configuration of the cluster, which has not been explored in this thesis.

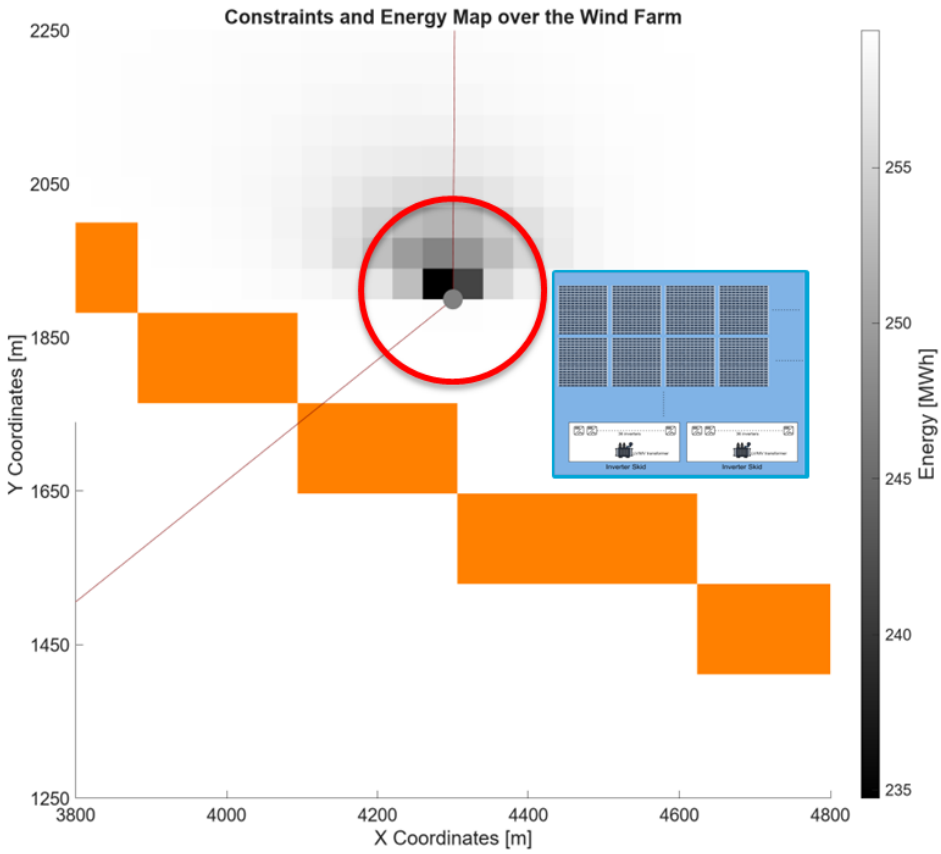

Figure 4.26: OFPV Placement Strategy Analysis for a Floating Cluster Around a Wind Turbine With Constraints in its Proximity

5

Discussion and Conclusion

In reflecting on the research objectives, the modelling sub-objective involved two critical aspects. Firstly, it was essential to consider the effect of sea waves on the tilt of OFPV systems. A model developed in [43] was employed, which, although stochastic and unable to predict power in real time, effectively quantifies the power variability caused by tilt. This model provides insights into how waves affect energy output over longer timescales. While adequate for this thesis, real-time modelling on a smaller timescale would necessitate 3D modelling software to accurately capture wave-floater interactions.

Secondly, the shading model, which was built from scratch, uses an analytical approach by representing the floating platform with a node gridmesh and employing a simplified geometry for the wind turbine. This model aligns with previous work and offers more flexibility, particularly in modelling dynamic shading effects from the wind turbine blades. However, it remains a simplified approach as it does not model the bypass diodes in the PV modules. Further improvements and optimisations could enable more detailed and dynamic simulations, providing deeper insights.

The second sub-objective aimed to qualitatively understand where to place an OFPV cluster within a wind turbine array for the considered simulation scenario. To achieve this, a grid map showing the energy output surrounding a wind turbine was developed. From this analysis, it was concluded that the placement for these OFPV clusters would be to the south of the wind turbines beyond it's clearance zone for maximum energy output. However, this solution is not always feasible due to real-life constraints. Therefore, various constraints were considered to identify potential areas around the wind turbine where the OFPV cluster could be placed to maximise energy output while remaining within constraint-free zones.

5.1. Implication of Findings

The findings from the tilt model have significant implications for predicting and understanding the variability of power generation on a daily or smaller time scale with a fine time resolution. By incorporating the tilt effects caused by waves, the model provides insights into how the power output from floating PV systems can fluctuate due to the dynamic sea conditions. This variability is crucial for optimising energy production and managing grid integration of offshore PV systems.

On an annual time scale, the effect of tilt on the energy produced by the floating PV systems is found to be minimal. These findings match with the findings in [43] where it was found that the loss in annual energy was about 0.1%. The simulations showed that the tilt could cause both increases and decreases in the energy output, essentially balancing out over the course of a year. This indicates that while tilt-induced variability is an important consideration for short-term energy management, its impact on long-term energy yield is negligible. This finding simplifies the long-term energy modelling and planning for floating PV installations.

Shading losses were identified as a critical factor influencing the energy yield in the wind farm configuration studied. The simulation results indicated that shading losses are most prominent to the north-northwest (NNW) of the wind turbine. This pattern is not only a consequence of the wind turbine's placement but also significantly influenced by the input irradiance data. The prevailing solar angles and the alignment of the wind turbine create a shading effect that predominantly affects the NNW region, leading to higher energy losses in these areas. Understanding this spatial variation in shading losses is essential for optimising the layout and placement of PV floaters to minimise energy deficits.

The irradiance map in Figure 4.9 shows a pattern similar to those found in [64], though the method for determining the shadow cast by the blades differs. Specifically, their approach considers an elliptical area affected by the wind turbine blades' shade. Additionally, the trend for energy loss observed in our study aligns with that seen in [68], and the figures illustrating the cumulative shading effect resemble the pattern seen in the figures showing the frequency of the nodes which are shaded on an annual time frame presented in Section 4.3. However, due to the lack of details on the wind turbine's location, dimensions, and PV array specifications in the referenced study, a direct comparison of the percentage of energy loss is not possible. Furthermore, in our study, the percentage loss for a floater is highly dependent on its physical configuration, making direct comparisons challenging.

5.2. Challenges and Limitations of this Work

While the tilt model developed in this study offers valuable insights, it is specifically tailored to the selected type of floater platform and relies on several simplifying assumptions. These assumptions were necessary to make the model feasible within the scope of this work and to understand how the tilting of the floater affects power and energy output. However, it is crucial to note that this model is statistical in nature, aiming to provide an overall effect of tilt rather than a real-time representation. Achieving real-time accuracy would require the use of advanced 3D simulation software incorporating fluid dynamics, which is beyond the scope of this study. Additionally, the current tilt model may not be applicable to different types of floating solar configurations, as the dynamics of each setup can vary significantly.

The shading model also presents certain limitations. One significant aspect not modelled is the impact of bypass diodes and shading on individual solar cell strings within a module. The presence of bypass diodes and non-uniform shading can considerably reduce the energy output, depending on the shape and extent of the shadow on the module. The current assumption that a shaded module is uniformly shaded simplifies the modelling process and does not capture the detailed effects of partial shading. This could lead to an underestimation of shading losses and, consequently, an overestimation of the energy output.

Moreover, the model does not account for potential dynamic shading effects caused by the moving blades of the wind turbine, which can further impact the energy yield. These simplifications, while necessary for this study's scope as mentioned in section 3.4.2, highlight areas where future work could focus on enhancing the model's accuracy and applicability to various floating solar PV configurations.

5.3. Practical Applications and Novelty

The methodologies and findings of this study lay the groundwork for developing a comprehensive framework for optimising the placement of floating PV systems integrated within offshore wind farms. This novel approach can significantly contribute to the efficient design and operation of hybrid energy farms by maximising energy yield while minimising losses due to shading and other environmental factors.

The shading model presented in this thesis introduces a novel analytical approach where the geometry of the wind turbine is approximated to simple shapes. In previous approaches [40, 64], the effects of the wind turbine blades have been approximated, focusing primarily on quantifying irradiance loss or introducing new terms such as land-loss. However, these methods do not consider the impact of shading on the power output of PV panels located near wind turbines. An exception is the work by [68], which investigates this effect taking into account the shape of the wind turbine, the yawing of the wind

turbine and, the power loss in PV arrays using a 3D shading simulation tool that leverages a graphical processing unit (GPU). Unlike these approaches, the model developed in the course of this project aims to provide a more straightforward yet effective means of analysing shading impacts without the need for complex simulations or oversimplification.

The innovative shading model developed in this research, which calculates the energy output of reference floaters surrounding a wind turbine, is instrumental in identifying floaters most susceptible to dynamic shading. This identification is crucial for considering inverter configurations and ensuring better performance of the hybrid system. Understanding which floaters experience the most dynamic shading allows for strategic placement and better inverter selection, ultimately improving the overall energy efficiency and reliability of the wind farm.

Furthermore, this work enhances the prediction accuracy of energy production and provides deeper insights into power variability for hybrid offshore wind-solar energy farms. By incorporating detailed models and simulations, stakeholders can make informed decisions regarding the layout and operational strategies of these renewable energy systems. The improved understanding of shading impacts and energy variability can lead to more robust and adaptive designs, ensuring that such hybrid systems can meet energy demands more effectively and sustainably.

5.4. Summary of Key Findings

The key findings from this research indicate that the tilting of the floater, on average, does not significantly affect the annual energy output. The variations in energy due to tilt tend to smooth out over a long duration, particularly for the floating PV configuration considered in this study. This suggests that, while tilt-induced intermittency is notable on shorter time scales, its impact on long-term energy yield is minimal.

In contrast, shading due to the wind turbine has a more pronounced effect on the annual energy output of the floating PV system. In the worst-case scenario, a floater situated near the wind turbine can experience up to a 10% reduction in annual energy output due to shading. For floaters positioned in an offshore installation beyond the clearance area of a wind turbine, the annual energy loss is approximately 3%. These findings underscore the importance of strategic placement to mitigate shading losses and optimise energy production in hybrid offshore wind-solar farms.

5.5. Significance of This Research

This research significantly advances the understanding of the impact of wind turbine shading on the energy output of photovoltaic (PV) systems. By developing and applying a more detailed shading model, this study helps better understand how wind turbines can influence the performance of PV modules in hybrid offshore wind-solar energy farms and the model can be transferred to land based hybrid wind-solar energy farms as well. The model helps predict power variability and annual energy output more accurately, which is crucial for optimising the design and placement of floating PV installations.

One of the aspects of this research is the integration of a tilt model to assess the impact of sea conditions on the performance of floating PV systems. This inclusion provides valuable insights into how tilt-induced intermittency affects daily and annual energy yield, contributing to a more nuanced understanding of floating PV performance in real-world conditions.

The shading model developed in this research is novel and has been meticulously crafted from scratch, providing a unique approach to understanding the shading effects of wind turbines on floating PV systems. Unlike previous studies that often approximated the effect of turbine blades by considering them as simple discs, this model takes into account the precise geometry of the blades. By accurately modelling the shape and movement of the blades, the shading effects are more realistically represented, offering a detailed and nuanced analysis. This advanced modelling approach enables a better prediction of shading impacts, leading to more reliable energy output assessments for hybrid wind-solar

installations.

Furthermore, the detailed irradiance and energy grid maps allows for a precise identification of areas most susceptible to shading. This can inform better placement strategies for floating PV clusters, enhancing the efficiency and reliability of hybrid renewable energy systems. These insights are not only applicable to offshore installations but also hold potential benefits for land-based hybrid wind-solar energy farms. Overall, this research lays the groundwork for future studies aimed at optimising the integration of PV systems with wind farms, ultimately contributing to more sustainable and efficient energy solutions.

5.6. Future Research Directions

The current study opens up several avenues for future research to enhance the accuracy and applicability of the models used. One significant direction is the incorporation of non-ideal Maximum Power Point Tracking (MPPT) modelling. By simulating different MPPT algorithms, it is possible to quantify the additional inverter losses caused by the dynamic shading of the wind turbine blades. These simulations should be validated against real-life experimental data to ensure accuracy and reliability. However, such detailed simulations would need to be conducted over very small time scales due to their computational intensity, making it impractical to extend them over an entire year.

To improve the shading model, the implementation of more efficient data structures could significantly reduce the runtime, thereby allowing for an increase in node resolution. This would enable more detailed and accurate modelling of the strings of solar cells within each module, incorporating the effects of bypass diode action under various shading conditions. Such enhancements would provide a more precise representation of the energy output and shading losses in the floating solar PV system.

Another future direction for this research involves leveraging the developed model to build a comprehensive framework for determining the optimal sizing of floating PV clusters integrated with wind farms. By conducting an in-depth analysis of the curtailment in inter-array cables connected to the offshore substation, the model can provide insights into the best possible configuration and size of the floating installation. This analysis would involve evaluating how different sizes and placements of the floating PV clusters affect the curtailment rates and overall efficiency of the hybrid renewable energy system. Furthermore, the model can be utilized to perform a detailed assessment of how varying the size of the floating cluster impacts the Levelized Cost of Energy (LCOE) of the entire system. By integrating economic factors with technical performance metrics, this approach aims to identify a balance between maximising energy output and minimising costs. The findings from such an analysis can guide the design and deployment of floating PV systems, ensuring that they contribute effectively to the overall energy mix while maintaining economic viability. Ultimately, this framework can serve as a decision-making tool for stakeholders, providing data-driven recommendations on the optimal sizing and placement of floating PV clusters within offshore wind farms. This would not only enhance the performance and reliability of hybrid renewable energy systems but also support the broader goal of sustainable and cost-effective energy production.

Future studies could also explore the integration of advanced fluid dynamics simulations to better understand the real-time interactions between the floater and sea waves. This would address one of the current model's limitations, providing a more realistic depiction of the tilt and its impact on energy production. Additionally, further research could investigate the optimal placement of floaters in various configurations and environmental conditions, considering not only energy yield but also factors like cable costs, AC power losses, and overall system efficiency.

References

[1] Ram Avtar et al. “Population–urbanization–energy nexus: a review”. In: *Resources* 8.3 (2019), p. 136.

[2] Ali Q Al-Shetwi. “Sustainable development of renewable energy integrated power sector: Trends, environmental impacts, and recent challenges”. In: *Science of The Total Environment* 822 (2022), p. 153645.

[3] Government of the Netherlands. *Climate Policy*. https://www.government.nl/topics/climate-change/climate-policy.

[4] ExxonMobil. *Energy Demand*. https://corporate.exxonmobil.com/what-we-do/energy-supply/global-outlook/energy-demand.

[5] North Sea Wind Power Hub. *Vision*. https://northseawindpowerhub.eu/vision.

[6] Evgeny Solomin et al. “8 Hybrid Floating Solar Plant Designs: A Review”. en. In: *Energies* 14.10 (May 2021), p. 2751. ISSN: 1996-1073. DOI: 10.3390/en14102751. URL: https://www.mdpi.com/1996-1073/14/10/2751 (visited on 09/18/2023).

[7] James F. Manwell. “Offshore Wind Energyoffshorewind energyTechnology Trends, Challenges, and Risks”. In: *Encyclopedia of Sustainability Science and Technology*. Ed. by Robert A. Meyers. New York, NY: Springer New York, 2012, pp. 7393–7425. ISBN: 978-1-4419-0851-3. DOI: 10.1007/978-1-4419-0851-3_697. URL: https://doi.org/10.1007/978-1-4419-0851-3_697.

[8] X. Costoya et al. “17. Combining offshore wind and solar photovoltaic energy to stabilize energy supply under climate change scenarios: A case study on the western Iberian Peninsula”. en. In: *Renewable and Sustainable Energy Reviews* 157 (Apr. 2022), p. 112037. ISSN: 13640321. DOI: 10.1016/j.rser.2021.112037. URL: https://linkinghub.elsevier.com/retrieve/pii/S1364032121012995 (visited on 09/18/2023).

[9] O. Lindberg, D. Lingfors, and J. Arnqvist. “14. Analyzing the mechanisms behind temporal correlation between power sources using frequency separated time scales: A Swedish case study on PV and wind”. en. In: *Energy* 259 (Nov. 2022), p. 124817. ISSN: 03605442. DOI: 10.1016/j.energy.2022.124817. URL: https://linkinghub.elsevier.com/retrieve/pii/S0360544222017200 (visited on 09/18/2023).

[10] Sundar Venkataraman et al. “Integrated wind, solar, and energy storage: Designing plants with a better generation profile and lower overall cost”. In: *IEEE Power and Energy Magazine* 16.3 (2018), pp. 74–83.

[11] S.Z.M. Golroodbari et al. “Pooling the cable: A techno-economic feasibility study of integrating offshore floating photovoltaic solar technology within an offshore wind park”. en. In: *Solar Energy* 219 (May 2021), pp. 65–74. ISSN: 0038092X. DOI: 10.1016/j.solener.2020.12.062. URL: https://linkinghub.elsevier.com/retrieve/pii/S0038092X20313219 (visited on 09/18/2023).

[12] Mervyn Smyth, James Russell, and Tony Milanowski. *Solar energy in the winemaking industry*. Springer Science & Business Media, 2011.

[13] Giuseppe Marco Tina et al. “Analysis of water environment on the performances of floating photovoltaic plants”. In: *Renewable Energy* 175 (2021), pp. 281–295.

[14] Thi Thu Em Vo et al. “Overview of Possibilities of Solar Floating Photovoltaic Systems in the OffShore Industry”. en. In: *Energies* 14.21 (Oct. 2021), p. 6988. ISSN: 1996-1073. DOI: 10.3390/en14216988. URL: https://www.mdpi.com/1996-1073/14/21/6988 (visited on 09/11/2023).

[15] Jun Wang and Peter D. Lund. “22. Review of Recent Offshore Photovoltaics Development”. en. In: *Energies* 15.20 (Oct. 2022), p. 7462. ISSN: 1996-1073. DOI: 10.3390/en15207462. URL: https://www.mdpi.com/1996-1073/15/20/7462 (visited on 09/18/2023).

[16] Parisa Ranjbaran et al. “A review on floating photovoltaic (FPV) power generation units”. In: *Renewable & Sustainable Energy Reviews* 110 (Aug. 2019). MAG ID: 2944698399, pp. 332–347. DOI: 10.1016/j.rser.2019.05.015.

[17] Kim Trapani et al. “Water absorption characterisation, electrical reliability and mechanical testing of a submerged laminated a-Si thin film photovoltaic (PV) cells”. In: *Microelectronics Reliability* 54.11 (2014), pp. 2456–2462.

[18] Vinod Kumar, RL Shrivastava, and SP Untawale. “Solar energy: review of potential green & clean energy for coastal and offshore applications”. In: *Aquatic Procedia* 4 (2015), pp. 473–480.

[19] Vikrant Sharma and Shyam Singh Chandel. “Performance and degradation analysis for long term reliability of solar photovoltaic systems: A review”. In: *Renewable and sustainable energy reviews* 27 (2013), pp. 753–767.

[20] Young-Kwan Choi and Young-Geun Lee. “A study on development of rotary structure for tracking-type floating photovoltaic system”. In: *International journal of precision engineering and manufacturing* 15 (2014), pp. 2453–2460.

[21] Frank Olsen and Kim Dyre. “Vindeby off-shore wind farm-construction and operation”. In: *Wind Engineering* (1993), pp. 120–128.

[22] Belachew Desalegn et al. “Onshore versus offshore wind power trends and recent study practices in modeling of wind turbines’ life-cycle impact assessments”. In: *Cleaner Engineering and Technology* 17 (2023), p. 100691. ISSN: 2666-7908. DOI: https://doi.org/10.1016/j.clet.2023.100691. URL: https://www.sciencedirect.com/science/article/pii/S2666790823000964.

[23] Tolga Kara and Ahmet Duran Şahin. “Implications of Climate Change on Wind Energy Potential”. In: *Sustainability* 15.20 (2023). ISSN: 2071-1050. DOI: 10.3390/su152014822. URL: https://www.mdpi.com/2071-1050/15/20/14822.

[24] Zhiyu Jiang. “Installation of offshore wind turbines: A technical review”. In: *Renewable and Sustainable Energy Reviews* 139 (2021), p. 110576. ISSN: 1364-0321. DOI: https://doi.org/10.1016/j.rser.2020.110576. URL: https://www.sciencedirect.com/science/article/pii/S1364032120308601.

[25] John Glasson et al. “The local socio-economic impacts of offshore wind farms”. In: *Environmental Impact Assessment Review* 95 (2022), p. 106783.

[26] Roberto Danovaro et al. “Making eco-sustainable floating offshore wind farms: Siting, mitigations, and compensations”. In: *Renewable and Sustainable Energy Reviews* 197 (2024), p. 114386. ISSN: 1364-0321. DOI: https://doi.org/10.1016/j.rser.2024.114386. URL: https://www.sciencedirect.com/science/article/pii/S1364032124001096.

[27] Hugo Díaz and C Guedes Soares. “Review of the current status, technology and future trends of offshore wind farms”. In: *Ocean Engineering* 209 (2020), p. 107381.

[28] Antonio Colmenar-Santos et al. “Offshore wind energy: A review of the current status, challenges and future development in Spain”. In: *Renewable and Sustainable Energy Reviews* 64 (2016), pp. 1–18.

[29] Mario López, Noel Rodríguez, and Gregorio Iglesias. “Combined Floating Offshore Wind and Solar PV”. en. In: *Journal of Marine Science and Engineering* 8.8 (Aug. 2020). Number: 8 Publisher: Multidisciplinary Digital Publishing Institute, p. 576. ISSN: 2077-1312. DOI: 10.3390/jmse8080576. URL: https://www.mdpi.com/2077-1312/8/8/576 (visited on 09/04/2023).

[30] European Commission. *2050 Long-Term Strategy*. https://climate.ec.europa.eu/eu-action/climate-strategies-targets/2050-long-term-strategy_en.

[31] David Connolly, Henrik Lund, and Brian Vad Mathiesen. “Smart Energy Europe: The technical and economic impact of one potential 100% renewable energy scenario for the European Union”. In: *Renewable and Sustainable Energy Reviews* 60 (2016), pp. 1634–1653.

[32] S. Zahra Golroodbari and Wilfried Van Sark. “30. Simulation of performance differences between offshore and land based photovoltaic systems”. en. In: *Progress in Photovoltaics: Research and Applications* 28.9 (Sept. 2020), pp. 873–886. ISSN: 1062-7995, 1099-159X. DOI: 10.1002/pip.3276. URL: https://onlinelibrary.wiley.com/doi/10.1002/pip.3276 (visited on 10/02/2023).

[33] Manish Kumar, Humaid Mohammed Niyaz, and Rajesh Gupta. “Challenges and opportunities towards the development of floating photovoltaic systems”. In: *Solar Energy Materials and Solar Cells* 233 (2021), p. 111408.

[34] Gaetano Mannino et al. “24. Photovoltaic Module Degradation Forecast Models for Onshore and Offshore Floating Systems”. en. In: *Energies* 16.5 (Feb. 2023), p. 2117. ISSN: 1996-1073. DOI: 10.3390/en16052117. URL: https://www.mdpi.com/1996-1073/16/5/2117 (visited on 09/18/2023).

[35] Adithi Prasannalal Sheena. *Feasibility Investigation of Floating PV in Hydro reservoirs: A case study on tropical and mediterranean climatic regions*. 2021.

[36] Siavash Asiaban et al. “Wind and solar intermittency and the associated integration challenges: A comprehensive review including the status in the Belgian power system”. In: *Energies* 14.9 (2021), p. 2630.

[37] Mohit Bajaj and Amit Kumar Singh. “Grid integrated renewable DG systems: A review of power quality challenges and state-of-the-art mitigation techniques”. In: *International Journal of Energy Research* 44.1 (2020), pp. 26–69.

[38] Nagananthini Ravichandran, Nagavinothini Ravichandran, and Balamurugan Panneerselvam. “Comparative assessment of offshore floating photovoltaic systems using thin film modules for Maldives islands”. In: *Sustainable Energy Technologies and Assessments* 53 (2022), p. 102490.

[39] Shiva Gorjian et al. “Recent technical advancements, economics and environmental impacts of floating photovoltaic solar energy conversion systems”. In: *Journal of Cleaner Production* 278 (2021), p. 124285.

[40] I. Mamia and J. Appelbaum. “37. Shadow analysis of wind turbines for dual use of land for combined wind and solar photovoltaic power generation”. en. In: *Renewable and Sustainable Energy Reviews* 55 (Mar. 2016), pp. 713–718. ISSN: 13640321. DOI: 10.1016/j.rser.2015.11.009. URL: https://linkinghub.elsevier.com/retrieve/pii/S1364032115012617 (visited on 10/23/2023).

[41] Nallapaneni Manoj Kumar et al. “Advancing simulation tools specific to floating solar photovoltaic systems – Comparative analysis of field-measured and simulated energy performance”. In: *Sustainable Energy Technologies and Assessments* 52 (Aug. 2022), p. 102168. ISSN: 2213-1388. DOI: 10.1016/j.seta.2022.102168. URL: https://www.sciencedirect.com/science/article/pii/S221313882200220X (visited on 09/01/2023).

[42] Sofiane Kichou, Nikolaos Skandalos, and Petr Wolf. “5. Floating photovoltaics performance simulation approach”. en. In: *Heliyon* 8.12 (Dec. 2022), e11896. ISSN: 24058440. DOI: 10.1016/j.heliyon.2022.e11896. URL: https://linkinghub.elsevier.com/retrieve/pii/S240584402203184X (visited on 09/18/2023).

[43] A. Alcañiz et al. “Offshore floating PV–DC and AC yield analysis considering wave effects”. en. In: *Energy Conversion and Management* 300 (Jan. 2024), p. 117897. ISSN: 01968904. DOI: 10.1016/j.enconman.2023.117897. URL: https://linkinghub.elsevier.com/retrieve/pii/S0196890423012438 (visited on 11/23/2023).

[44] Alessandro Niccolai et al. “A review of floating PV systems with a techno-economic analysis”. In: *IEEE Journal of Photovoltaics* (2023).

[45] Aritra Ghosh. “31. A comprehensive review of water based PV: Flotavoltaics, under water, offshore & canal top”. en. In: *Ocean Engineering* 281 (Aug. 2023), p. 115044. ISSN: 00298018. DOI: 10.1016/j.oceaneng.2023.115044. URL: https://linkinghub.elsevier.com/retrieve/pii/S0029801823014282 (visited on 10/18/2023).

[46] Netherlands Enterprise Agency (RVO). *General Information on Offshore Wind Energy*. https://offshorewind.rvo.nl/page/view/367fe51f-cc7d-4bd1-81f0-4aad448078d8/general-information. Accessed: June 29, 2024. 2024.

[47] North Sea Energy. *North Sea Energy Atlas*. https://north-sea-energy.eu/en/energy-atlas/.

[48] Canadian Solar. *BiHiKu7 CS7N-MB-AG Module Datasheet*. https://static.csisolar.com/wp-content/uploads/sites/3/2021/07/28105634/CS-BiHiKu7_CS7N-MB-AG_v1.7_F43M_J1_NA.pdf. Version 1.7, Accessed: June 29, 2024. 2021.

[49] FIMER. *Utility Applications Brochure*. https://www.fimer.com/sites/default/files/FIMER_Brochure-Utility.

[50] Junkun Zhang et al. "Design and optimization of a magnetron DC–DC isolated power supply with high efficiency". In: *IEEE Transactions on Power Electronics* 37.8 (2022), pp. 9392–9405.

[51] Jan Pierik et al. "A Wind Farm Electrical Systems Evaluation with EeFarm-II". en. In: *Energies* 3.4 (Mar. 2010), pp. 619–633. ISSN: 1996-1073. DOI: 10.3390/en3040619. URL: https://www.mdpi.com/1996-1073/3/4/619 (visited on 06/29/2024).

[52] Seyit A Akdağ and Ali Dinler. "A new method to estimate Weibull parameters for wind energy applications". In: *Energy conversion and management* 50.7 (2009), pp. 1761–1766.

[53] Royal Netherlands Meteorological Institute (KNMI). *Sunshine and Radiation Dataset - Sunshine and Radiation at a 10 Minute Interval*. https://dataplatform.knmi.nl/dataset/access/zonneschijnduur-en-straling-1-0. 2024.

[54] Royal Netherlands Meteorological Institute (KNMI). *Wind Data - Wind Data at a 10 Minute Interval*. https://dataplatform.knmi.nl/dataset/access/windgegevens-1-0. 2024.

[55] A. Oldroyd et al. *Wind Resource Assessment for Hollandse Kust (noord) Wind Farm Zone*. Report HKN$_2$0190312$_O BL_W RA - HKN_V 5_O F$. Oldbaum, Mar. 2019.

[56] Mark Mikofski. *Solar Position Calculator*. https://www.mathworks.com/matlabcentral/fileexchange/58405-solar-position-calculator. MATLAB Central File Exchange. Retrieved June 29, 2024. 2024.

[57] Mphethe I. Tongwane, Michael J. Savage, and Mitsuru Tsubo. "Relationship between global and diffuse irradiance and their variability in South Africa". en. In: *Theoretical and Applied Climatology* 137.1-2 (July 2019), pp. 1027–1040. ISSN: 0177-798X, 1434-4483. DOI: 10.1007/s00704-018-2646-7. URL: http://link.springer.com/10.1007/s00704-018-2646-7 (visited on 05/30/2024).

[58] Roland Séférian et al. "An interactive ocean surface albedo scheme (OSAv1. 0): formulation and evaluation in ARPEGE-Climat (V6. 1) and LMDZ (V5A)". In: *Geoscientific Model Development* 11.1 (2018), pp. 321–338.

[59] Klaus Hasselmann et al. "Measurements of wind-wave growth and swell decay during the Joint North Sea Wave Project (JONSWAP)." In: *Ergaenzungsheft zur Deutschen Hydrographischen Zeitschrift, Reihe A* (1973).

[60] Yang Yu, Hailong Pei, and Chengzhong Xu. "Parameter identification of JONSWAP spectrum acquired by airborne LIDAR". In: *Journal of Ocean University of China* 16 (2017), pp. 998–1002.

[61] MJ Tucker, Peter G Challenor, and DJT Carter. "Numerical simulation of a random sea: a common error and its effect upon wave group statistics". In: *Applied ocean research* 6.2 (1984), pp. 118–122.

[62] Sayyed Mohsen Vazirizade. "An intelligent integrated method for reliability estimation of offshore structures wave loading applied in time domain". PhD thesis. The University of Arizona, 2019.

[63] JS Mani. *Coastal hydrodynamics*. PHI Learning Pvt. Ltd., 2012.

[64] Sahil Shanghavi, W. Mack Grady, and Bradley Schwarz. "Evaluating the impact of wind turbine shadows on an integrated wind and solar farm". In: *2012 3rd IEEE PES Innovative Smart Grid Technologies Europe (ISGT Europe)*. 2012, pp. 1–6. DOI: 10.1109/ISGTEurope.2012.6465711.

[65] Elisa Skoplaki and John A Palyvos. "On the temperature dependence of photovoltaic module electrical performance: A review of efficiency/power correlations". In: *Solar energy* 83.5 (2009), pp. 614–624.

[66] WCL Kamuyu et al. *Prediction model of photovoltaic module temperature for power performance of floating PVs. Energies 11 (2): 447*. 2018.

[67] R. Chenni et al. “A detailed modeling method for photovoltaic cells”. en. In: *Energy* 32.9 (Sept. 2007), pp. 1724–1730. ISSN: 03605442. DOI: 10.1016/j.energy.2006.12.006. URL: https://linkinghub.elsevier.com/retrieve/pii/S0360544206003501 (visited on 05/02/2024).

[68] Jesus Robledo et al. *Dynamic simulation of the shading cast by a wind farm on an adjacent photovoltaic plant*. Sept. 2021.